Winter 12-15-2018

Effects of Secondary Stall and Unsteady Free-Stream on Blade Drag and Pitching Moments

Michael Malick
Washington University in St. Louis

Recommended Citation

Malick, Michael, "Effects of Secondary Stall and Unsteady Free-Stream on Blade Drag and Pitching Moments" (2018). *McKelvey School of Engineering Theses & Dissertations*. 386.
https://openscholarship.wustl.edu/eng_etds/386

WASHINGTON UNIVERSITY IN ST. LOUIS
School of Engineering and Applied Science
Department of Mechanical Engineering & Materials Science

Dissertation Examination Committee:
David Peters, Chair
Ramesh Agarwal
Roger Chamberlain
Swami Karunamoorthy
Patricia Weisensee

Effects of Secondary Stall and Unsteady Free-Stream on Blade Drag and Pitching Moments

by
Michael Malick

A dissertation presented to
The Graduate School
of Washington University in
partial fulfillment of the
requirements for the degree
of Doctor of Philosophy

August 2018
Saint Louis, Missouri

Table of Contents

List of Symbols

a	location of center of rotation aft of the mid-chord in semi-chords
b	blade semi-chord in meters
b_n	inflow expansion coefficients
C_l	lift coefficient
ΔC_l	static stall lift residual
C_d	drag coefficient
ΔC_d	static stall drag residual
C_m	moment coefficient
ΔC_m	static stall moment residual
e	forcing function derivative parameter of the stall equation
e_0	constant component of e stall parameter
e_2	quadratic component of e stall parameter
f	reversed-flow parameter
h	generalized airfoil motion, positive down, in meters
h_n	components of h as Chebychev polynomials
k	reduced frequency, $\omega b/u_0$
L	Lift per unit span in newtons per meter
L_n	generalized loads per unit span, in N/m
M	Number of shape function expansions in Johnson airloads theory
N	Number of inflow states
ΔP	Pressure difference across airfoil, in pascals
t	time, sec
u_0	freestream velocity, in m/s
x	location along the chordline, in meters
y	location perpendicular to the chordline, in meters
α	airfoil angle of attack, radians
α_s	constant correction to angle of attack, radians

γ	circulation per unit length, m/s
γ_b	bound circulation, m/s
γ_n	components of velocity due to bound circulation, m/s
γ_w	wake circulation, m/s
Γ	total bound circulation, m^2/s
Γ_n	pseudo-circulation due to the nth stalled load, m^2/s
η	damping parameter of the stall equation
η_0	constant component of η
η_2	quadratic component of η
λ	induced velocity due to shed wake, m/s
λ_n	induced velocity states, m/s
ρ	air density, kg/m^3
τ	non-dimensional time u_0t/b
τ_n	expansion coefficients for $\Delta P/(2\rho), m^2/s^2$
ϕ	Glauert variable, rad/s
ω	frequency parameter of the stall equation
ω_0	constant component of ω
ω_2	quadratic component of ω

List of Figures

List of Tables

Acknowledgements

This work was sponsored by the Army Research Office, ARO Grant # W911NF-13-1-0244, through a subcontract from Georgia Institute of Technology, Technical Monitor Dr. Matthew Munson.

Michael Malick

Washington University in St. Louis
August 2018

ABSTRACT OF THE DISSERTATION

Effects of Secondary Stall and Unsteady Free-Stream on Blade Drag and Pitching Moments

by

Michael Malick

Doctor of Philosophy in Aerospace Engineering

Washington University in St. Louis, 2018

Professor David Peters, Chair

Dynamic stall is a complex aerodynamic phenomenon occurring in helicopter rotors, limiting the flight envelope and causing control linkage damage and instabilities. The Peters-Modarres semi-empirical dynamic stall model is extended to simulate pitching moment and drag in unsteady freestream and yawed flow, including the effects of secondary stall. The aerodynamics are implemented as a state-space model, suitable for time-marching or aeroelastic analyses. With small modifications to the original stall model, secondary stall effects and unsteady freestream can be simulated without adding additional states. An optimization routine determines sets of parameters that minimize the error between the modeled solution and experimental data. The stall model is validated against five wind tunnel tests with a range of aerodynamic conditions. The results show good qualitative correlation with each test case, improving on the pitching moment and drag results of previously found by Ahaus.

Chapter 1: Introduction

Dynamic Stall describes the behavior of airloads for airfoils that perform dynamic motions into the regime in which static stall would normally occur. Dynamic stall is dominated by the time-dependent aerodynamic effect of the large vortices that are shed from an airfoil undergoing pitching oscillations [1]. In particular, when airfoil oscillations subject the airfoil to angles of attack beyond its linear regime, (i.e., beyond where it would generate lift linearly with angle of attack in steady flow), the airfoil experiences loads different from those experienced in static stall in a steady freestream. Dynamic stall becomes significant when the time an airfoil spends beyond the normal angles of attack is a significant fraction of the time required for the stall vortex to shed and traverse along the airfoil. The phenomenon is characterized by an increased lift beyond the maximum lift of the airfoil in steady flow, followed by a loss of lift due to the stall vortex and a delayed reattachment of the flow. A typical dynamic stall event can be seen in the lift data from Fig. 1.1, with the arrows indicating the direction of increasing time. While static and dynamic stall are usually described by their effects on lift, pitching moment and drag experience similar behavior: a hysteresis and overshoot of the static stall curves. Airfoil pitching moments during dynamic stall usually exhibit multiple "loops" in the data, indicating regions of negative aerodynamic damping. These can contribute to a phenomenon known as stall flutter.

Dynamic stall is an important condition for helicopter rotors in particular; it can occur at high advance ratios or heavily loaded rotors. At higher speeds, the helicopter rotor experiences a higher relative angle of attack on the retreating blade due to the relative wind, resulting in the stalled condition. Since the blades' positions are periodic, they do not stall statically, but oscillate in and out of stall. Dynamic stall in a helicopter is associated with excessive vibration and loads, a loss of lift, and severe control system feedback. It effectively establishes a limiting speed for helicopters in forward flight. Given the modern requirements for the U.S. military’s Joint Multi-Role helicopter, with intended designs capable of speeds exceeding 230 kts [2], dynamic stall remains a significant challenge to aerodynamicists and helicopter companies.

Stall flutter is the effect that occurs when there is net negative damping in the pitching moment response during cycles of dynamic stall. As in classical flutter, stall flutter is a dynamic instability that increases in amplitude over time, causing excessive loads in the entire rotor system. Ref. [3] indicates that the stall flutter phenomenon is due to the phasing between the pitching moment and the loss of bound vorticity during the dynamic stall event, and is most prevalent during what would be considered "light dynamic stall." In Ref. [4], significant amounts of experimental data was examined to determine regimes of stall flutter, which can be seen in Fig. 1.2. Regions of negative damping (indicated by clockwise loops in the moment graph) were found for cases where the airfoil oscillated through stalled and unstalled angles. Negative damping was not present outside of those regions, even for very deep stall. Cases investigated in this work will include regions of negative damping, including some cases of net negative damping.

Modelling stall flutter is a necessary step in the effort to alleviate it, in both passive and active implementations. Ref. [5] introduces an experiment in individual blade control for affecting stall flutter in an active manner. This system uses servo motors on a single blade in a rotating configuration to attempt to limit blade motions during the stall flutter events. The application of feedback through the servo motors showed a significant reduction in the stall flutter frequencies in the pitching moment response. In Ref. [6] airfoil shapes are investigated for their effects on stall flutter. The Boeing VR-5, VR-6, and VR-7 airfoil designs were influenced by the necessity for acceptable flutter characteristics, among other typical factors such as hover performance.

The pitching moment loads during dynamic stall of a helicopter rotor can impose very large stresses on the control system linkages, reducing their effective lifespan through fatigue and causing excessive vibration and feedback through the control systems [1]. While this can appear to be an issue of pitch-link strength, the cyclic loads due to stall flutter increase very rapidly with advance ratio, so simple reinforcement of the links and other components barely improve the flight envelope. Prediction of the pitch-link loads due to stall flutter is a major motivation for a reduced order stall model that correctly predicts pitching moment. Reference [6] shows how during a flight test of a CH-47C helicopter, variation in speed from 75 to 111 knots resulted in a 5-fold increase in peak pitch link loads; the flight test data was correlated with an aerodynamic model that showed similar maximum loads but different phasing.

Reduced-order modelling of dynamic stall in order to predict and reduce its effects is an important area of modern helicopter research. Flight computers use control models in order to predict control responses in real time and must rely on simplified aerodynamic models. Due to the computational complexities of CFD, a typical flight computer cannot utilize a CFD model and expect to get loads and controls predictions fast enough, necessitating the use of reduced order models. Examples of such models include the ONERA method [7-8], the Leishman-Beddoes method [9], the UTRC method [10-11], MIT method [12-13], and the Peters-Modarres model [14-15], which has been selected for the current work (Modarres in Ref. [14] shows a fair comparison of these stall models). All of these models require some kind of parameter identification or empiricism; unsteady stalled behavior currently cannot be described in even a simplified form by any closed form solution, nor is there a simplified analytical equation for the stalled region that can be time-marched with the other aerodynamic models. Thus, a large requirement for the development of these models is an extensive database of experimental data.

Experimental data, such as those presented in Refs. [16-23], represent a wide range of operating conditions, all with certain advantages and drawbacks. Empirical stall models are usually hierarchical, such that additional complexity, when added to a model, does not affect previous solutions, but may require different datasets to validate. Most dynamic stall data takes the form of a harmonically pitching airfoil section in a steady freestream, with equipment to measure the unsteady loads on the section. This represents 2D data without unsteady freestream, yawed flow, or finite-wing effects, as would be present in an actual helicopter. Full flight test data are also used, but use of these data requires the assumption of a structural model, and would not be used to validate a stall model alone. It is preferable (and much easier) to use the simpler datasets.

1.2 - Statement of work

The purpose of this work is to extend the Peters-Modarres dynamic stall model to prediction of pitching moment and drag, including the effects of secondary stall, unsteady freestream, and yawed flow. Secondary stall effects are evaluated for each case that requires them, as many do not show the behavior; cases without secondary stall can still be used for validation of the primary stall model. The airloads, inflow, and dynamic stall models that are used in Ref. [14] serve as the basis for the current work. The model is validated by comparison with experimental data from wind tunnel tests of several airfoils and flow conditions listed in Table 1. An optimization routine selects parameter sets for the stall models that result in the closest agreement with the data, and appropriate modifications to the models are added if there is poor correlation with the data. Though it is not a necessity, the optimization routine is coded with efficiency in mind, taking advantage of parallel computing. The optimization routine determines sets of stall parameters to minimize cost functions that measure the error between the computed and experimental results, recording these parameter sets for future use. However, the parameters themselves are not the goal of this process. The goal is to develop an efficient means of determining parameters for the end user of the stall model. Future users implementing these aerodynamic models in a flight simulator should be able to process their experimental data or their CFD results and obtain stall parameters with minimal manual adjustment. Improvements to the previous implementations of the optimization process in Ahaus and Modarres [15] [14] will reduce the time required for the user to set up the routine. A novel method is presented in Section 3.2 that simplifies the number of states needed to run the model, reducing the optimization time by a factor of nine.

1.3 - Literature review

A review of finite-state aerodynamic stall models is important to establish the precedent for the current model. While other aerodynamic models used in this work (airloads theory and inflow model) are particularly important, they are not being validated. Only the stall model from the previous work will be extended, modified, and validated in this work.

Closed-form and exact solutions for aerodynamic problems are important in their own right; but given the task of creating a real time solution method for dynamic stall, a finite-state approach is particularly useful. State-space representations use a system of first-order ordinary differential equations to represent a physical model [24]; each dependent variable in the system is called a state. State-space representations allow coupled aerodynamic and structural models to be time-marched using algorithms such as Runge-Kutta and Dormand-Prince. Finite-state models can be found in many areas in helicopter aerodynamics [25][26]. The airloads [27] and induced flow [28] models used in this work are examples of hierarchical finite-state models, indicating that the most significant aerodynamic effects are represented with the lowest-order states. As more states are added, changes to the aerodynamic results become less significant, while computational requirements increase. Finite-state models that can require a small number of states to accurately represent their physics are desirable.

1.3.2 Dynamic Stall Models

Dynamic stall models investigated here only represent finite-state, reduced order dynamic stall models. CFD models, while they can be time-marched, are too computationally intensive and are only an important comparison for accuracy; real time CFD simulation is currently only possible with supercomputers. The reduced order models used in this work stem from the original ONERA empirical model.

The ONERA model is the predecessor to the stall models used in Ahaus [15], Modarres [14], and this work. Developed in Refs. [7] and [8], the original ONERA method uses two equations: one for the linear lift in the unstalled region, and another for the lift in the stalled region, represented by Equations 1.1-1.3.

$$\begin{gathered}
C_L = C_{L1} + C_{L2} \\
\overset{*}{C}_{L1} + \hat{\lambda} C_{L1} = \hat{\lambda}\hat{a}\theta + (\hat{\lambda}\hat{s} + \hat{\delta})\overset{*}{\theta} + \hat{s}\overset{**}{\theta} \\
\overset{**}{C}_{L2} + \hat{\eta}\overset{*}{C}_{L2} + \hat{\omega}^2 C_{L2} = -\hat{\omega}^2 \left[\Delta C_L + \hat{e}\,\frac{\partial \Delta C_L}{\partial \theta}\,\overset{*}{\theta} \right]
\end{gathered} \tag{1.1-1.3}$$

The stalled lift equation contains parameters to be determined empirically from small-amplitude wind tunnel tests. This is similar to our parameter identification procedure, but is distinctly different in that ours involves large amplitude tests where wing sections are oscillated in and out of stall during one cycle, whereas identification of parameters in the original ONERA method involved small oscillations about fixed angles of attack either in stall or out of stall. In that method, many more tests were necessary to characterize the behavior of an airfoil for a given Mach number and reduced frequency than are required in the current stall model. Fig 1.3 shows these small-amplitude tests from Ref [17], which is the VR-7 data we use in Chapter 4. The small amplitude tests were necessary to determine the components of the empirical parameters that depend on $(\square\square_{\square})^{2}$(this process is developed in section 2.3.1).

Another difference in the present method with respect to the ONERA approach is that Peters in [29] indicated that the linear lift equation (Eq. 1.2) of the ONERA model implies a first-order approximation to induced flow, and should be replaced with a more general airloads and induced flow theory. That is the approach taken here. In addition, Peters suggested that the stalled lift equation be written in terms of circulation rather than lift coefficient. That form is used throughout this work and referred to as the "primary stall model." The Ahaus-Peters and Modarres-Peters stall models take have this general form, with additional equations being added to account for the effects of unsteady freestream and yawed flow.

An important finite state stall model for comparison is the Leishman-Beddoes model of Ref. [9]. This is a semi-empirical model for calculating lift, pitching moment, and drag of an airfoil in dynamic stall, based on the indicial method. Indicial methods use the step response of a system to determine the system’s response to arbitrary forcing via application of a convolution integral. Leishman uses an exponential approximation to the indicial lift and moment responses of an airfoil in potential flow for circulatory and non-circulatory terms, with factors included to account for compressibility effects. To model stall in the static case, the linear lift is interpolated to the stalled value with an exponential function at the point of stall. To include unsteady effects, this entire lift function is applied with an exponential function in time, representing a time delay. The indicial method has several disadvantages, one of which is the inability to separate the induced flow model or wake model from the airloads. Use of the Wagner function implies a flat wake, which is not a reasonable approximation to the helical wake of a helicopter rotor. While this may be sufficient for the determination of the empirical stall model with 2D data, it will require correction to predict the loads in a 3D scenario. The Leishman approach cannot arbitrarily substitute inflow models to correct for the 3D effects, which is why an ONERA-like approach is desired in the present work. The mutual independence of the stall, airloads, and induced flow models allows one to change very few equations when investigating 2D or 3D effects.

The Peters-Ahaus dynamic stall model forms the basis of the current work [15]; and as modified by Modarres [14], it is our foundation. Ahaus used the current form of the primary stall equation to correlate lift, pitching moment, and drag data. Only one set of parameters was used for a given combination of airfoil geometry and Mach number, using the same set for each of the loads. The optimization process used was very similar to the one in this work, though Ahaus used cost functions that evaluated the error between modeled lift and experimental lift only; no adjustment to the parameters was made that attempted to minimize the error in pitching moment or drag, as is done in this thesis. The cost functions Ahaus used evaluated a weighted-average of the errors in several cases in order to fit one set of parameters for a range of reduced frequencies. The airfoil tests investigated include NACA 0012, SC-1095, and Boeing VR12 data. The VR12 data, from Ref. [16] is the same set we being examined here.

One of the objectives of Ahaus' work was the evaluation of the dynamic stall model for morphing airfoils. The Johnson-Peters airloads theory was used in Ahaus provides loads in the linear region for an arbitrarily morphed airfoil, and the stall model exhibited great flexibility in the range of behavior it can reproduce. The morphed Boeing VR-12 variable droop leading edge from Ref. [16] was investigated with interest in evaluating the stall model for a design with active stall mitigation effects. A comparison of Figs. 5.15 and 5.12 in Ahaus, for example, shows significantly reduced loads for the case of an airfoil with variable droop, as compared to its unmorphed configuration. The validation of the tests on morphing airfoils is not repeated in this work.

Modarres in [14] directly extended the work of Ahaus to validate the dynamic stall model on additional datasets, ones that included secondary stall effects, yawed flow, and unsteady freestream, but for lift only[1]. This work explores the same datasets for pitching moment and drag. He uses the same Unified model, but with changes to accommodate secondary stall and unsteady freestream. The single pitching moment case in section 5.5 of

---

[1] Modarres included a single pitching moment case, but the rest were lift.

Modarres [14] was the first attempt to find a parameter set of the Unified model that was optimized for pitching moment instead of lift.

Modarres and Peters revealed that secondary stall effects present in the lift data can be modeled with a simple second-order equation driven by a rectangular pulse. This secondary equation is then used alongside the same primary stall model as before. The secondary stall effects are due to additional vortex shedding after the initial stall vortex, and cannot be captured by the primary stall model alone. While this requires an additional set of parameters, the approach requires no additional states in a state-space implementation, as the secondary stall equation can be solved in closed form. The secondary stall equation is developed in section 2.3.2.

The unsteady freestream effects can be fully included in the Johnson-Peters airloads theory, but a modification to the stall model was required. The important effect observed in Ref. [22] was that the stalled lift and pitching moment behavior was dependent on the freestream conditions present at the time of stall only, and did not vary significantly during the vortex shedding. In Modarres [14], since the stall model is dependent on freestream, a correction to the original model is needed to effectively “freeze” the freestream and circulation values at the time of stall. Section 2.3.3 details this modification.

Many more works covering dynamic stall have been detailed by Modarres [14] and Ahaus [15] than are presented here. Since this work does not modify the theory used in those references in any way, more background knowledge unneeded. Modarres and Ahaus both cover the history of dynamic stall in more detail.

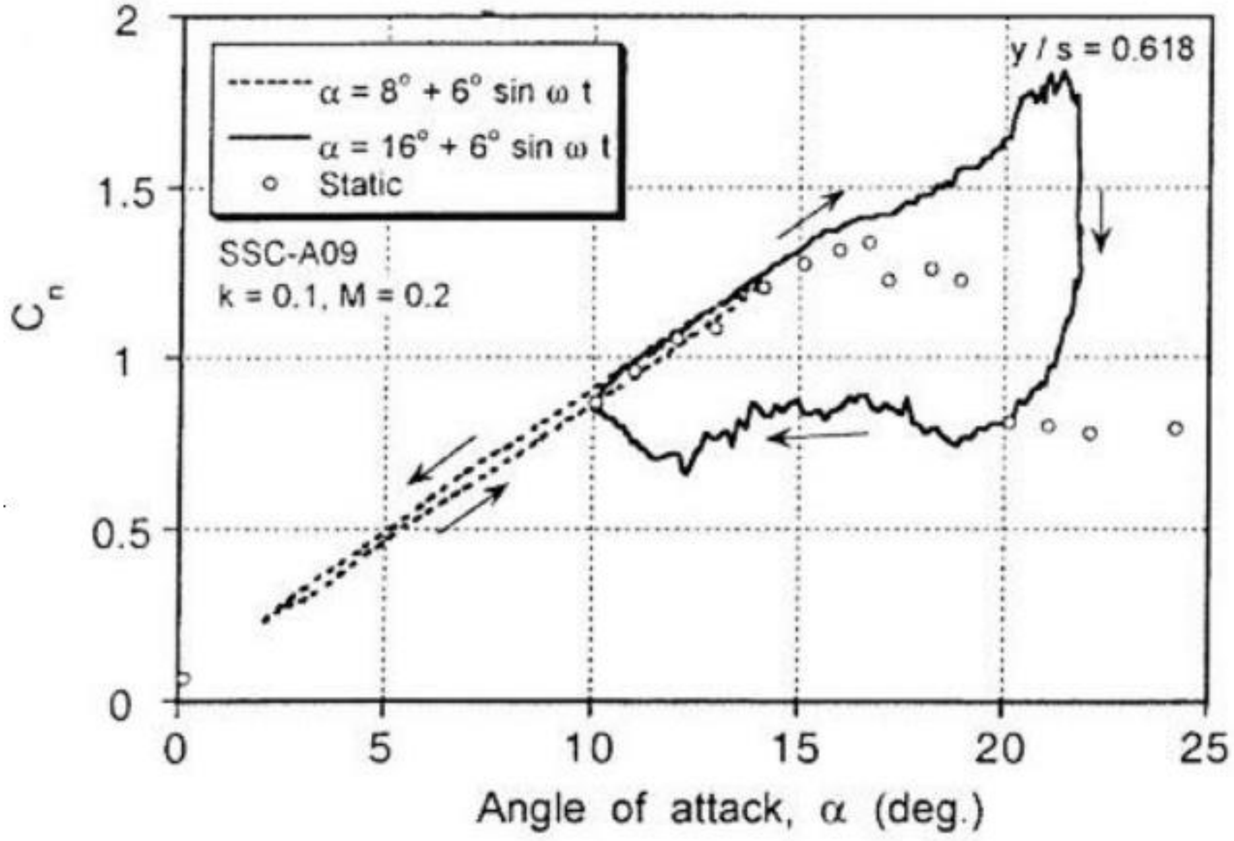

Figure 1.1 - a typical dynamic stall event in lift, compared to static data, from Ref. [14].

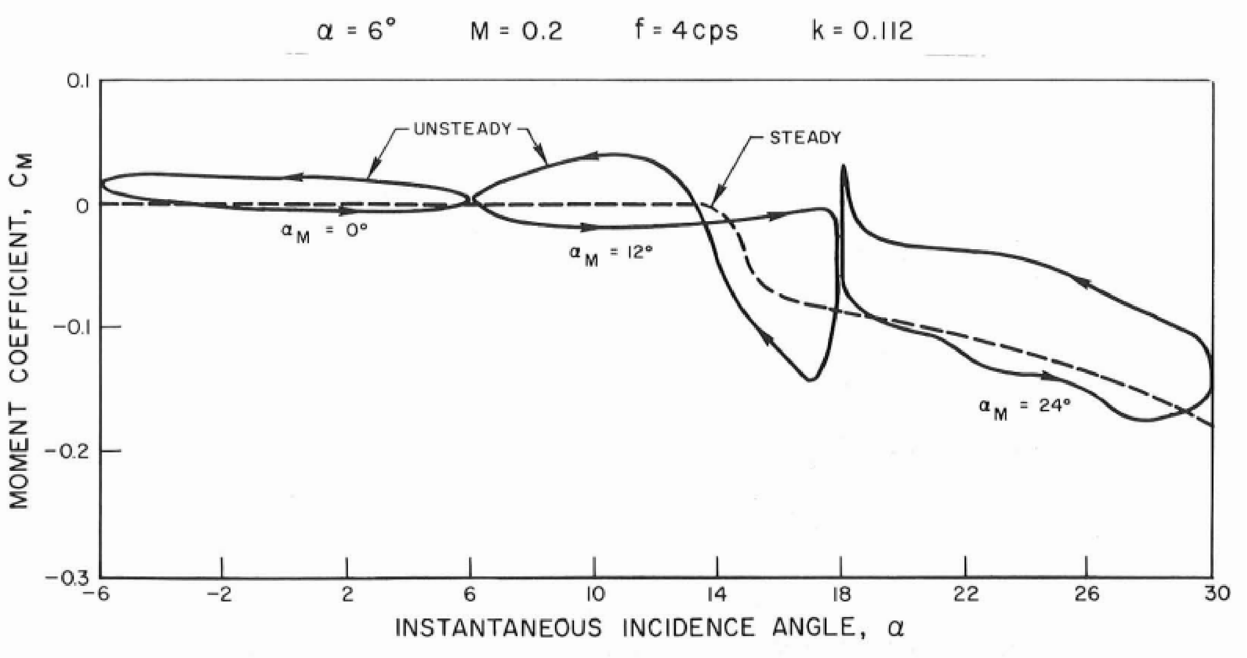

Figure 1.2 - Regimes of pitching moment stall from Ref. [4].

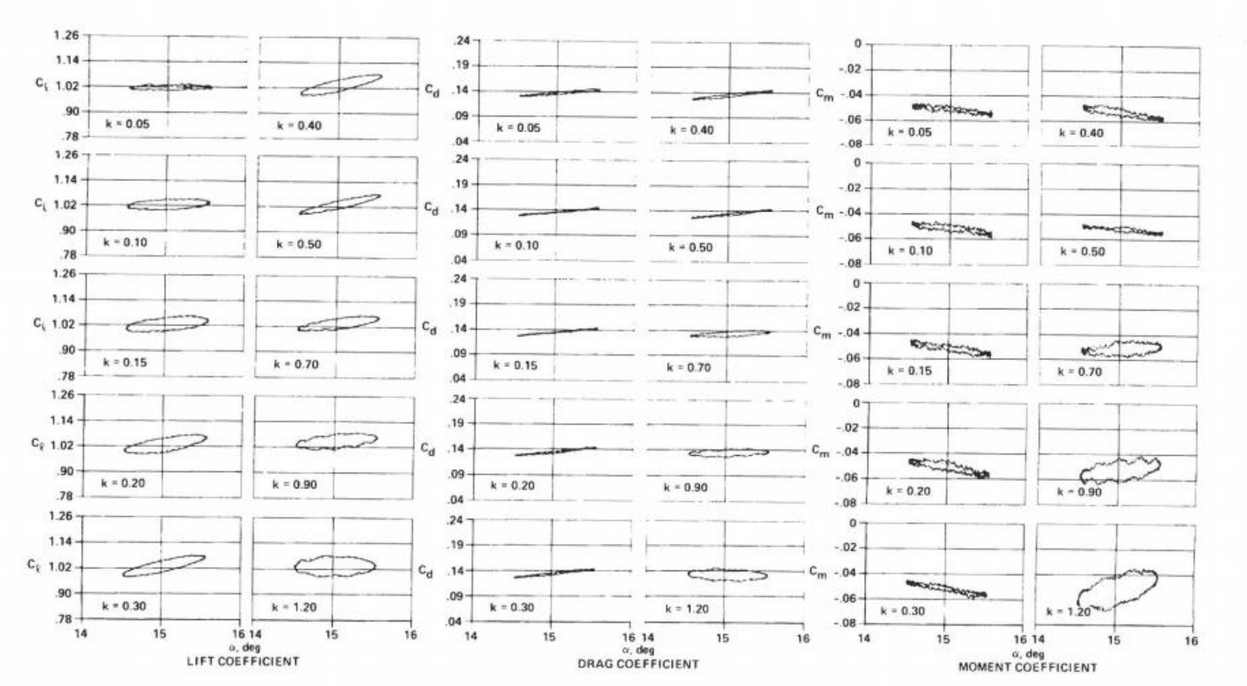

Figure 1.3 - Small amplitude tests from McCalister [17] that were required for validation of the old ONERA stall model. Amplitudes of only 2 degrees were typical.

Chapter 2 - Unified Model

The development of the set of aerodynamic models, referred to throughout this work as the Unified model, is crucial to the implementation of the dynamic stall model. The Unified model consists of the Johnson-Peters airloads model [27], the Peters-Karunamoorthy 2-D induced flow model [28], and the Peters-Modarres dynamic stall model [14]. Each of these models can act be replaced with equivalent models without changing the others (*i.e.,* the induced flow model can be changed from a 2D to a 3D model without affecting either the airloads or stall models). Figure 2.1 presents a flowchart that represents how the various models' inputs and outputs are related. The airloads theory is developed first in Section 2.1. This will provide the loads in the linear regime, the angles of attack smaller than the stall angle. In section 2.2, the 2D inflow model will calculate the free vorticity responsible for changing the angle of attack. Section 2.3 will define the primary stall model, secondary stall model, and unsteady freestream modifications. The Unified model consisting of the models in the previous 3 sections will be summarized in Section 2.4 and Appendix A. The result of this chapter is a state-space aerodynamic model that can predict lift, pitching moment, and drag on a 2D airfoil in steady or unsteady flow, stalled or unstalled. The Unified model is used in the optimization process of Chapter 3.

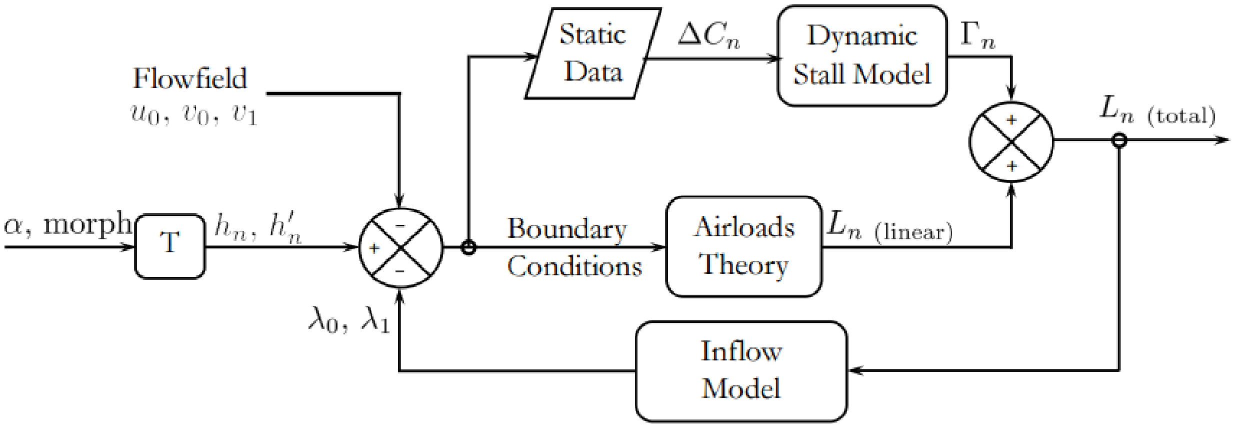

Figure 2.1 - Flowchart of the Unified Model

2.1 - Johnson-Peters airloads theory

Validation of the dynamic stall model requires an airloads theory that provides the pressure on an airfoil section or blade during a dynamic stall event; this implies that we need a theory that works under unsteady and large airfoil motions, without any small-angle assumptions. Following the procedure of previous work [14] and [15], our choice of airloads theory is the Johnson-Peters airloads theory defined in Ref. [27]. The model allows us to calculate lift, pitching moment, and drag through arbitrary blade motions and is not coupled to any inflow model, allowing it to work for 2D or 3D scenarios. The model also includes the effect of airfoil shape morphing, though we will likely only investigate rigid (unmorphed) airfoil sections in this work. The derivation of the Johnson-Peters theory provides a state-space representation, which will become necessary for the implementation of the Unified Model and its application in the optimization routine. The results of the following derivation is more compactly summarized in *Appendix A*, which is the form used in the code for this work.

Consider a given airfoil section, with its leading and trailing edges situated at coordinates -b and +b, where b is the half-chord. The airfoil is fixed with respect to the coordinate system, but that coordinate system is allowed to move with horizontal velocity u_0, vertical velocity v_0, and rotational velocity v_1. The airfoil is allowed to deform arbitrarily within its reference frame, only such that h<<b, dh/dx <<1, and dh/dt << u_0. The angles of the relative wind with respect to the reference frame are allowed to take on any value, with no small angle assumptions present. As is the case in thin-airfoil theory [30], the circulation generated by the airfoil is assumed to be concentrated along the chordline, which corresponds to the x-axis of the airfoil coordinate system.

The basis of the theory is the non-penetration boundary condition, eq 2.1 below:

$$w = \overline{v} + \lambda = u_0 \frac{\partial h}{\partial x} + \frac{\partial h}{\partial t} + v_0 + v_1 \frac{x}{b} \tag{2.1}$$

The total induced flow, w, is composed of λ , the induced flow from shed circulation, and $\bar{v}$, the induced flow from bound circulation. The movement of a point on the airfoil is with respect to the flow is represented by the v_0 and $v_1 x/b$ terms. The movement of a point on the airfoil due to the any changes in the shape of the section are represented by the $u_0 dx/dt\ +\ dh/dt$ term. As in thin-airfoil theory, there is no y-dependence. There are no restrictions on frame motion, so u_0, v_0, and $v_1$can be any value.

The induced flow from bound circulation can be found from the Biot-Savart law:

$$\bar{v} = \frac{-1}{2\pi} \int_{-b}^{b} \frac{\gamma_b(\xi,t)}{x-\xi} d\xi \tag{2.2}$$

where $\gamma_{\square}$is the unknown bound vorticity. The resulting pressure is determined by the pressure-vorticity equation:

$$\Delta P = \rho u_0 \gamma_b + \rho \int_{-b}^{x} \partial \gamma_b / \partial t \, d\xi \tag{2.3}$$

These 3 equations are all that is needed to compute airloads, but an additional model is required to compute λ. This inflow model can be chosen based on 2D or 3D flow conditions or more specific assumptions about the wake geometry. Any appropriate inflow model can be used since the derivation of the airloads theory is not dependent on any particular inflow assumptions. Regardless of the inflow model used, λ must satisfy the following equation:

$$\partial\lambda/\partial t + u_0 \partial\lambda/\partial x = \frac{d\Gamma/dt}{2\pi}\frac{1}{b-x} + \bar{u}_0 \partial\zeta/\partial x \tag{2.4}$$

where Γ is the total bound circulation, ζ is induced flow due to external bound vorticity, and $\bar{u}_0$ is the velocity of that external bound vorticity (for all the cases investigated in this work, external bound vorticity can be assumed negligible).

Equations 2.1 and 2.2 can be converted into ordinary differential equations through a Glauert expansion. We make a change of variable to express x in terms of the Glauert variable, ϕ:

$$x = b\cos\phi$$
$$-b \le x \le b, \quad 0 \le \phi \le \pi \tag{2.5}$$

For positive u_0, $\phi = 0$ is at the trailing edge, while $\phi = \pi$ is at the leading edge. With this change of variable, thin airfoil theory results in the following expansions:

$$\gamma_b = 2\left[\frac{+\gamma_s}{\sin\phi} - \frac{\gamma_0 \cos\phi}{\sin\phi} + \sum_{n=1}^{\infty}\gamma_n \sin(n\phi)\right]$$

$$\Delta P = 2\rho\left[\frac{+\tau_s}{\sin\phi} - \frac{\tau_0 \cos\phi}{\sin\phi} + \sum_{n=1}^{\infty}\tau_n \sin(n\phi)\right] \tag{2.6-2.7}$$

The shape functions and velocities are also expanded in the Glauert variable:

$$h = \sum_{n=0}^{\infty} h_n \cos(n\varphi)$$

$$w = \sum_{n=0}^{\infty} w_n \cos(n\varphi)$$

$$\lambda = \sum_{n=0}^{\infty} \lambda_n \cos(n\varphi)$$

$$\bar{v} = \sum_{n=0}^{\infty} \gamma_n \cos(n\phi)$$

(2.8-2.11)

If we substitute Eqs. 2.6-2.7 into 2.3, it simplifies to the following relation:

$$u_0 \gamma_s = \tau_s, \quad u_0 \gamma_0 = \tau_0$$

$$b(\dot{\gamma}_0 - \frac{1}{2}\dot{\gamma}_2) + u_0 \gamma_1 = \tau_1 - \dot{\Gamma}/\pi$$

$$\frac{b}{2n}(\dot{\gamma}_{n-1} - \dot{\gamma}_{n+1}) + u_0 \gamma_n = \tau_n - \dot{\Gamma}/(n\pi) \quad n \geq 2$$

(2.11)

We get another set of differential equations using the Glauert expansion for wake circulation, substituting 2.10 into 2.4:

$$b(\dot{\lambda}_0 - \frac{1}{2}\dot{\lambda}_2) + u_0 \lambda_1 = \dot{\Gamma}/\pi + \bar{u}_0 \zeta_1$$

$$\frac{b}{2n}(\dot{\lambda}_{n-1} - \dot{\lambda}_{n+1}) + u_0 \lambda_n = \dot{\Gamma}/(n\pi) + \bar{u}_0 \zeta_n \qquad n \geq 2$$

(2.12)

If we add Eqs. 2.11 and 2.12, we get the form of the equation used to calculate loads:

$$w \equiv \bar{v} + \lambda = \sum_{n=0}^{\infty} w_n \cos(n\phi)$$

$$\Rightarrow w_n = \gamma_n + \lambda_n$$

$$u_0(w_0 - \lambda_0) = \tau_0$$

$$b(\dot{w}_0 - \frac{1}{2}\dot{w}_2) + u_0 w_1 = \tau_1 + \bar{u}_0 \zeta_1$$

$$\frac{b}{2n}(\dot{w}_{n-1} - \dot{w}_{n+1}) + u_0 w_n = \tau_n + \bar{u}_0 \zeta_n \qquad n > 2$$

(2.13-2.14)

In order to be useful in application, 2.14 must be in terms of ▯$_n$, the shape of the airfoil camber line. This can be done using the ▯▯ expansions and the non-penetration boundary condition:

$$w_0 = v_0 + \dot{h}_0 + u_0 \sum_{n=1,3,5}^{\infty} nh_n/b$$

$$w_1 = v_1 + \dot{h}_1 + 2u_0 \sum_{n=2,4,6}^{\infty} nh_n/b$$

$$w_m = \dot{h}_m + 2u_0 \sum_{n=m+1,m+3,}^{\infty} nh_n/b \quad m \geq 2 \tag{2.15}$$

The last condition we need before loads is the Kutta condition, which makes$\tau_{▯} = ▯_0$. In real rotor conditions, this should be changed to accomodate reversed flow, as mentioned in Ref [27]. No test present in this work will contain reversed flow, so the Kutta condition is sufficient.

The generalized loads per unit span can be determined by integrating the pressure distribution over the airfoil:

$$L_n = -\int_{-b}^{+b} \Delta P \cos(n\phi) dx = -\int_0^{\pi} b \Delta P \cos(n\phi) \sin\phi d\phi \tag{2.16}$$

This, combined with 2.7, gives the generalized loads for all n. The matrix form of this equation, and the form used in the code, is shown in Eq. 2.17.

$$\frac{1}{2\pi\rho}\{L_n\} = -b^2[M]\left\{\ddot{h}_n + \dot{v}_n\right\} - bu_0[C]\left\{\dot{h}_n + v_n - \lambda_0\right\} - {u_0}^2[K]\{h_n\}$$
$$- b[G]\{\dot{u}_0 h_n - u_0 v_n + u_0 \lambda_0\} \tag{2.17}$$

The definitions of each matrix and vector term in Eq. 2.17 are found in Appendix A. $▯_0$, which is the negative lift per unit length, is Eq. 2.18:

$$L_0 = -2\pi b\rho(\tau_0 f + \frac{1}{2}\tau_1) =$$

$$[-2\pi\rho f u_0(w_0 - \lambda_0) - \pi\rho u_0 w_1 - \pi\rho b(\dot{w}_0 - \frac{1}{2}\dot{w}_2) + \pi\rho\bar{u}_0\zeta_1]b \tag{2.18}$$

L$_1$, which is the nose-up pitching moment per unit length per semi-chord, is Eq. 2.19:

$$L_1 = \pi b\rho(\tau_0 - \frac{1}{2}\tau_2) = [\pi\rho u_0(w_0 - \lambda_0) - \frac{1}{2}\pi\rho u_0 w_2 + \frac{1}{2}\pi\rho\bar{u}_0\zeta_2 \\ -\frac{1}{8}\pi\rho b(\dot{w}_1 - \dot{w}_3)]b \tag{2.19}$$

Pressure drag can be found by computing the integral expression in Eq. 2.20:

$$D = \int_{-b}^{+b}(\Delta P)(\partial h/\partial x)dx \; - 2\pi\rho b f(w_0 - \lambda_0)^2 \\ = \int_0^{\pi} b(\Delta P)(\partial h/\partial x)\sin\phi d\phi - 2\pi\rho b f(w_0 - \lambda_0)^2 \tag{2.20}$$

Using the same expansions for pressure and airfoil shape from earlier, the pressure drag is:

$$D = -2\pi\rho b(v_0 + \dot{h}_0 - \lambda_0)\Bigg[f(v_0 + \dot{h}_0 - \lambda_0) \\ + u_0 \sum_{n=1,3,5}^{\infty} fnh_n/b + u_0 \sum_{n=2,4,6}^{\infty} nh_n/b\Bigg] \\ + 2\pi\rho\sum_{n=1}^{\infty} h_n\left[\frac{b}{4}(\ddot{h}_{n-1} - \ddot{h}_{n+1}) + nu_0\dot{h}_n + \frac{1}{2}n\dot{u}_0 h_n - \frac{1}{2}n\bar{u}_0\zeta_n\right] \\ + 2\pi\rho h_1\left(\frac{b}{2}\dot{v}_0 + \frac{b}{4}\ddot{h}_0\right) + 2\pi\rho h_2\frac{b}{4}\dot{v}_1 + \pi\rho u_0 v_1 h_1 \tag{2.21}$$

Note this does not include profile drag, which must be added outside of the Johnson-Peters theory. Typically, profile drag is input as a correction directly from experimental data, and is small compared to the overall drag. The matrix form of the drag equation used in the code is Eq. 2.22:

$$\frac{1}{2\pi\rho}D = -b\left\{\dot{h}_n + v_n - \lambda_0\right\}^T [S]\left\{\dot{h}_n + v_n - \lambda_0\right\} + b\left\{\ddot{h}_n + \dot{v}_n\right\}^T [G]\{h_n\} \\ - u_0\left\{\dot{h}_n + v_n - \lambda_0\right\}^T [K - H]\{h_n\} + \{\dot{u}_0 h_n - u_0 v_n + u_0\lambda_0\}^T [H]\{h_n\}$$

(2.22)

The end result of this section is a set of equations used to calculated the linear airloads of airfoils with arbitrary morphing camber lines in unsteady flow. This applies to every pitching moment and drag dataset investigated in Chapter 4, but does not account for stalled loads, which will be handled in Section 2.3. While equations 2.18, 2.19, and 2.22 are used to calculate every load in the results chapter, λ_0, the constant component of inflow, is still undetermined.

2.2 - Peters-Karunamoorthy 2D Induced Flow Model

The Peters-Karunamoorthy 2D inflow model of Ref [28] is used to complete the set of loads equations in Section 2.1. All of the quantities are determined except for λ_0, so an inflow model must be used to close the system, and the Karunamoorthy model is used here because all of the test cases in this work are considered 2D flow conditions. 3D flow conditions would require a different inflow model, which can be accommodated by a 3D inflow model such as the Peters-He model if necessary [31]. The important quantity for the loads of interest in the previous section is λ_0, which represents the constant term of the induced flow distribution (like the other quantities, induced flow is represented as a combination of Chebyshev polynomials). Other inflow terms are necessary in order to determine λ_0, but only λ_0 is needed to determine lift, pitching moment, or drag.

Using the potential function expansion of wake velocity from [28], Eq. 2.4 results in 2.23:

$$
\begin{aligned}
b\left(\dot{\lambda}_0 - \frac{1}{2}\dot{\lambda}_2\right) + u_0\lambda_1 &= \frac{\dot{\Gamma}}{\pi} \\
\frac{b}{2n}(\dot{\lambda}_{n-1} - \dot{\lambda}_{n+1}) + u_0\lambda_n &= \frac{\dot{\Gamma}}{n\pi} \quad n \geq 2
\end{aligned}
\tag{2.23}
$$

2.23 is a system of N differential equations for determining N+1 inflow states that holds true for any wake model (as before, assuming the external vorticity term from Eq. 2.4 is 0). One more relation is necessary to close the system, and for a flat wake, λ_0 may be approximated by Equation 2.24:

$$
\lambda_0 \approx \frac{1}{2}\sum_{n=1}^{N} b_n\, \lambda_n
\tag{2.24}
$$

where b_n is defined by 2.25:

$$b_n = (-1)^{n-1} \frac{(N+n)!}{(N-n)!} \frac{1}{(n!)^2} \quad n = 1, 2, \cdots, N-1$$
$$b_N = (-1)^{(N+1)} \tag{2.25}$$

Equation 2.23 is now the 2D inflow model, but in order to be useful, the total circulation derivative term, $\dot{\mathit{\Gamma}}$,must be expressed in known quantities. From the airloads theory [27], the total circulation can be expressed as:

$$\Gamma = 2\pi b \left[f(w_0 - \lambda_0) + \frac{1}{2} w_1 - \frac{1}{2} \lambda_1 \right] \tag{2.26}$$

This must be added to the circulation due to stall, $\mathit{\Gamma}_0$, and differentiated to produce the right hand side of 2.23:

$$\dot{\Gamma} = 2\pi b \left[f(\dot{w}_0 - \frac{1}{2} \{b\}^T \{\dot{\lambda}\}) + \frac{(\dot{w}_1 - \dot{\lambda}_1)}{2} \right] + \dot{\Gamma}_0 \tag{2.27}$$

where the $\{b\}^T\{\dot{\lambda}\}$term is the matrix form of λ_0 (all vectors and matrices are defined in Appendix A). Equation 2.23 can now be written as:

$$\begin{aligned}
\left(\frac{1}{2} + f\right) \{b\}^T \{\dot{\lambda}\} + \dot{\lambda}_1 - \frac{1}{2}\dot{\lambda}_2 &= 2\left(f\dot{w}_0 + \frac{1}{2}\dot{w}_1\right) + \frac{1}{b\pi}\dot{\Gamma}_0 - \frac{u_0}{b}\lambda_1 \quad n = 1 \\
\frac{f}{2}\{b\}^T\{\dot{\lambda}\} + \frac{3}{4}\dot{\lambda}_1 - \frac{1}{4}\dot{\lambda}_3 &= \left(f\dot{w}_0 + \frac{1}{2}\dot{w}_1\right) + \frac{1}{2b\pi}\dot{\Gamma}_0 - \frac{u_0}{b}\lambda_2 \quad n = 2 \\
\frac{f}{n}\{b\}^T\{\dot{\lambda}\} + \frac{1}{n}\dot{\lambda}_1 + \frac{1}{2n}\dot{\lambda}_{n-1} - \frac{1}{2n}\dot{\lambda}_{n+1} &= \frac{2}{n}\left(f\dot{w}_0 + \frac{1}{2}\dot{w}_1\right) + \frac{1}{nb\pi}\dot{\Gamma}_0 - \frac{u_0}{b}\lambda_n \quad n \geq 3
\end{aligned} \tag{2.28}$$

This is now a complete system of equations for the wake velocities λ_n in terms of flow conditions (w) and stall conditions ($\dot{\mathit{\Gamma}}_0$). If we express this system in matrix form, using the definitions from the airloads theory, it becomes:

$$\{\dot{\lambda}\} = [A]^{-1} \left[\{c\} \left(\{e\}^T \{\dot{v}_n + \ddot{h}_n\} + \frac{u_0}{b} \{f\}^T \{\dot{h}_n\} + \frac{\dot{\Gamma}_0}{2b\pi} \right) - \frac{u_0}{b} \{\lambda\} \right] \tag{2.29}$$

This is the form of the inflow used in the Unified model (and the code). The $\lambda_{\square}$ are expressed as 8 states, so Eq. 2.29 represents 8 equations that must be time-marched in the state-space model. 2 additional states, $\mathit{\Gamma}_0$and $\dot{\mathit{\Gamma}}_0$, are needed to complete the states for the Unified model. These 8 inflow equations are the most computationally intensive part of simulation, but that burden can be greatly reduced during optimization with the developments in Section 3.2.2.

2.3 - Peters-Modarres Dynamic Stall Model

The dynamic stall model used throughout this work takes several forms, all of which were developed in the previous work by Modarres [14]. The intention of the stall model, as stated in Chapter 1, is to provide a quantitatively accurate simulation of pitching moment and drag during dynamic stall, including several effects previously explored by Modarres for lift, such as the secondary load peaks and effects of unsteady freestream. The model developed here will use lift data, but will only be applied to calculating pitching moment and drag.

2.3.1 - Primary stall model

The 6-parameter ONERA model, modified by Ahaus [15], is one of the models referred to throughout this work as the "primary stall model." Eq. 2.9 and 2.10 represent this primary stall model, and they take the same form in the previous works.

$$\frac{b^2}{U^2}\ddot{\Gamma}_n + \eta\frac{b}{U}\dot{\Gamma}_n + \omega^2\Gamma_n = -bU\omega^2\left[\Delta C_n + e\frac{b}{U}\frac{d\Delta C_n}{dt}\right] \tag{2.30}$$

$$L_n = L_{n(linear)} + \rho U \Gamma_n \tag{2.31}$$

The Γ_n terms represent the stall correction to the "n^th^" quantity, L_n. Every stalled load will have an associated Γ_n; for lift, this physically represents the circulation loss due to stall, but it does not have the same physical meaning for the other loads, so it is called *pseudo-circulation*. The $L_{n(linear)}$term represents the contribution to that load from the linear Peters-Johnson airloads theory. Each load will have a set of 6 stall parameters associated with it; these stall parameters are the coefficients in Eq. 2.30, and they have the following functional form:

$$\omega = \omega_0 + \omega_2(\Delta C_L)^2 \tag{2.32}$$

$$\eta = \eta_0 + \eta_2(\Delta C_L)^2 \tag{2.33}$$

$$e = e_0 + e_2(\Delta C_L)^2 \tag{2.34}$$

Each set of parameters represents a point in the space of the cost function used during the optimization routine. These are empirical parameters, determined only by the optimization, and do not have units.

The Γ_n of Equations 2.30-2.31 is Γ_0 of Equation 2.29. Eq. 2.30 above (the primary stall equation), when expressed in state-space form, provides the equations for the 2 stall states that complete the model when combined with the 8 inflow states. While the optimization process determines the parameters to the stall equation, the time-marching must occur for the 10 total states, as the equations are coupled. The stall equations contain inflow terms through the quantities dependent on angle of attack, $\Delta C_l, \Delta C_d, and\ \Delta C_m$, and the inflow equations contain the derivative of pseudo-circulation.

The primary stall model used throughout this work, referred to as the "12-parameter model", is a modification of the original 6-parameter model to allow multiple parameter sets for a single cycle of airfoil oscillation. It was observed early on that a single parameter set only captured the stall effects of pitching moment accurately on the upstroke of an oscillating airfoil; given that a large improvement for lift results in the previous work was possible by allowing separate stall parameters for the upstroke and downstroke, we have elected to use the 12-parameter model as the primary stall model throughout this work, unless otherwise stated.

It is important to note that while Modarres needed a cross-coupling term plus an additional 2 stall parameters to model pitching moment, our model does not. The same stall equation he used for lift is used here for pitching moment and drag.

2.3.2 - Secondary stall model

The secondary stall phenomenon was explored heavily by Modarres [14] for lift, who had also observed similar behavior in the other loads. He described secondary stall as one or more peaks in the lift following the first stall peak, as shown in Fig. 2.2. Modarres noted that the primary stall model was unable to match these additional peaks in the lift, and similar peaks were also present in several sets of pitching moment and drag data [16][17]. The difference in the stall model and the experimental data revealed a plot that could be matched by the response of a simple harmonic oscillator. He used a simple second-order equation for a harmonic oscillator driven by a rectangular pulse to represent this secondary stall phenomenon. This secondary stall model of Eq. 2.35 is used alongside the primary stall model, being activated only in the region of secondary load peaks:

$$\left(\frac{b}{U}\right)^2 \ddot{\Gamma}_{s,n} + 2\left(\frac{b}{U}\right)\zeta\omega_s\dot{\Gamma}_{\mathrm{s,n}} + \omega_s^2\Gamma_{s,n} = \omega_s^2 h_s(u(\tau_i) - u(\tau_e)) \tag{2.35}$$

As in the primary stall model, the $\Gamma_{s,n}$ is the contribution to that particular load from the secondary stall model. An additional set of 5 parameters for each load is needed, but no additional states are required to simulate secondary stall effects, since the equation has a closed-form solution. For the loads and inflow equations, the secondary stall pseudo-circulation is simply added to the primary stall pseudo-circulation.

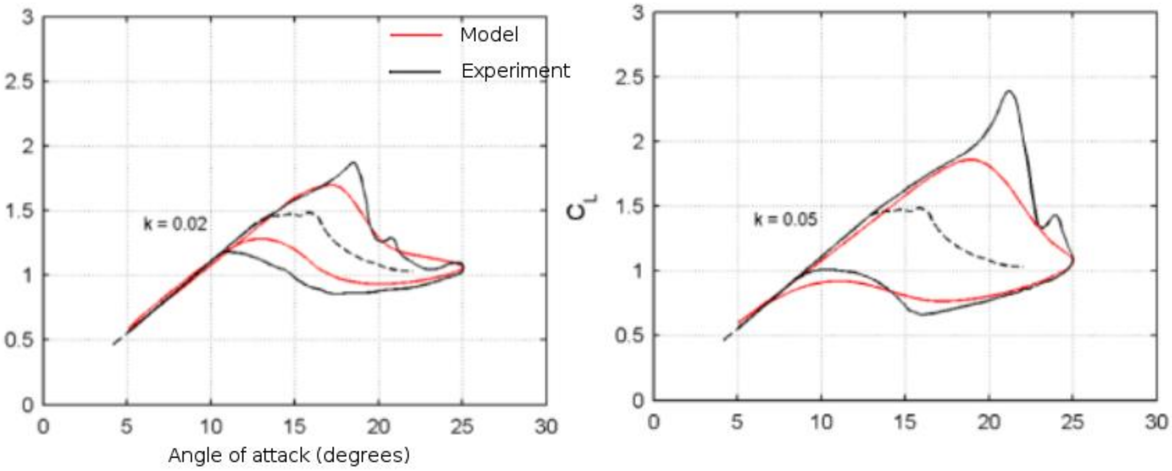

Figure 2.2 - Lift data showing secondary stall effects, adapted from [14]

2.3.3 - Unsteady Freestream

Modarres and Peters [14] modified the stall model to account for the effect of unsteady freestream. They hypothesized that the important parameter to describe the stalled behavior would be the value of freestream velocity at the point of stall. Modification of the stall model allows this circulation due to the freestream at the point of stall to be "frozen in," otherwise the simulated shed vortex would be changing strength as it traversed aft, which is not observed in reality. The equations for total lift and moment in unsteady freestream are below:

$$L_{total} = L_{linear} + F_c(U_c - U_T)\rho a\, c\, U_p + \rho U_T\Gamma_L + \rho F_c(U_c - U_T)\Gamma_L \tag{2.36}$$

$$M_{total} = M_{linear} - F_c\left(U_c - U_T\right)\rho a b^2 U_P \varepsilon + \rho U_T \Gamma_M + \rho F_c\left(U_c - U_T\right)\Gamma_M \tag{2.37}$$

$$F_c = \frac{\kappa \Delta C_L}{C_{L_{Static}} + \Delta C_L} \tag{2.38}$$

$$\begin{aligned}
U_c &= U_T & \alpha &< \alpha_{ss},\ \overset{*}{\alpha} \geq 0 \\
U_c &= U_T + \left(U_{ss} - U_T\right)\frac{\left|\overset{*}{\alpha}\right|}{\left|\overset{*}{\alpha}_{ss}\right|} & \alpha &< \alpha_{ss},\ \overset{*}{\alpha} < 0 \\
U_c &= U_{ss} & \alpha &\geq \alpha_{ss}
\end{aligned} \tag{2.39-2.40}$$

The first two terms of eq. 2.36 represent the linear lift from the airloads theory, plus a correction to maintain the same linear circulation throughout stall, since the unsteady freestream would normally modify L_{linear}. In a similar manner, the last two terms of the same equation represent the stalled loads from the primary stall model with a correction to keep the stalled circulation the same strength at the point of stall.

The Unified model is now defined, being a combination of the airloads theory in Eqs. 2.17 and 2.22, the inflow model of Eq. 2.29, the primary stall model of 2.30, the secondary stall model of 2.35, and finally the unsteady freestream corrections of 2.36-2.40. The states to be time-marched are the 2 pseudo-circulation states of the stall equation and the 8 inflow states from the inflow equation. The matrix form of the Unified model exactly as it appears in the code [32] is in the Appendix.

Chapter 3 - Optimization Process

This chapter explains the process used to find stall parameters and verify the stall model. Specific programming details are not included here, but the code is available in [32]. This code generated all of the results in Chapter 4; and any mention of code, or of implementation, refers to it. Much of the code is convenience functions, such as plotting and formatting methods, which are unimportant for the stall model and will not be detailed here.

The unified model as developed in the previous chapter is implemented in the Julia™ language as a state-space model. The equations are used in their matrix forms, with the necessary additional states accounting for second-order equations. Each experimental case is expressed as a function of time instead of angle of attack, and fourier smoothing of the static data is applied as necessary. Static corrections are determined, and the optimization algorithm determines stall parameters that minimize a particular cost function, usually the 2-norm error between the experimental and modelled solutions. Graphs of pitching moment and drag calculated by the model are compared with the corresponding experimental cases to determine the model's accuracy. The end result is a parameter set that applies to one airfoil at a particular Mach number, load, and reduced frequency. This is the progression of events for every case investigated in this work.

Any solution to an arbitrary optimization problem can be expressed as the point in a space that minimizes a cost function. The optimization problem consists of selecting a set of 6 parameters of the modified ONERA dynamic stall equation such that the error in the load of interest (lift, pitching moment, or drag) is minimized. This error is defined as the 2-norm of the difference between the experimental and computed solutions. For determining parameters of the 12-coefficient model, 2 optimizations must be performed, one for each set of parameters. The secondary stall model requires an additional optimization for its 5 parameters, though determining these does not require as many computations (often these can be found analytically). Each cost function evaluation requires simulating several cycles of the unified model using a time-marching algorithm, such as 4th-order Runge-Kutta [33]. A typical optimization process requires approximately 1.8 million time steps of the time-marching algorithm, but every function call can be computed in parallel, greatly improving the computing time of the whole process.

To begin the optimization process, we first find an appropriate set of experimental data. These data can be from wind tunnel testing, CFD, or flight tests, but the physical constraints must agree with our model constraints. For example, all of the datasets correlated in this work are from wind tunnel tests of airfoil sections, so 2D flow conditions are assumed. If we used flight test data or wind tunnel tests of rotors, we would assume 3D flow conditions and change our inflow model to accommodate this. Using flight test data would require implementing a structural model to account for blade motions, which is outside the scope of this project. Experimental data must exhibit stalled behavior for the Unified model validation to be useful.

Collection of these experimental data usually involves digitization of plots of dynamic stall loops and static data for each load (often no static data or not enough static data is present in the original paper, in which case we use additional sources). Since the unified model is expressed in the time domain, these dynamic stall loops must be "unrolled" in time by assuming some function $\theta(\square)$, the geometric angle of attack. For wind tunnel tests, the airfoil section is usually mounted to allow sinusoidal pitching at a particular frequency, which gives us a $\theta(\square)$,but this function is sometimes slightly off from the actual angle of attack data[2], so we can also assume a sinusoidal form based on the data alone.

The static load data, C_l, C_m, C_d, must be converted into the *residual* form used in the stall equation, $\Delta C_l, \Delta C_m$, and ΔC_d. This is done by using the linear model (no stall equation) to predict static loads for all angles of attack in an experimental case, including past the stall angle where the model would no longer give accurate results. The difference between the static data and the computed load is the static stall residual ($\Delta C_l, \Delta C_m \Delta C_d$). These delta-loads are input as the forcing function in the stall equation for that particular load. The stall residuals can also be computed simply by extrapolating a straight line from the linear portion of the static data into the nonlinear angles of attack, and then taking the difference between them.

---

[2] Modarres and Ahaus have both noted small differences in the angle of attack data a source presents, and the pitching function that is supposed to produce it. Every data source in this work has discrepancies too.

A very important part of using the static data is Fourier smoothing. The e parameter appears in the last term of stall equation, multiplying the derivative of ΔC_n. When just the raw points from the static data were used, $\Delta C_n$was not smooth and its derivative was not continuous; this is due to the low resolution of the static data (usually 15-20 points), so intermediate values were linearly interpolated. This would cause the model to be overly sensitive to changes in the e_0 and e_2 parameters and the optimization algorithm could not consistently find optimum values for them. Since the model is a function of time, and geometric angle of attack is periodic, the static stall residual is also periodic in time and can be represented as a Fourier series. The series can then be truncated to smooth the peaks in the ΔC_n function, as seen in Fig 3.1. This smoothing process should not be severe enough to significantly change the static data, so testing the smooth function by running the stall model with $e_0 = 0$ and $e_2 = 0$ is necessary. The smoothing was deemed acceptable if the solution changed by less than 1%. Previous works (Ahaus [15] and Modarres [14]) did not mention any kind of data smoothing, so we are unsure if their models were found to be overly sensitive to the e_0 and e_2 parameters as well.

Static corrections are the changes to the inputs needed to account for features in the experimental data not treated by the linear airloads theory or the stall model. Compressibility of air, airfoil thickness effects, and wind tunnel wall effects are phenomena that could change the loads but would not be part of the airloads model. We do not try to specifically determine causes, as it is sometimes a combination of several; instead we have sought to minimize the number of necessary corrections, and make them the same quantities for every case. For each pitching moment and drag dataset, a user of the model only needs to find corrections to $\boldsymbol{h}_{\boxed{?}}$ and $\boldsymbol{a}$. $\boldsymbol{h}_{\boxed{?}}$ is a measure of the camber of the airfoil, but can be used to account for the lift or pitching moment curves having a constant offset. Fig 3.2 shows a NACA 0012 test from Ref [18] in which the angle of zero lift is clearly not 0 degrees, even for a symmetric airfoil; the h_2 parameter can correct for this. The "a" parameter is the location of the aerodynamic center, in semi-chords, aft of the mid-chord (a = -0.5 corresponds to the quarter-chord). We can apply additional corrections as in Ahaus [15], but we have found that correcting the camber and aerodynamic center is all that is necessary for each case we investigated. The correction factors can be determined analytically, but it is usually easier to include the determination of static corrections as part of the optimization process.

There is one other correction factor that is occasionally necessary to include: $\alpha_{⍰}$. This parameter is a constant shift in the true angle of attack of the airfoil not accounted for by the unified model. The shift in the wind tunnel data could arise from wall effects or other effects previously mentioned. We found that certain stall cases were impossible to correlate for any set of parameters, due to the stall forcing function lagging behind the experimental data, as seen in Figure 3.3. One can see that regardless of the choice of stall parameters, it is not possible to match the experimental case unless the phase of the true angle of attack was adjusted. This was not required on the majority of cases, but for a few it was extremely important.

In either the 6-parameter or 12-parameter primary stall models, parameters are optimized independently of each other. If the parameters could affect the cost function independently of each other, it would be more efficient to optimize each parameter separately while holding the others constant. This is not the case, so the parameters are all adjusted at the same time, which increases the number of combinations of parameter sets, requiring more computing time to effectively search the space of possible parameters. Each parameter set in the 12-parameter model, one set for the upstroke and another for the downstroke, are determined during separate phases. This can be done because the upstroke parameters should have very little effect on the downstroke portion of the solution, and vice-versa, reducing the number of possible combinations to be searched in the 12-parameter system. The upstroke parameters are determined first, with an arbitrary set of downstroke parameters used; the upstroke parameters are then fixed while the downstroke parameters are determined. This process of holding one set of parameters constant while optimizing the other set can be repeated as desired, but usually only one cycle of this is needed. The upstroke parameters are usually unchanged after a 2nd iteration.

Once the primary stall parameters have been determined, the secondary stall optimization is performed. The region in which secondary stall occurs must be determined for a particular case beforehand because two of the secondary stall parameters depend on where in time the secondary peak in pitching moment or drag occurs. With the current secondary stall model, the parameters can be determined without any optimization from the difference solution; however, this usually can be improved upon slightly by allowing those parameters to be an initial guess for the optimization routine. Given how quickly the entire optimization process takes, this can be done with very little extra computing time. A final optimization of the primary stall parameters can be performed after the secondary stall parameters are determined, but this rarely affects the final solution.

The primary stall parameters are constrained in order to restrict the stall equation to produce qualitatively accurate solutions. While the optimization process would likely find the qualitatively accurate solutions, by restricting the space to only include them, we can greatly reduce the computation time. The primary stall equation should produce a solution with similar behavior to that of a harmonic oscillator driven by the static stall curves. This restricts the ω_0 and η_0 terms to be > 0 in order for the equation to be statically and dynamically stable. Furthermore, while the ω_2 and η_2 terms can be negative, they should not allow the stall equation to become unstable for a significant portion of the stalled region. Usually we restrict η_0 and η_2 such that $\eta_0 + \eta_2 \Delta C_l^2 > 0$, for all angles of attack.

Every set of stall parameters is associated with a particular Mach number, M, and reduced frequency, k. The static data associated with each case are also dependent on Mach number. One of the goals of this semi-empirical model, similar to the goals of the previous modified ONERA stall models, is to produce a single set of parameters for a particular airfoil at a given Mach number that can be used to determine loads during dynamic stall for a range of reduced frequencies. The goal of the previous work was to provide a process to determine parameter sets that would be independent of reduced frequency, but for this current work, each test case is allowed to have significantly different parameters for different reduced frequencies. One can modify the cost function used during the optimization in order to select a parameter set that is independent of reduced frequency, but this kind of cost function must simulate several cases independently, so the computing time necessarily increases.

Various cost functions can be used with the optimization algorithm; all of our cost functions use the 2-norm error between the experimental case being examined and the modelled solution. In the interest of computation time, only a single experimental case is compared for a set of parameters to determine cost, except for the results in section 4.6 Ahaus in Ref. [15] has used a cost function that calculates the weighted average of the errors for multiple test cases, which effectively requires multiple time-marched simulations. The effect of the weighted-average cost function is to produce a set of parameters that applies to a range of reduced frequencies. A non-weighted cost function like this is used for the results in 4.6.

Since the work here deals with cases that exhibit secondary stall behavior, it is often useful to determine the set of primary stall parameters that closely matches the so-called "smooth curves" drawn through the experimental data. This smooth curve is created to resemble a solution that the primary stall model can match that also allows the secondary stall model to capture the effects of the secondary peak. An example of a smooth curve is shown in Figure 3.4, where the difference between the experimental and computed solutions resembles a simple damped harmonic oscillation. Once the secondary stall model is enabled, the entire solution closely matches the experimental data. If just the optimal primary stall solution was used instead of a smooth curve, it will often result in a curve that does not produce a difference solution that looks like the desired pulse response. The production of the smooth curves for experimental cases is largely arbitrary, so they can be either manually drawn or automated via splines or other means. We have opted to manually determine smooth curves for this work.

Once the primary stall parameters (and secondary if necessary) are found, a case is finished. The parameters are then saved to be used as an initial guess for future optimizations, if needed, or for future users of the stall model. The process, not parameters, should be seen as the end goal for this work, since a user will eventually apply it to their own data to determine their own parameters.

The optimization algorithm used here is “Simulated Annealing”, a technique first described by Kirkpatrick et al in [34]. This choice of optimization algorithm was not motivated by the stall parameter problem in particular, but instead of its ease of implementation. Genetic algorithms, as used in previous works, can efficiently solve these kinds of optimization algorithms as well, but since we had code for simulated annealing already available, it was easy to adapt it. We imposed only a few requirements on the algorithm: it must be at least as computationally efficient as previously used optimization routines from the MATLAB standard library, and it must be a parallel implementation that can easily scale across multiple processors. These constraints are not simply for convenience, since with limited time and computing power available, our options for test data would be reduced by a slower implementation.

The optimization algorithm used is non-deterministic, so a collection of final parameter sets is kept for each experimental case. If the parameters all produce solutions which differ qualitatively but have acceptable and similar costs, more work is needed for those cases; this may also indicate something in the code is incorrect[3].

The computational efficiency of the model is extremely important for its application in flight simulators and on-board flight computers. It is a necessity that the physical models in such applications are able to run and update in real-time, since pilots will be using the simulations in real-time. This only applies to the models, and not the whole optimization process, which will always take a non-trivial amount of time. The current implementation of the optimization process in Julia benefits greatly from the fast implementation of the model; optimizing cases in the previous work [14] would occasionally take hours, but usually single cases only require 5 minutes in the current work (this figure varies greatly based on how quickly transient solutions decay). A large part of this benefit stems from being able to execute the optimization algorithm in parallel.

3.1 Frozen Inflow Method

There is a method in the code we call the "frozen inflow method" to speed up the optimization by a factor of 9, but at the cost of accuracy. This was not used in the previous work. The optimization is concerned with the calculation of $\Gamma_{\square}$, the pseudo-circulation that is the basis of stall corrections, using equations 2.30 and 2.31. The two equations representing pseudo-circulation in state-space depend on the inflow equations through the $\Delta\square_{\square}$terms in the stall parameters, and the $\Delta\square_{\square}$ term and its derivative in the forcing function. This is due to inflow affecting angle of attack, and because the inflow depends on the pseudo-circulation, the equations are coupled. However, the effect of the stall equation

---

[3] Before using Fourier smoothing on the static data, the algorithm could not consistently find useful "e" parameters

is small on inflow, making the change in angle of attack small, and so the effect on the stalled loads is also small. The inflow equation (2.29) is repeated below, with the stall feedback highlighted:

$$\{\dot{\lambda}\} = [A]^{-1}\left[\{c\}\left(\{e\}^T\{\dot{v}_n + \ddot{h}_n\} + \frac{u_0}{b}\{f\}^T\{\dot{h}_n\} + \frac{\dot{\Gamma}_0}{2b\pi}\right) - \frac{u_0}{b}\,\{\lambda\}\right]$$

Figure 3.5 shows the computed stalled pitching moment using the normal model, in blue, and using the model without including the stall feedback in the inflow equation, in red. For this particular case, and many others, there is almost no difference between using the stall circulation and removing it from the inflow equation. Time marching the 8 inflow states takes the majority of the computing time during an optimization, but since the coupling is small, we created a shortcut: the inflow from a previous optimization is saved and used as a *lookup table* instead of being recalculated for each differing set of stall parameters. This decouples the equations, and the optimization algorithm now uses the same exact history of inflow states for every cost function evaluation regardless of the stall equation. This is inaccurate and technically incorrect, but the cost to the overall accuracy is small until the optimization closes in on a solution. Between running cases, normally the cost function should not change at all, since the algorithm can never do worse than the best result from the previous run; the frozen inflow method can break this rule, however, since the inflow is allowed to change, which is how we know when the method cannot improve the solution anymore. The final cost function value for a run will be better than the first cost function value for the next run, so at this point we can switch back to the original model. This process of using the frozen inflow method first and switching to the original model after a few runs can save an enormous amount of time.

Creating the lookup table for the frozen inflow method is more involved than just saving the states from a previous simulation. The 4th-order Runge-Kutta algorithm uses half steps in time when calculating the derivative, so a previous simulation needs double the number of states available when using this method. At the beginning of a frozen inflow optimization, a simulation is evaluated at twice the number of steps inputted by the user. These states are saved and used instead of evaluating the 8 derivative equations in Karunamoorthy model. This also requires a different implementation of the Runge-Kutta algorithm that uses an integer index instead of an arbitrary time value to calculate its output.

All of the results in Chapter 4 were generated using the frozen inflow optimization method first, using the normal method afterwards if a better solution was possible.

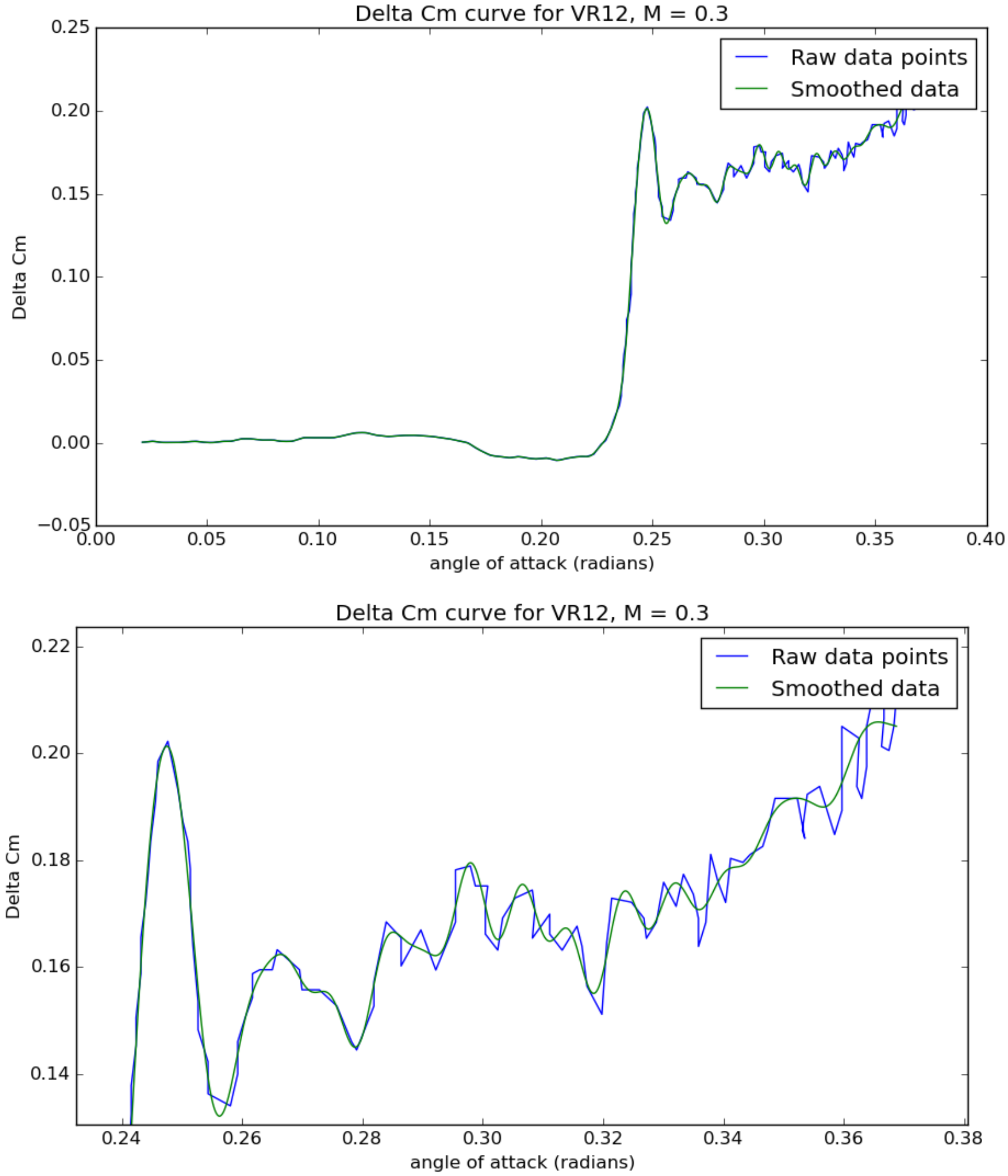

Figure 3.1 - Smoothed ΔC_mdata; fourier series truncated to first 100 terms

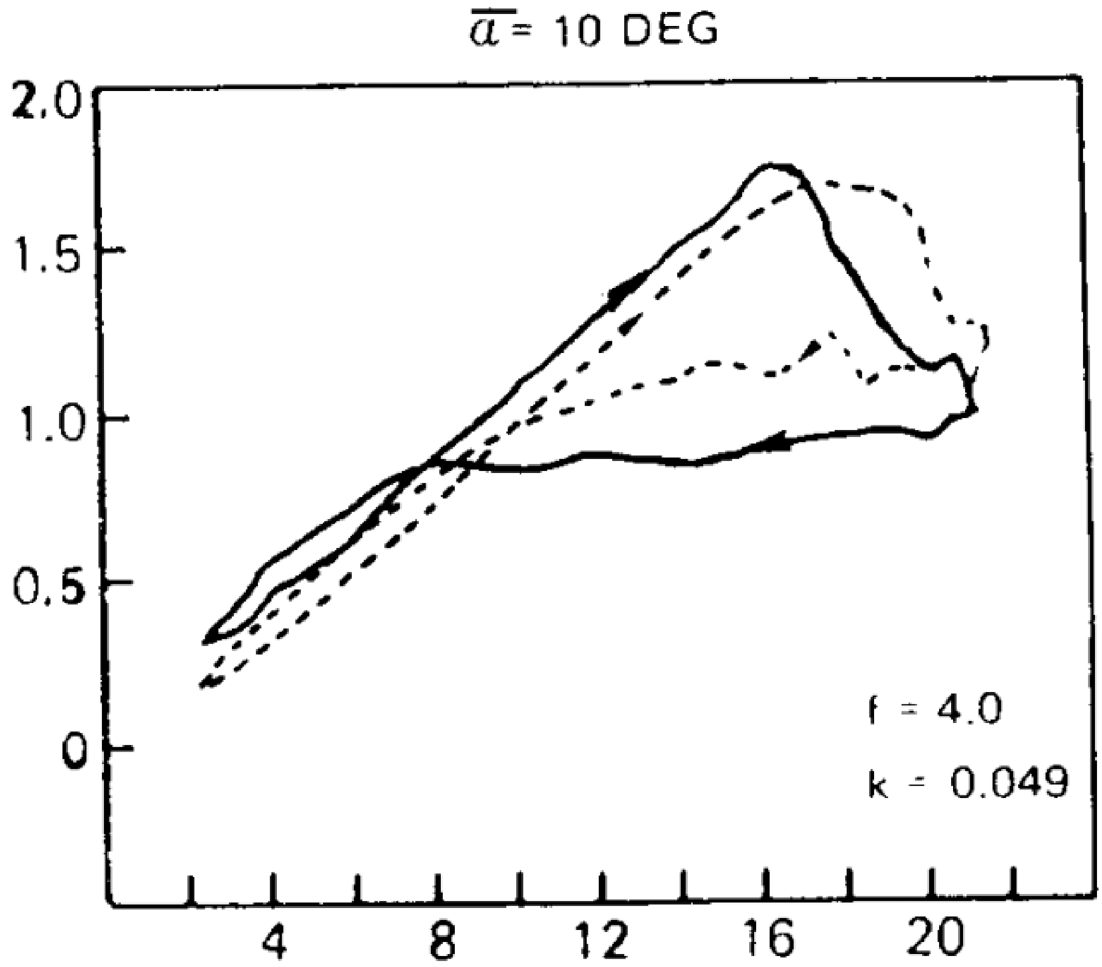

Figure 3.2 - Lift coefficient vs Angle of attack from Ref [18], showing a nonzero lift offset, even for a symmetric airfoil (NACA 0012).

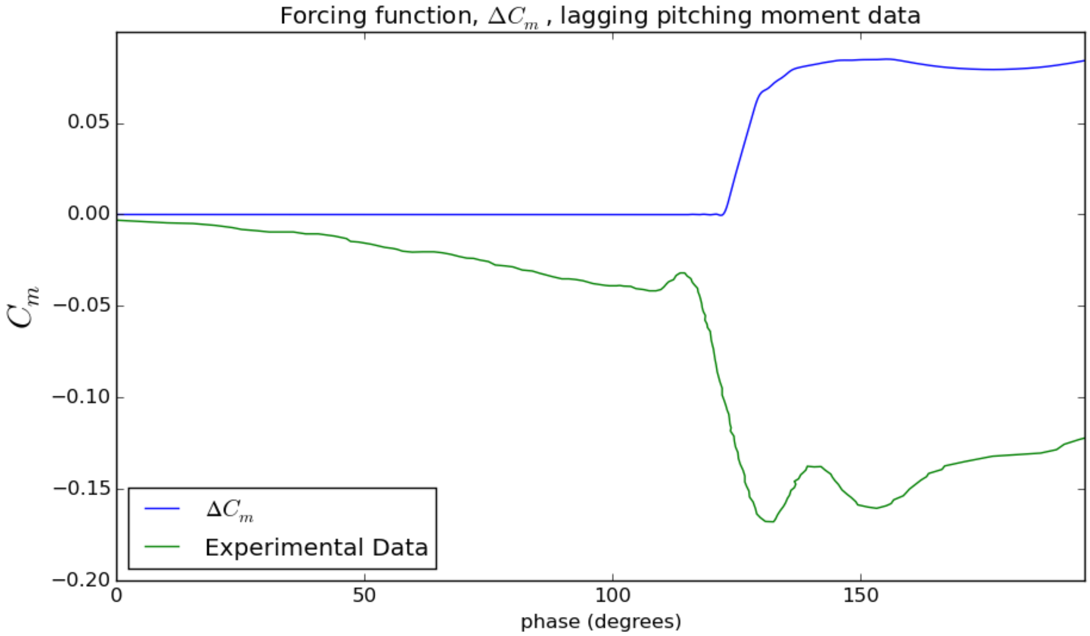

Figure 3.3 - Phase difference between forcing function and pitching moment data

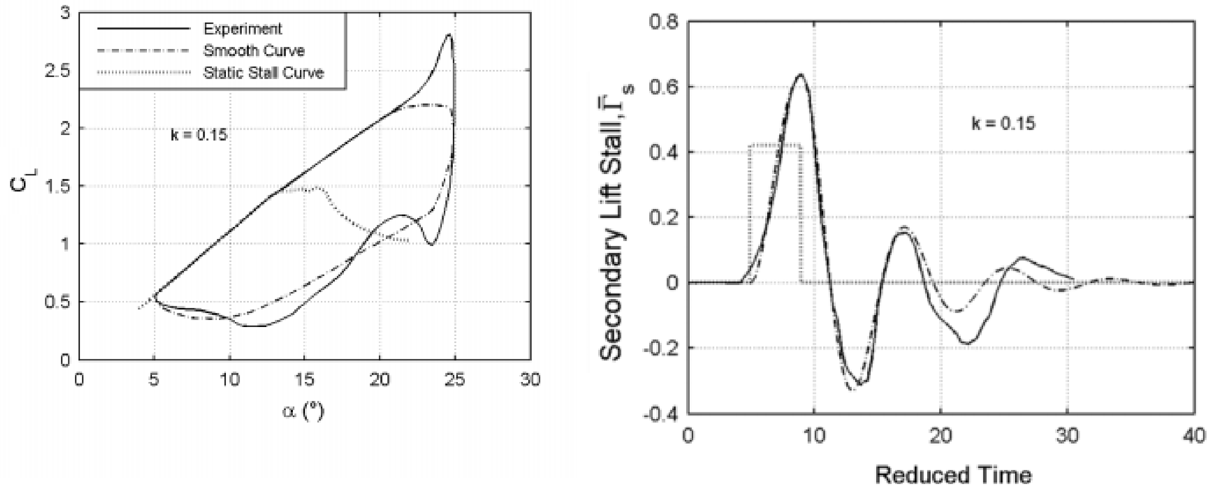

Figure 3.4 - Example of a smooth curve for lift, taken from [14]

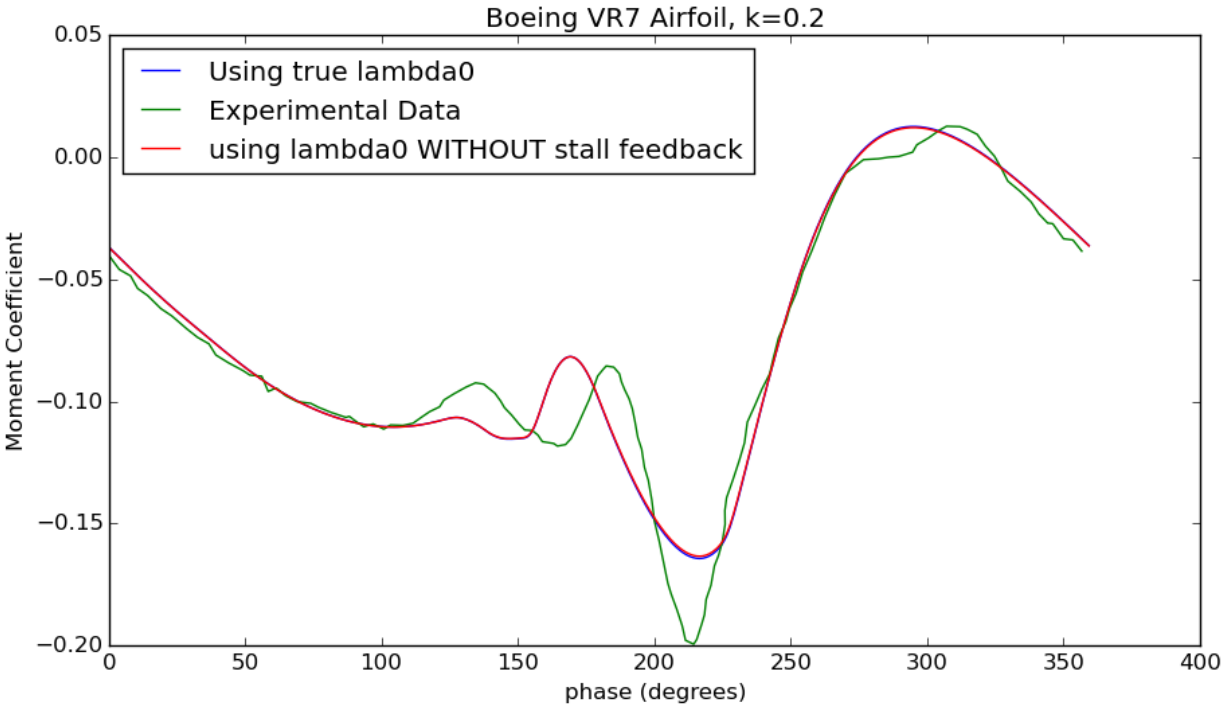

Figure 3.5 - Comparison of stalled loads with and without stalled feedback in the inflow equation.

Chapter 4: Results

The Unified model correlations are divided into 6 sections: *VR-12, VR-7, NACA 0012 Yawed, NACA 0012 Unsteady, SSC-A09 Unsteady,* and *VR-7 for a single set of parameters*. All of the results from each dataset were generated by the same procedure outlined in Chapter 3. Each plot contains the experimental data in green, the modeled solution in blue, and, if applicable, the modeled solution including the secondary stall effects in red.

4.1 Boeing VR-12

The first results are correlations from the data in Ref [16], a wind tunnel test of a harmonically pitching Boeing VR-12 airfoil, the same data investigated in Ahaus [15]. The test is meant to evaluate the effectiveness of a Variable Droop Leading Edge (VDLE) airfoil for lessening the effects of dynamic stall on a retreating helicopter blade. The VDLE configuration is effectively a dynamically morphing airfoil, well suited to be modeled by the Johnson airloads theory, and Ahaus considered both morphed and unmorphed configurations. However, for this work we only consider the baseline (unmorphed) data. This is because Ahaus already validated the effects of morphing on pitching moment and drag, so we are more interested in the stall effects. The Mach numbers of the tests are 0.2, 0.3, and 0.4, with 2 reduced frequencies, k = 0.05 and k=0.1. Lift, pitching moment, and drag dynamic data are all present, but drag static data was only present for the M=0.3 case, which is why the M=0.2 and M=0.4 cases are not evaluated. The geometric angles of attack vary sinusoidally from 0 to 20 degrees, with a mean angle of 10 degrees for each experiment, according to the following expression:

$$\theta = \theta_m + \theta_0 \sin(\omega t + \phi)$$

, where θ is the geometric angle of attack. CFD data is available from the same reference, though it shows poor correlation for several pitching moment and drag cases, and will not be evaluated here.

The VR-12 results are shown in Figs [4.1-4.8]. Each figure is plotted in angle of attack and phase and the experimental data, primary stall, and primary + secondary stall are shown in green, blue, and red, respectively. The pitching moment results of [4.1-4.6] show close agreement with the experimental data for each Mach number and reduced frequency examined. The secondary stall model provides a small improvement to the k = 0.05 results around the small secondary peak in pitching moment (secondary peaks occur between phases of 120 to 180 degrees for Figures 4.1-4.3). The same static corrections ($h_2$and a) were used for every case.

4.2 - Boeing VR-7

Data from Ref [17] were obtained in a water-tunnel test of a Boeing VR-7 airfoil. They contain the largest range of reduced frequencies of any data we used, with k values ranging from 0.002 to 0.25. Ref [17] evaluates the original ONERA stall model with experimental data taken from the Aeromechanics Laboratory Water Tunnel at NASA Ames. The airfoil section was placed a water tunnel with minimal side clearance, attached to a pitch transducer at the quarter-chord to allow simple harmonic pitching. No plunging or side motion of the airfoil was allowed, as it was fixed in these directions. The water velocity in the tunnel was set to produce a dynamic pressure of 689 N/m^2, corresponding to a reynolds number of 120000. The airfoil section oscillated sinusoidally, with a mean value of 10 degrees, and an amplitude of 10 or 15 degrees.

Cases were evaluated for reduced frequencies of .05, .1, .15, .2, and .25 (the k=0.002 data is quasi-static, and is not used). Since the original ONERA model relied on determining parameters from much smaller-amplitude tests, this data is available as well, with amplitudes of $\sim$2 degrees and means values from 0 to 18 degrees. This is not necessary for the parameter identification in the Modarres-Peters stall model, so only the large amplitude data will be used, since the large-amplitude data is more representative of the aerodynamic environment of real helicopter blades. Both pitching moment and drag data were evaluated. Only one set of static data was necessary since the compressibility effects were negligible (due to the increased speed of sound in water, this data effectively has a Mach number of 0). This is the only data to provide plots with both angle of attack and reduced time, so we did not need to assume the sinusoidal form from the data as described in Chapter 3. This is the same dataset that will be used for the last set of results that attempt to match all of the VR-7 data for a given load with the same set of parameters.

The VR-7 results for pitching moment in Figs [4.9-4.13] show some interesting characteristics. First, the data shows significant multiple vortex shedding phenomenon for the reduced frequencies higher than 0.1. The multiple peaks present in the data do not resemble the normal secondary vortex behavior, like what was observed in Section 4.1, where a smaller peak is following the single large peak. The smaller peaks leading the larger peaks are an interesting stall phenomenon not present in the other datasets. The Unified model matches the linear region well and the stalled region fairly well for each case. For this dataset in particular, the optimization routine had a difficult time finding parameter sets that reached the same peak values as the data, which is a concern for load modelling. In an application where peak loads are critical, the stall model would need to be corrected. This could be done by implementing composite cost functions that try to minimize error and put additional weight on the peak value being close to the data (perhaps erring on the side of predicting larger loads than is present in the data). These kinds of cost functions were not tested.

4.3 NACA 0012 Yawed Flow

Ref [18-19] is a wind tunnel experiment of a NACA 0012 airfoil pitching harmonically in a steady freestream. Since we are not investigating flight tests or other 3D data, this paper is our only source of data taken at swept geometries. This source contains many combinations of reduced frequencies and pitch angle ranges, with yaw angles of either 0 or 30 degrees. Static data for every load at both yaw angles is also provided. Modarres [14] validated 3 reduced frequencies of this data for lift, so we validate the same three frequencies for drag and pitching moment: 0.037, 0.075, and 0.093. The data at these three reduced frequencies is for a Mach number of 0.4, with a pitch range of 4° to 20°.

This dataset introduced some interesting problems. The pitching moment data show what appears to be a constant component of the moment on the airfoil that changes depending on reduced frequency and yaw angle. Figure 27 of Ref [18] strongly exhibits this trait for the $\bar{\alpha} = 10$ degrees cases, which is not the data we correlated. We cannot account for anything aerodynamic that would cause this phenomenon, especially since the same constant component of pitching moment should be independent of reduced frequency, as it was for other cases validated in this work. We believe this indicates a physical error in the testing apparatus of the wind tunnel, possibly an axis of rotation that is changing slightly with each test. Normally we use a single value of h2 to correct for any effect of "virtual camber" on a dataset, but in this case we make an exception to allow a different h2 for each case. We would be otherwise unable to get the optimization routine find decent parameter sets.

The results for the stall model on this dataset, Figures [4.19-4.30], showed close agreement for both pitching moment and drag, yawed and un-yawed cases. Oddly, some of the cases still showed a constant offset in the results even after correction for it during a no-stall simulation. Both yawed and un-yawed results show peak values close to the data and stall loops that are close in size to those in the data, so the effect of stall flutter would not be under predicted. Many more figures are available from Ref [18], and also Refs [35-36], for more stall model validation.

4.4 NACA 0012 Unsteady Freestream

The wind tunnel test of Ref [21] is a NACA 0012 airfoil section in a subsonic wind tunnel. With a maximum speed of 25 m/s, the Reynolds number of the tests range from 50,000 to 400,000. The unsteady freestream is simulated via the motion mechanism attached to the airfoil; combinations of pitching, plunging, and fore-aft motion can be induced, and the phasining between the types of motion can be varied. The pitching occurs via a shaft at the quarter-chord of the section. Several combinations of pitch range, reduced frequency, and unsteady freestream amplitude are available, for the sake of brevity, we have limited the analysis to only the drag data of Figure 3 in Ref [21]. There are nine cases investigated here, one with steady freestream and eight with unsteady freestream. The reduced frequency is 0.135, the amplitude of unsteady freestream is 0.153, and the pitch range is 3° to 15°. The unsteady freestream and pitching functions are the following:

$$V = V_{\infty}(1 + \lambda cos\omega t)$$

$$\alpha = \alpha_0 + \Delta\alpha\cos(\omega t + \phi)$$

, where λ is the unsteady freestream amplitude and ϕ is the phase difference between the two functions. ϕ is varied between each unsteady case in 45 degree increments, from 0° to 315°.

The results for all of the unsteady cases, Figures [4.32-4.39], use a parameter set optimized for the steady case only, Fig 4.31. All of the cases show decent agreement with the experimental data (since the experimental data does not change very much for each ϕ), but they also reveal that we have a bias when looking at these plots. Every plot in phase looks much better than the plots in angle of attack, but they have the same 2-norm error. We believe the phase plots better represent the true nature of the model since the model is based in time, but this also indicates how additional validation through other means than what was done here, in Ahaus [15], and in Modarres [14], is necessary. How accurate the stall model is for a given dataset should not be dependent on the method we chose to plot the results with, nor should it be just a quantitative measure of that visual difference we discern when looking at the plots. A real-world application of the stall model needs to be used as feedback for a better way to formulate cost functions and determine parameters.

It should be noted that the same authors of this data paper [21] also have pitching moment data available in another source [20], but this data posed some issues. In figures 5 and 6 of [20], the pitching cases show extremely large peaks in moment and drag, several times the magnitude of the static data. We were unable to get the stall model to correlate this without making much larger corrections outside of the simple static corrections we elect to use for every other dataset. It may require additional changes to the model, or the dataset itself might be suspect. The plunging data for the same angles of attack shows much smaller loads for pitching moment and drag, but similar loads for lift, which makes us hypothesize that the experiment could have some physical problem. The pitching moment data shows a large region of negative damping that may have caused the apparatus to go unstable.

4.5 SSC-A09 Unsteady Freestream

The experiment of Ref [22] is of a blowdown wind tunnel, which can produce much higher mach numbers than the other unsteady experiment of Ref [21]. A high pressure (17

MPa) tank of air is connected to the tunnel allowing a fast gust of air to reach the SSC-A09 airfoil test section, which can be oscillated in pitch only. The motor controlling the pitch of the airfoil can be phase-matched to the vanes controlling the gusts, so the unsteady freestream and pitch oscillations can be synchronized. Lift and pitching moment data are available from this test at reduced frequencies of 0.025 and 0.05 (approximately). The Mach number of the freestream is0.4 ± 0.07. Additional data for this experiment is available in Ref. [23], in which the freestream phasing with respect to the airfoil pitch phasing is allowed to vary.

This test is important for several reasons. First, it is the only unsteady moment data we tested. Modarres previously tested this same dataset for only one of the reduced frequencies, so it also provided a sanity-check for the implementation of the model. The small reduced frequencies and high Mach numbers of these tests are more indicative of real helicopter conditions. In lieu of 3D test data, these data are the next best thing. Lastly, this paper interpolated steady freestream tests to predict unsteady behavior, which corroborates the unsteady freestream corrections to the Unified model by Peters and Modarres [14]. The idea of holding the freestream value at the point of stall constant to give the same vortex-shedding behavior shows how the stall characteristics of steady conditions can predict stall in the unsteady freestream.

The results for the SSC-A09 data are Figures [4.40-4.45]; 4 of the results have steady freestream and 2 are unsteady freestream. Parameters optimized from the steady freestream cases are used in the unsteady cases because we are validating the unsteady corrections themselves. Ideally, the unsteady corrections with only one stall parameter set could be used for the dynamic stall of a real helicopter blade instead of trying to interpolate multiple sets of stall parameters without the corrections. The agreement between the model and experimental data in these cases shows the unsteady corrections of Section 2.3.3 effectively model the small difference between the steady and unsteady data.

It is important to note that while the model was able to match the unsteady k = 0.0506 case, this result is not as close as Modarres' correlation, and the exact cause of this was not determined. We believe the main issue is his inclusion of a cross-coupling term in the primary stall equation that is not present in our model. Equation [5.2] of Ref [14] has an additional term to allow lift data to affect the pitching moment model. It is also possible there is a discrepancy between our static corrections and his; in particular he may have used an α_s parameter that we did not include.

4.6 Boeing VR-7 with single set of parameters

This is the same dataset from Ref [17] considered in section 4.2. One of the goals of this work is to find a k-independent parameter set, so data with a large number of reduced frequencies is desired. All of the same conditions and static corrections applied to this optimization; the only part changed was to use a cost function that averaged the error from each case equally. This required 5 time-marching simulations instead of 1 for each cost function evaluation, so the optimization took 5 times as long (the frozen inflow method was able to alleviate this greatly). Results from this optimization are shown in Figures [4.46-4.55].

These results show fairly good agreement with the higher reduced frequencies, similar to the solutions of the previous VR-7 results. The lower reduced frequencies, k=0.1 and k = 0.05, have solutions that differ from the previous results. In particular, the deep-stalled region of the pitching moment results for those 2 reduced frequencies shows some very lightly-damped oscillations that are not present in the higher reduced frequencies. This would not be desirable in an application that expected the dynamic stalled behavior to approach static stalled behavior, as the model would produce oscillations for a quasi-static case. The stall parameters for the drag cases did not have this oscillating behavior; instead, the model slightly underpredicted the peak drag for the higher reduced frequency cases, and overpredicted the drag for the lower reduced frequencies. This is not necessarily a bad feature, since the consequences of underpredicting loads could be worse than overpredicting. These results could be further improved by relaxing the requirement of one parameter set for all reduced frequencies. In order to provide close agreement with both low and high reduced frequencies, multiple parameter sets could be smoothly interpolated between as a function of reduced frequency.

Airfoil	**Mach Number**	**Reduced Freq.**	**Secondary Stall**	**Unsteady Freestream**	**Yawed Flow**	**Load Data**	**Reference**
VR12	0.2 - 0.4	0.05, 0.1	yes	no	no	Moment, Drag	[16]
VR7	Approx. 0 (water)	0.05 - 0.25	yes	no	no	Moment, Drag	[17]
NACA 0012	0.3 - 0.4	0.037, 0.075, 0.093	no	no	yes	Moment, Drag	[18]
NACA 0012	0.07	0.135	no	yes	no	Drag	[21]
SSC-A09	0.33 - 0.47	0.025, 0.05	no	yes	no	Moment	[22]

Table 4.1 - Summary of experimental data investigated

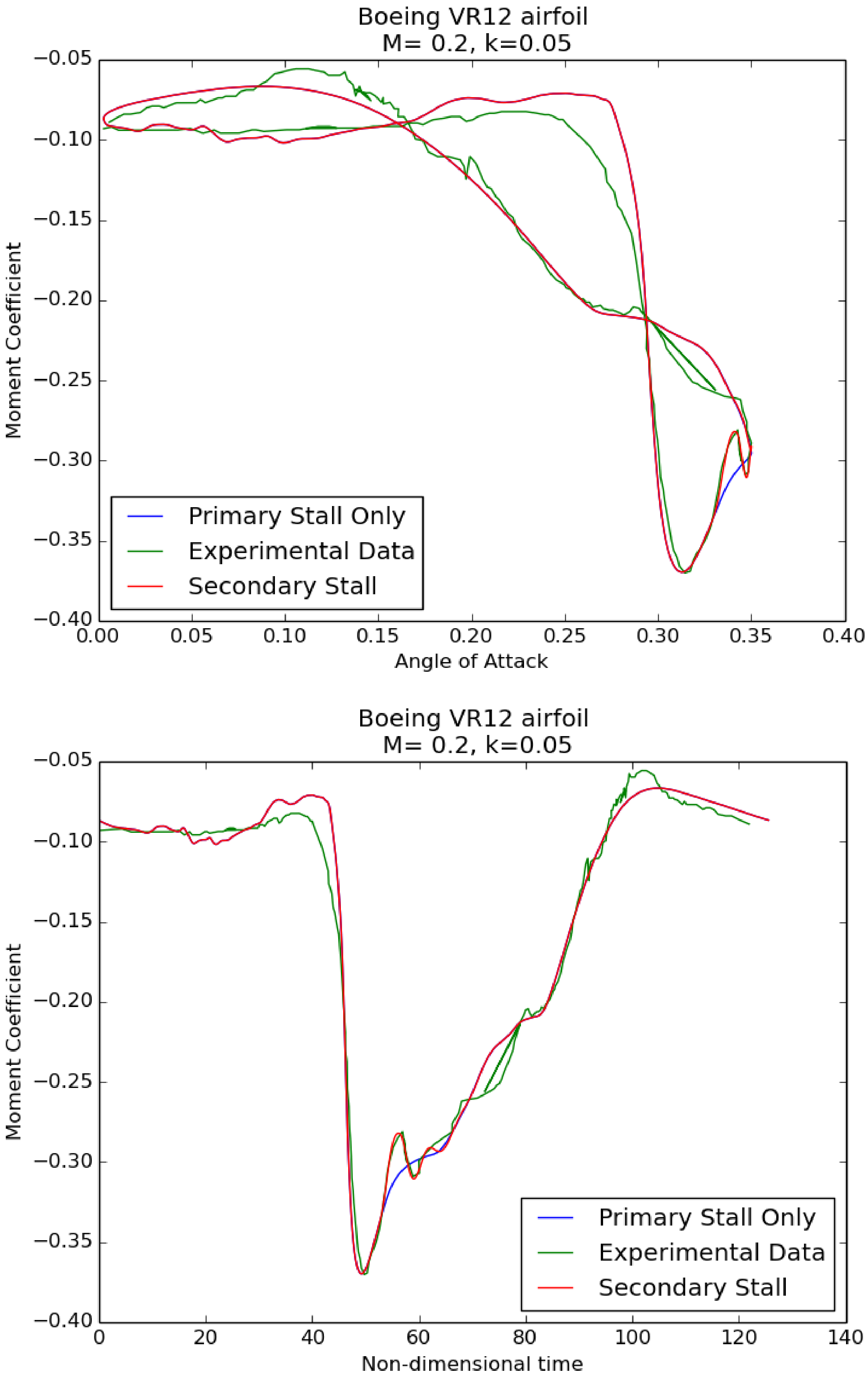

Figure 4.1 - Pitching moment solutions for k = 0.05, M = 0.2, compared to Ref. [16].

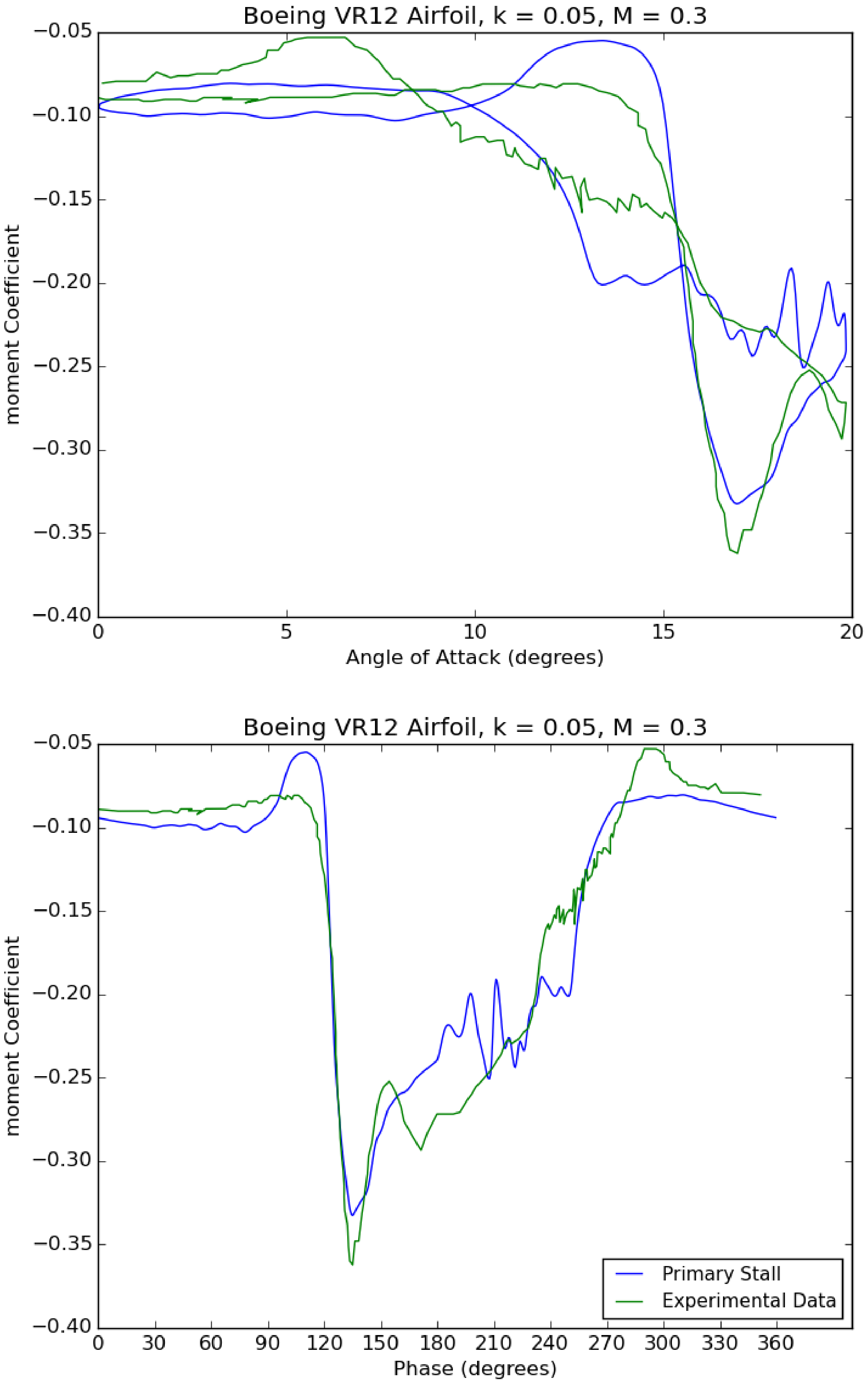

Figure 4.2 - Pitching moment solutions for k=0.05, M=0.3 compared to Ref [16]

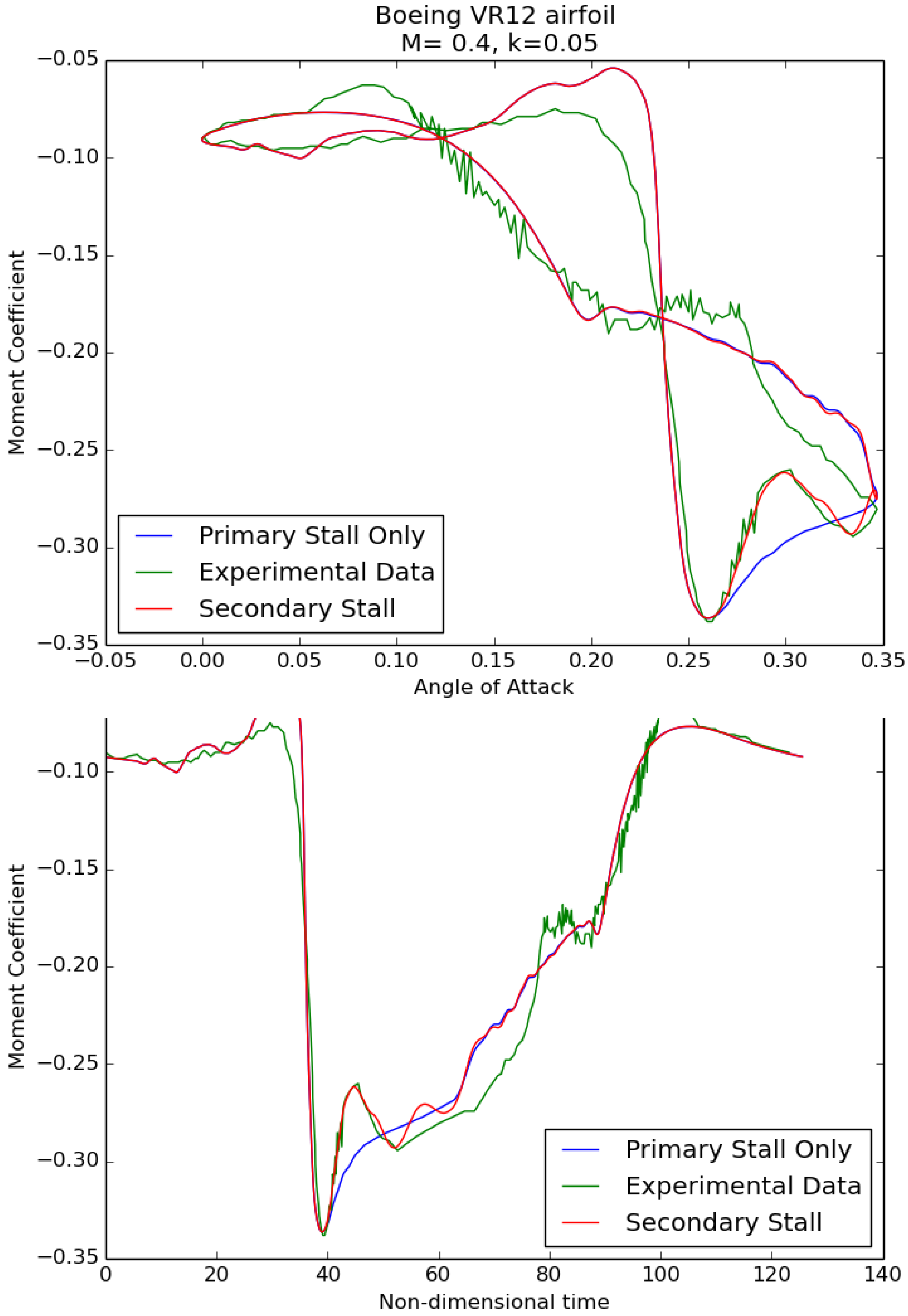

Figure 4.3 - Pitching moment solutions for k=0.05, M=0.4 compared to Ref [16]

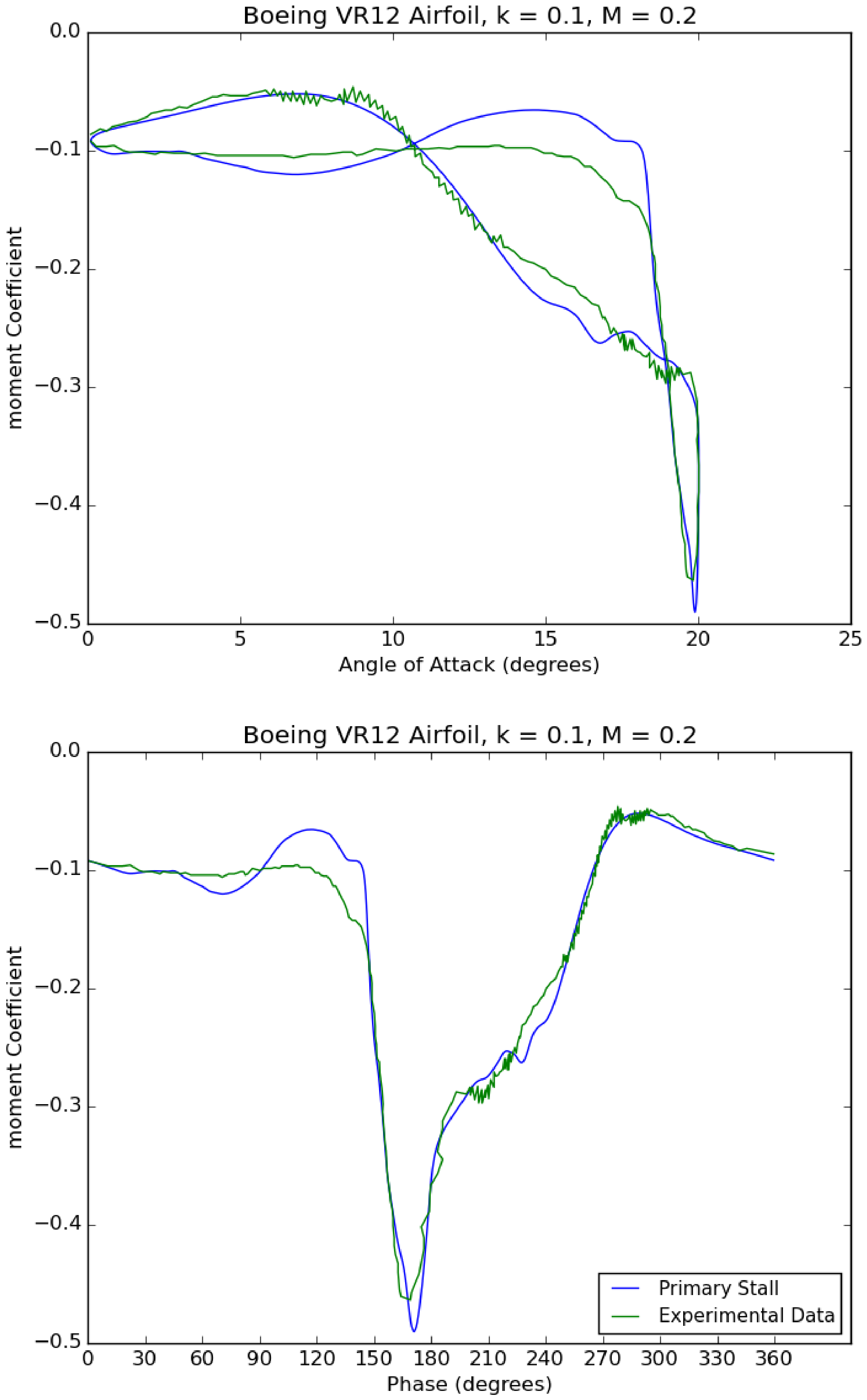

Figure 4.4 - Pitching moment solutions for k=0.1, M=0.2 compared to Ref [16]

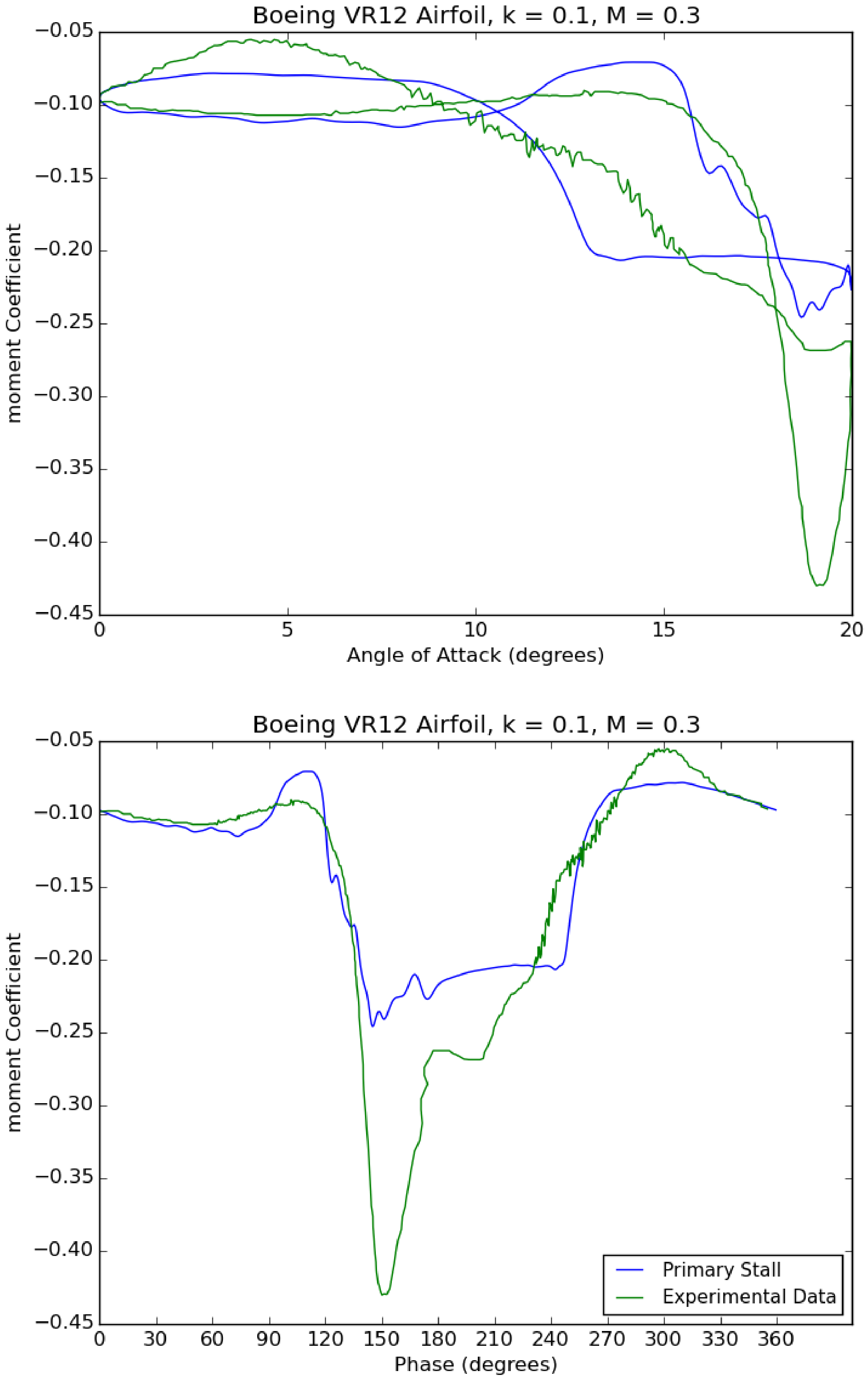

Figure 4.5 - Pitching moment solutions for k=0.1, M=0.3 compared to Ref [16]

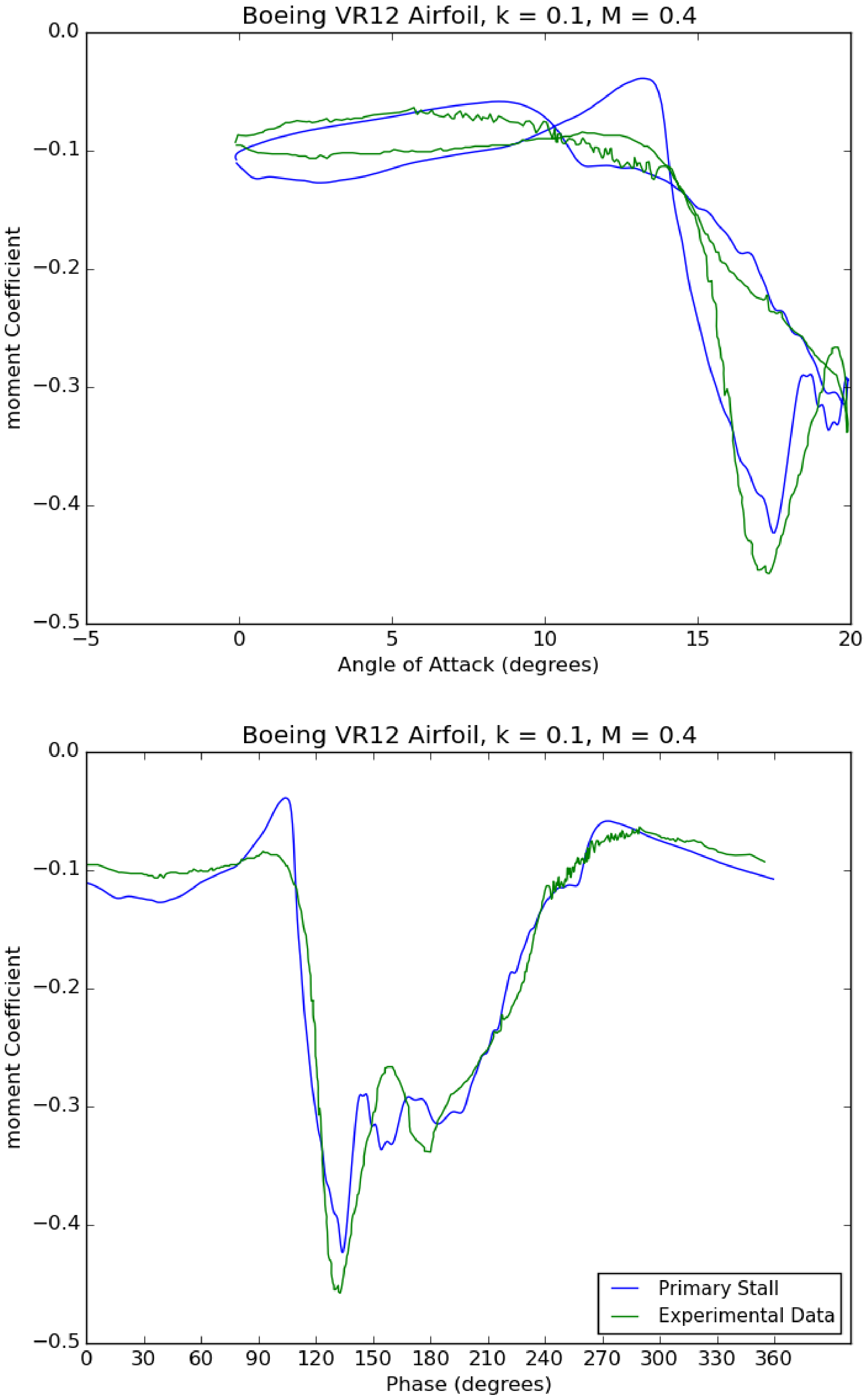

Figure 4.6 - Pitching moment solutions for k=0.1, M=0.4 compared to Ref [16]

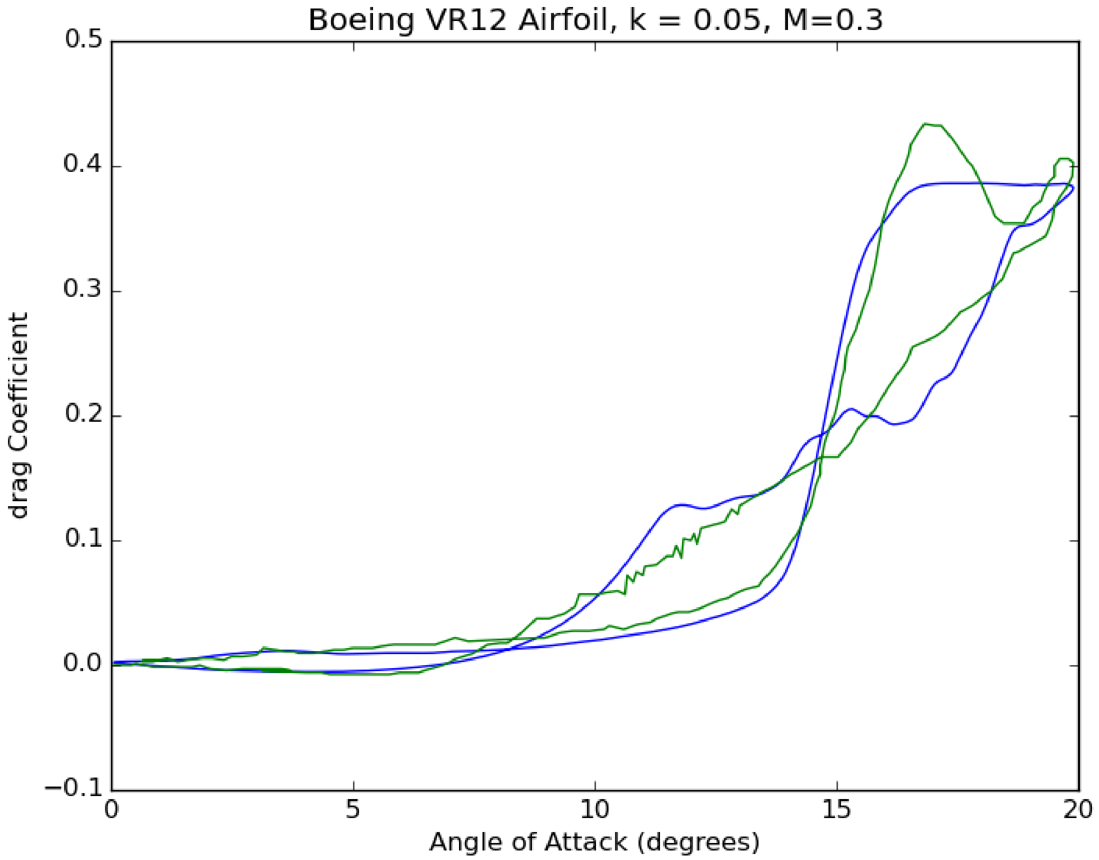

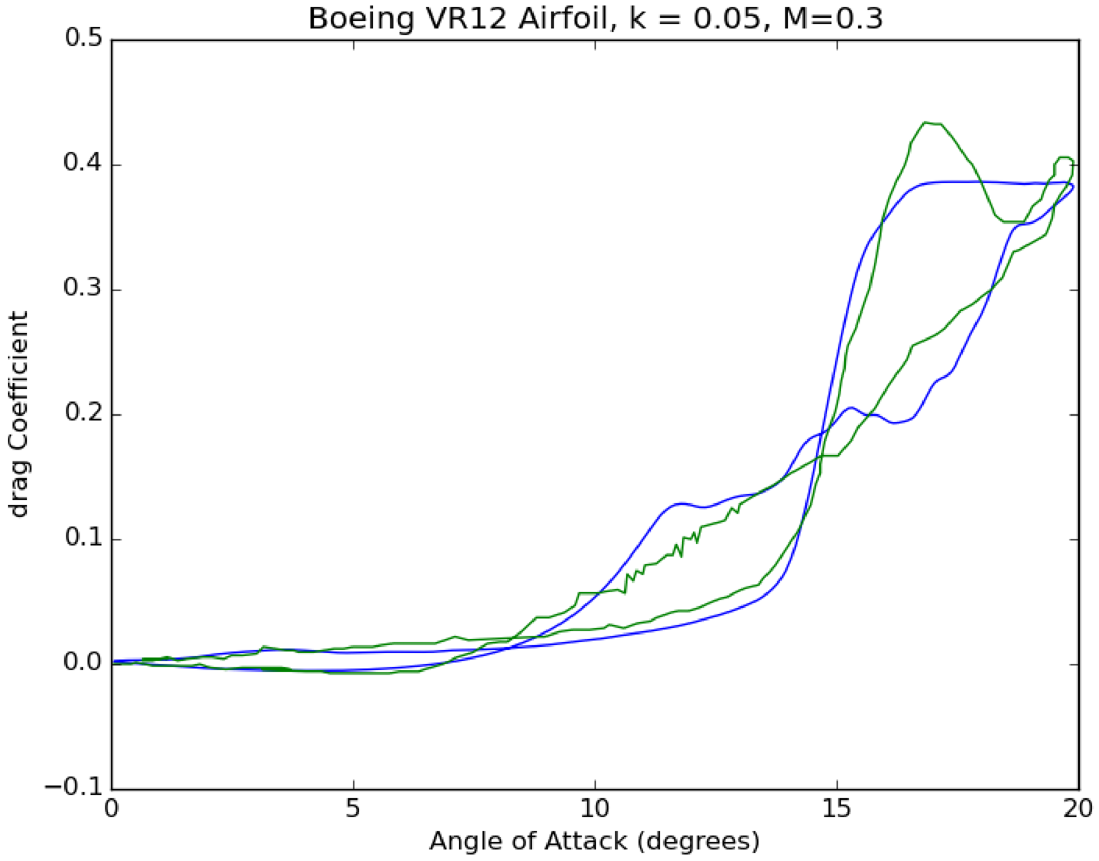

Figure 4.7 - Drag solutions for k=0.05, M=0.3 compared to Ref [16]

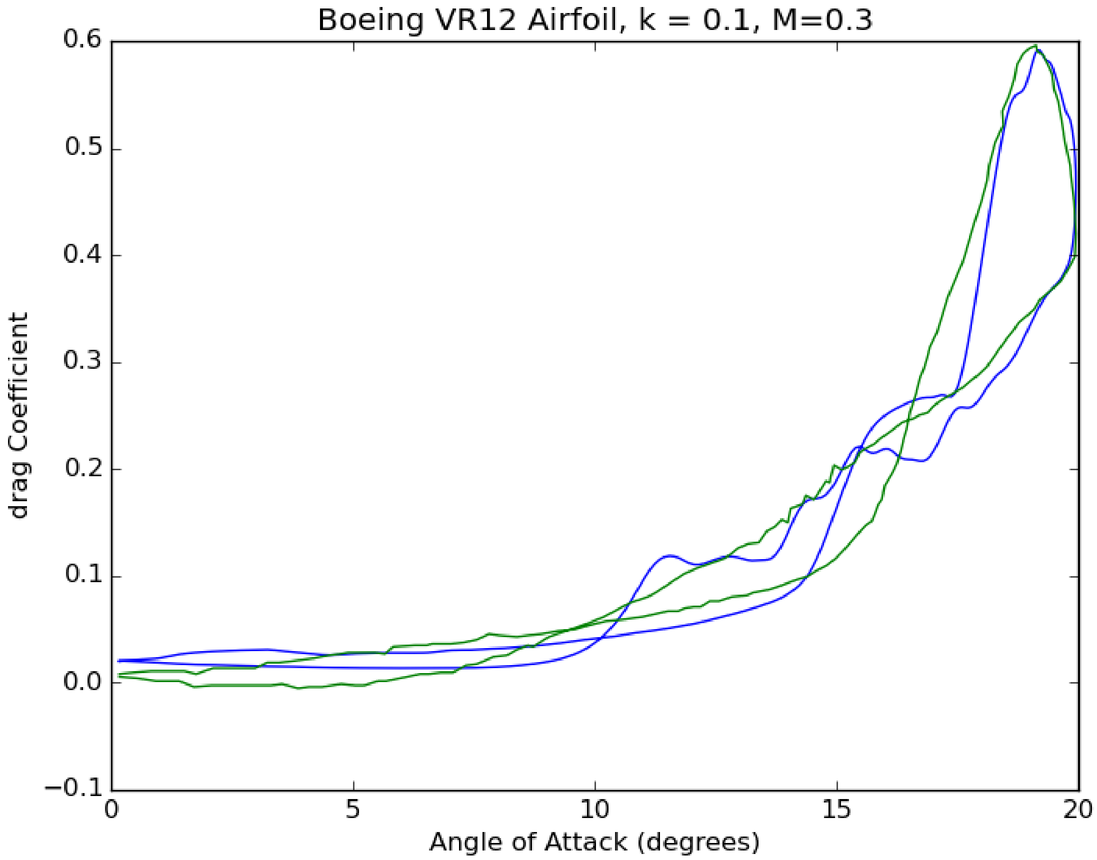

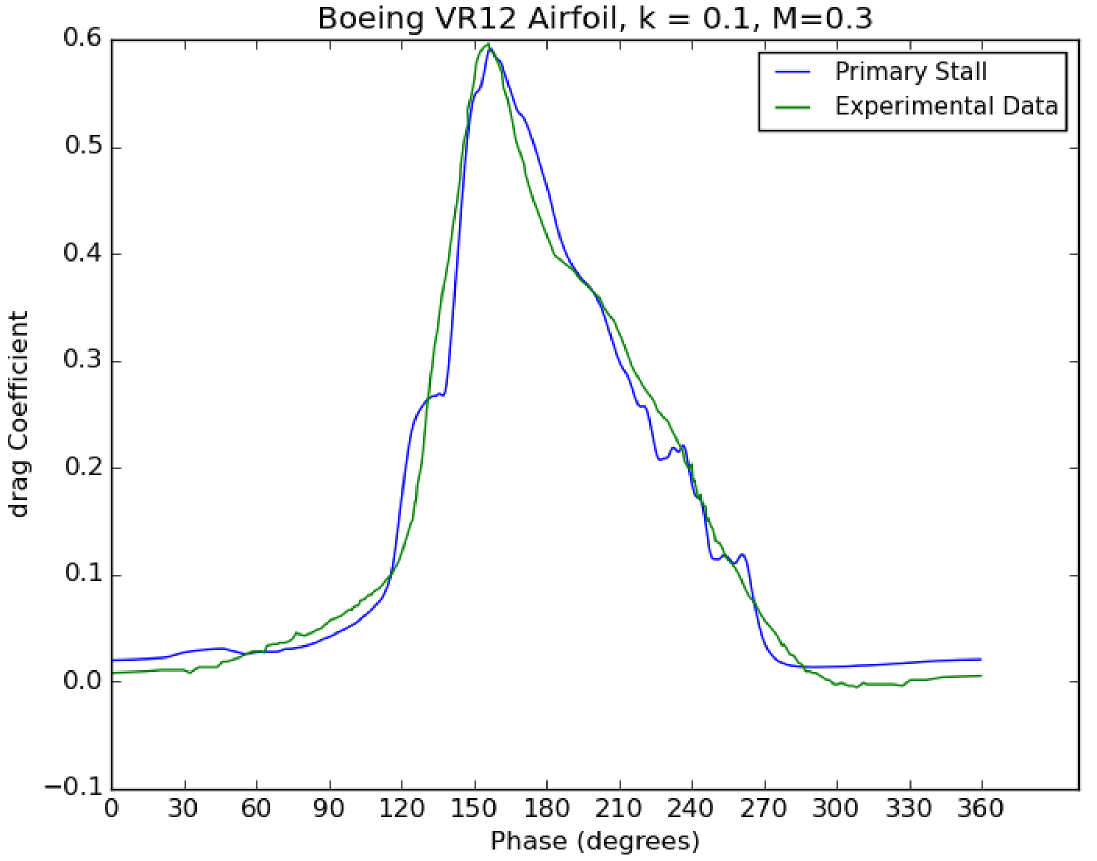

Figure 4.8 - Drag solutions for k=0.1, M=0.3 compared to Ref [16]

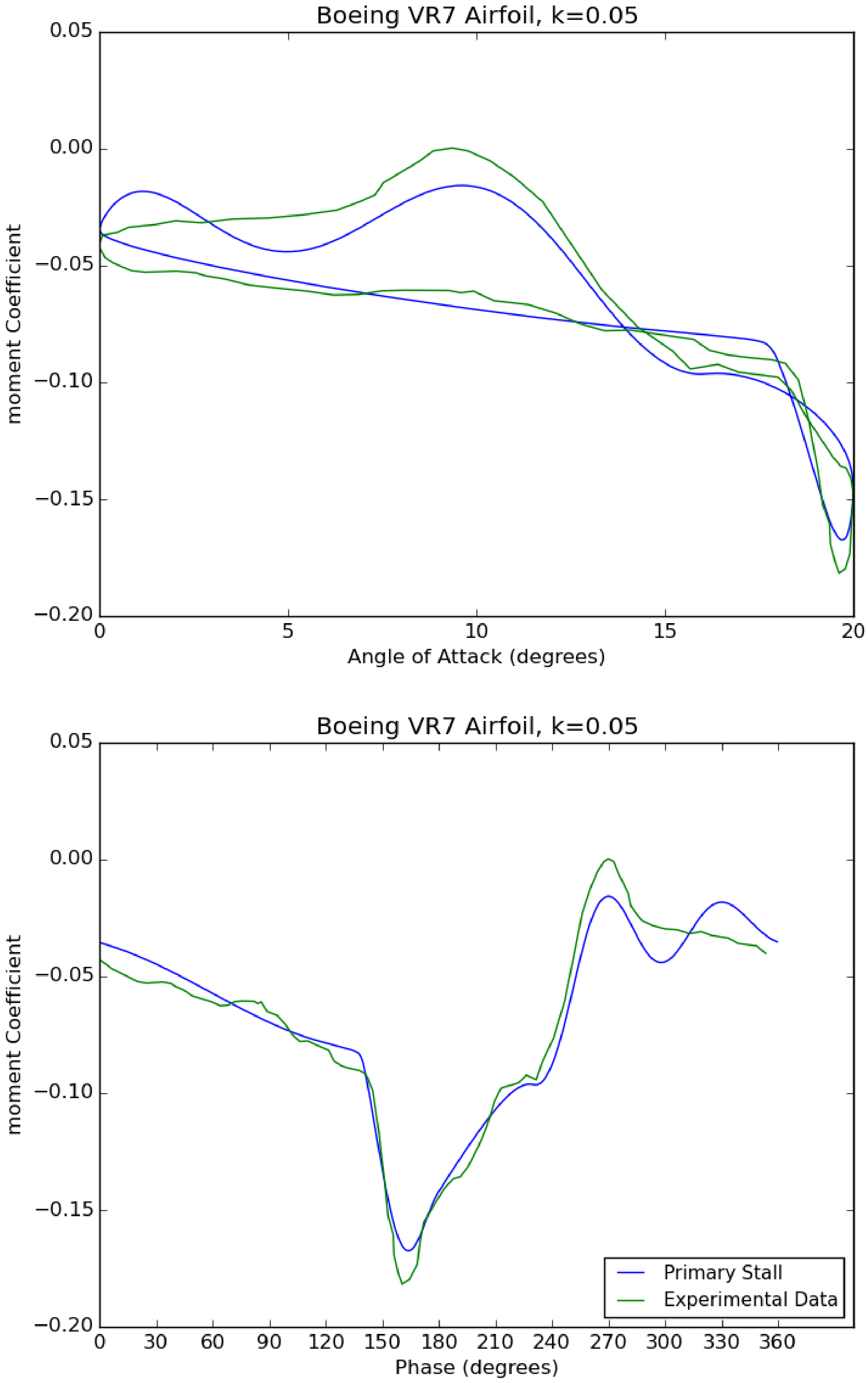

Figure 4.9 - Pitching moment solutions for k=0.1, compared to Ref [17]

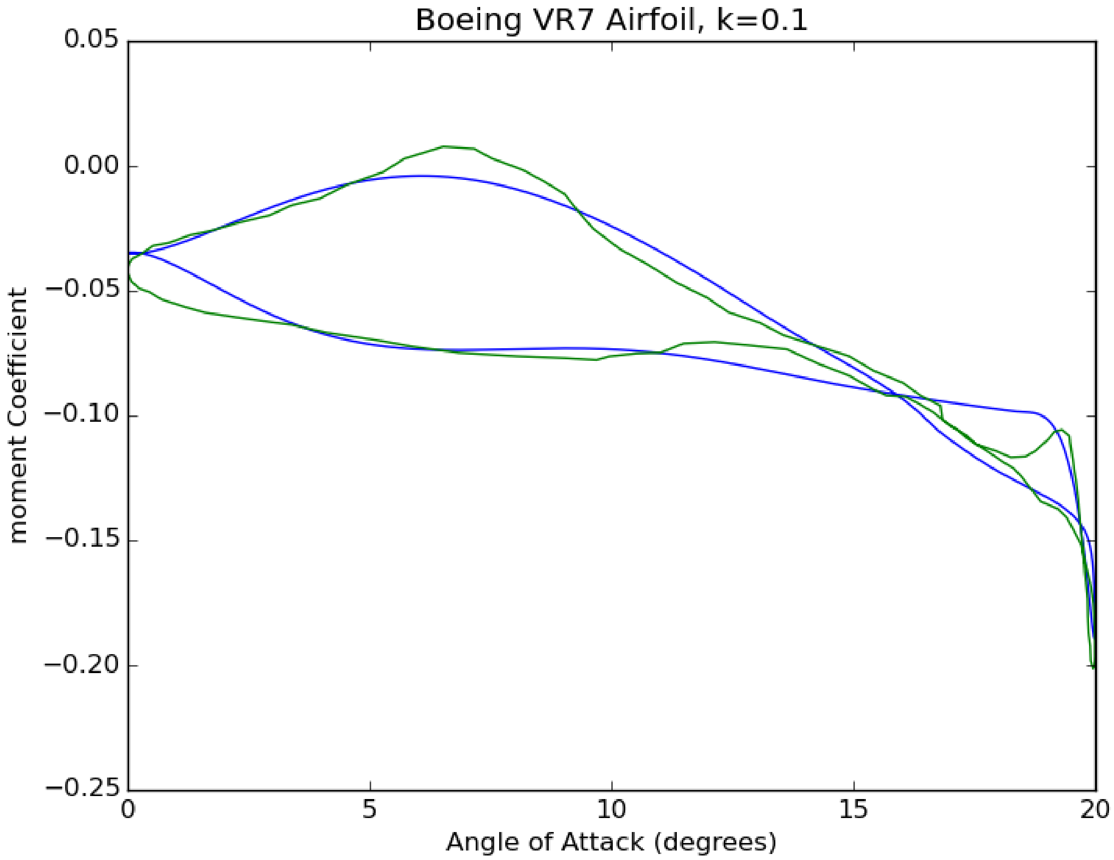

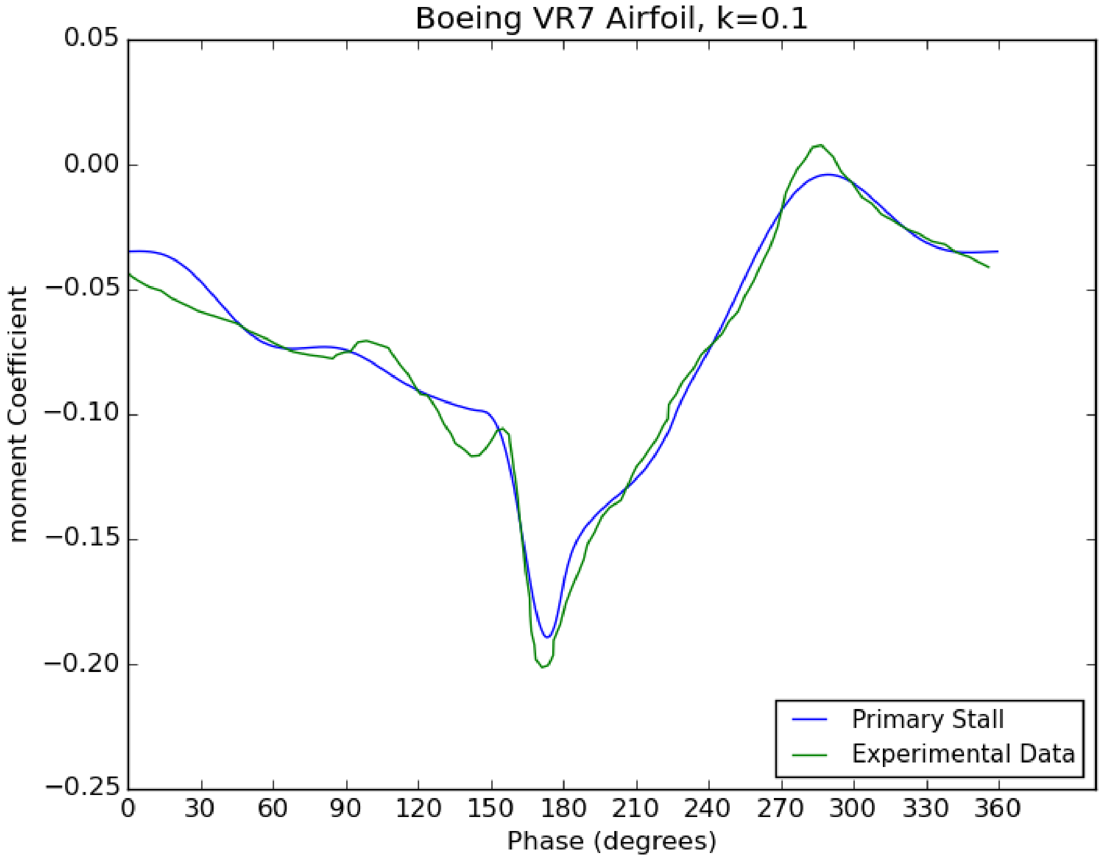

Figure 4.10 - Pitching moment solutions for k=0.1, compared to Ref [17]

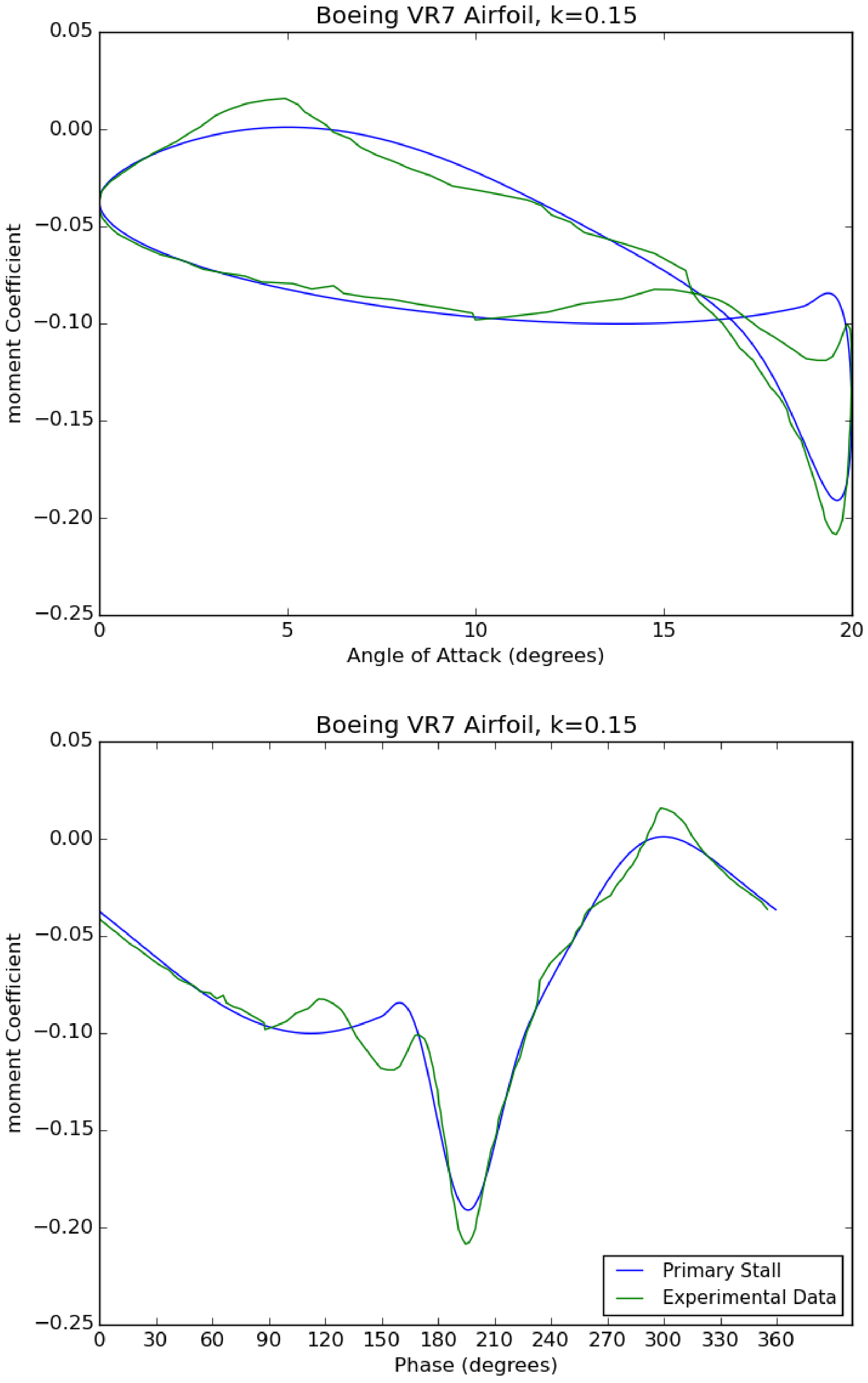

Figure 4.11 - Pitching moment solutions for k=0.15, compared to Ref [17]

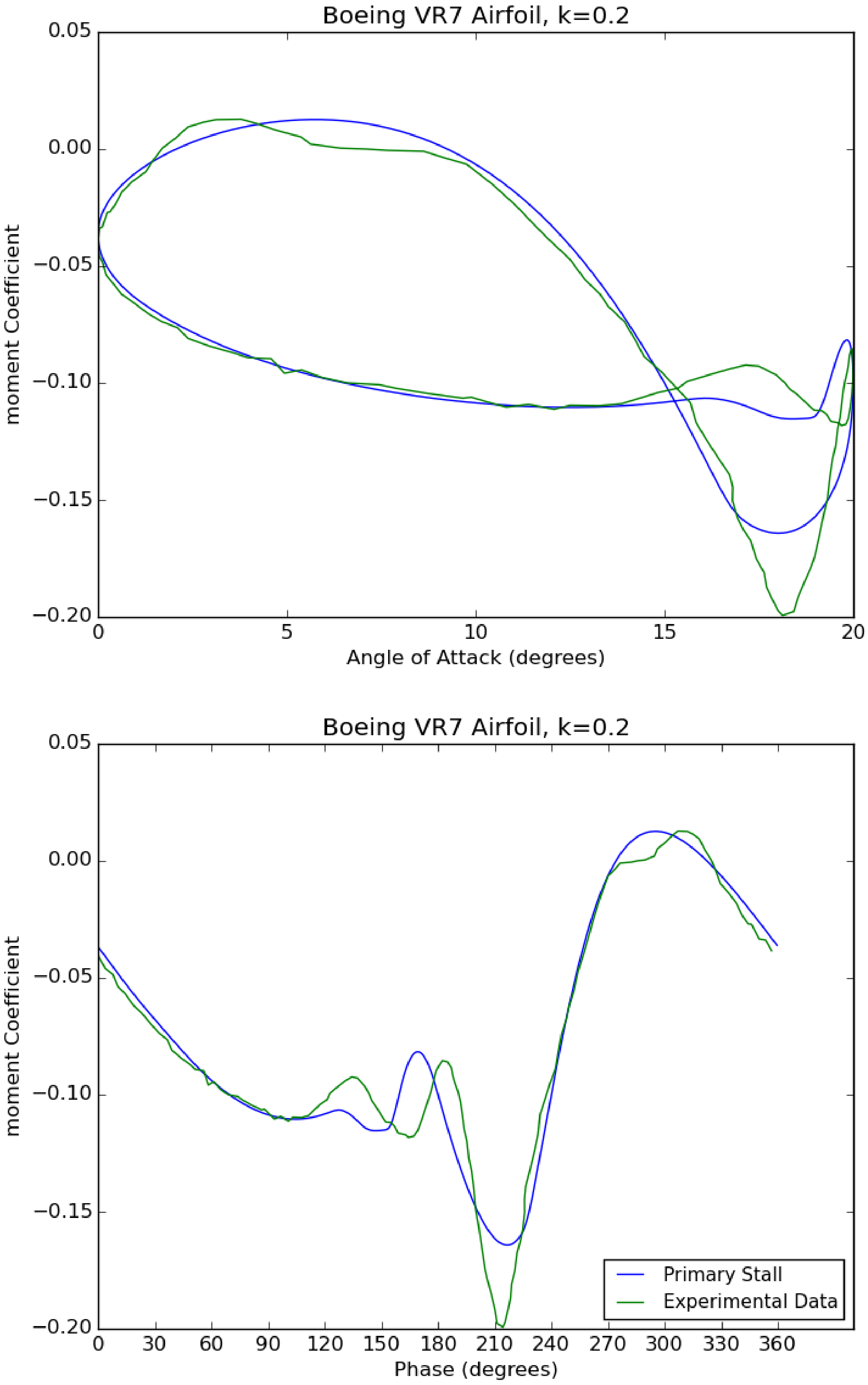

Figure 4.12 - Pitching moment solutions for k=0.2, compared to Ref [17]

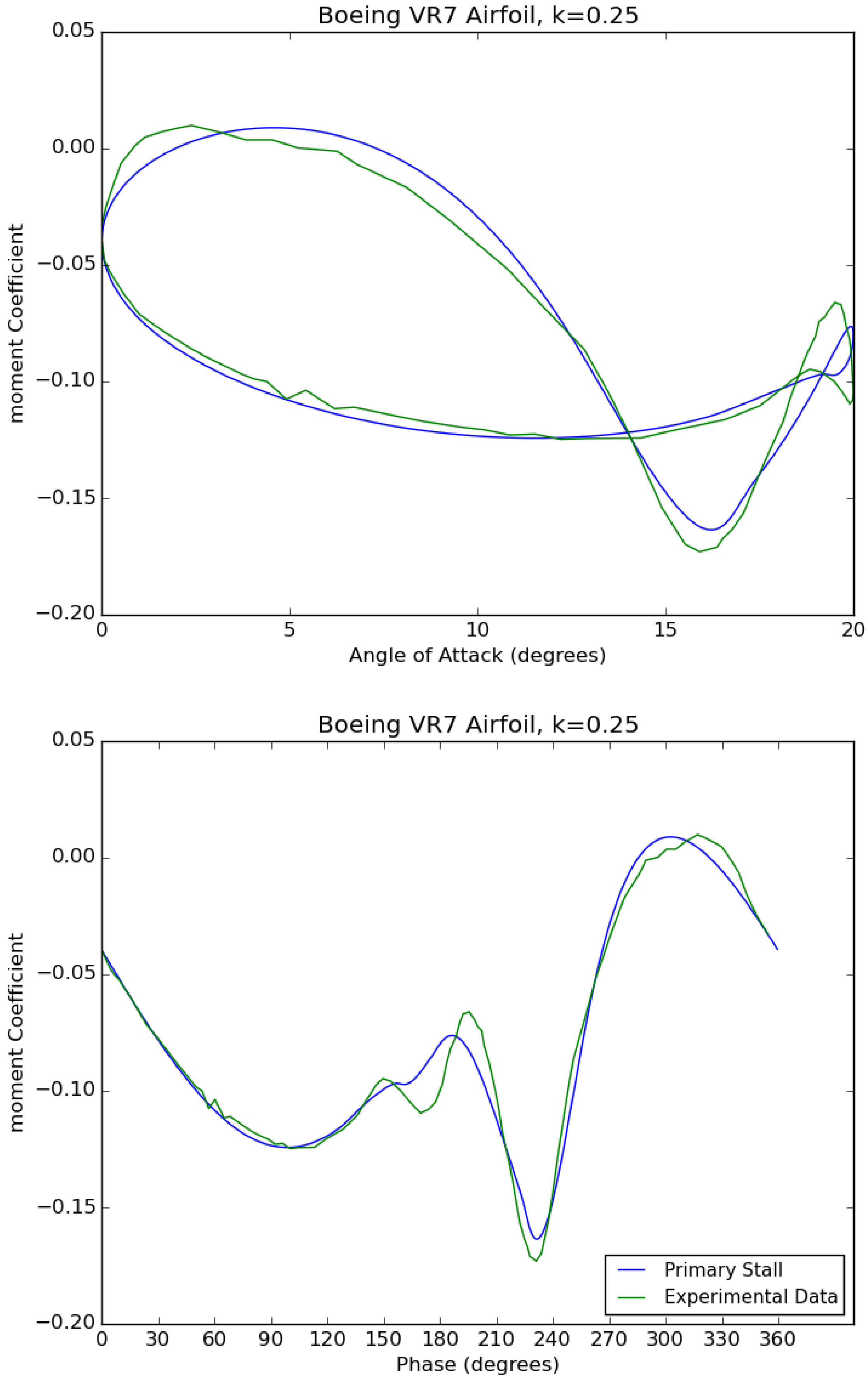

Figure 4.13 - Pitching moment solutions for k=0.25, compared to Ref [17]

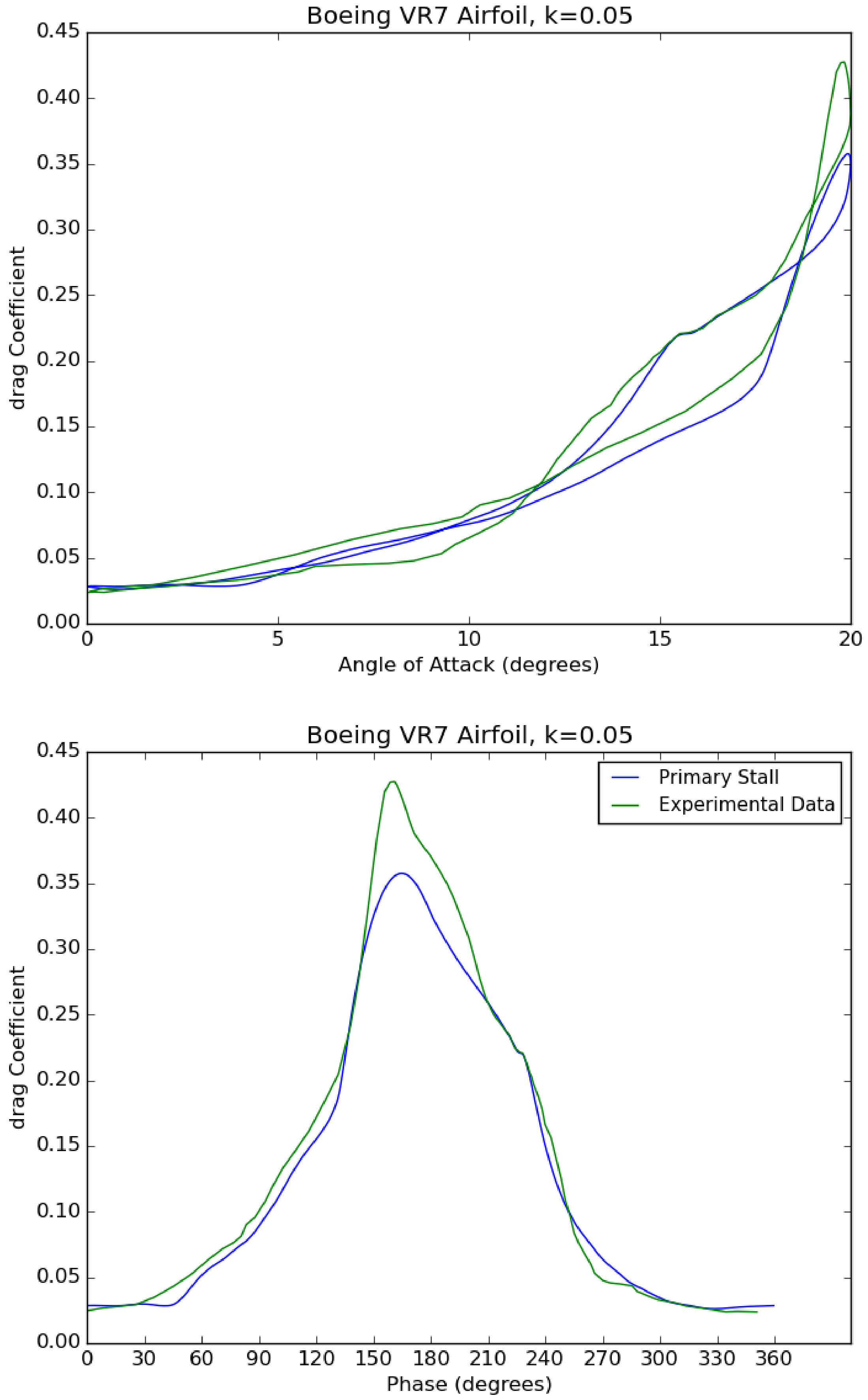

Figure 4.14 - Drag solutions for k=0.05, compared to Ref [17]

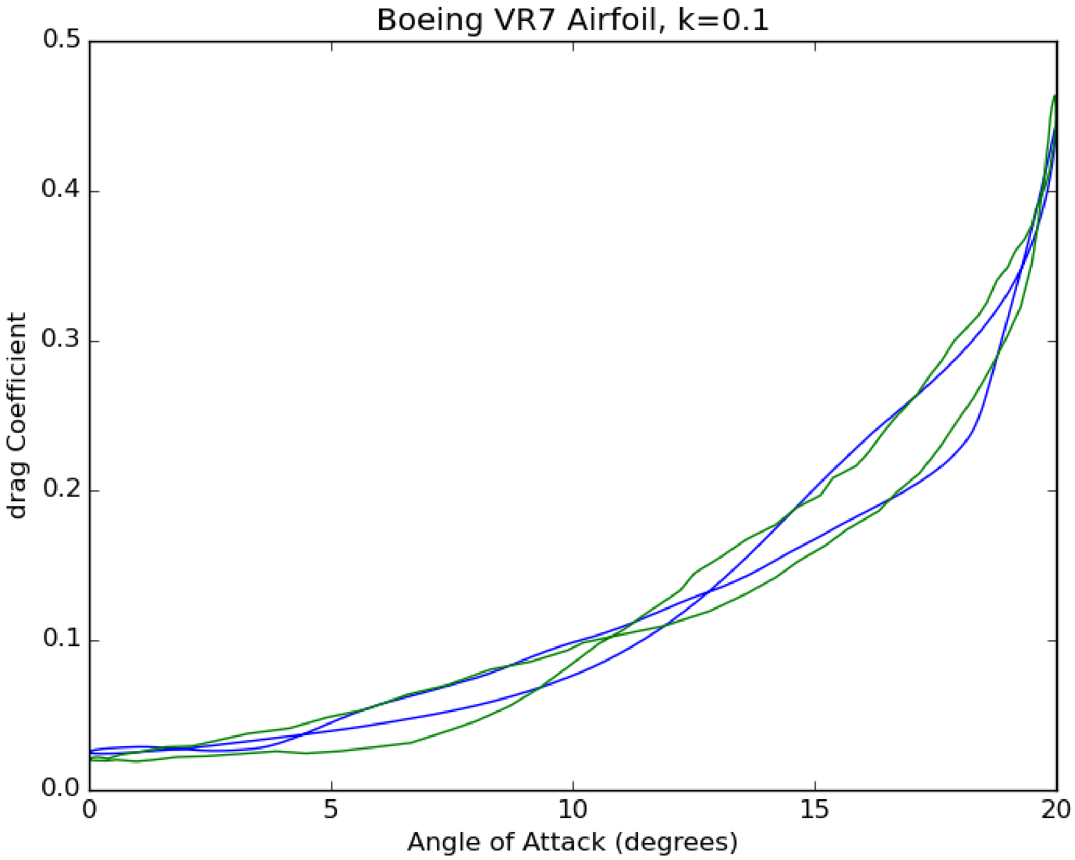

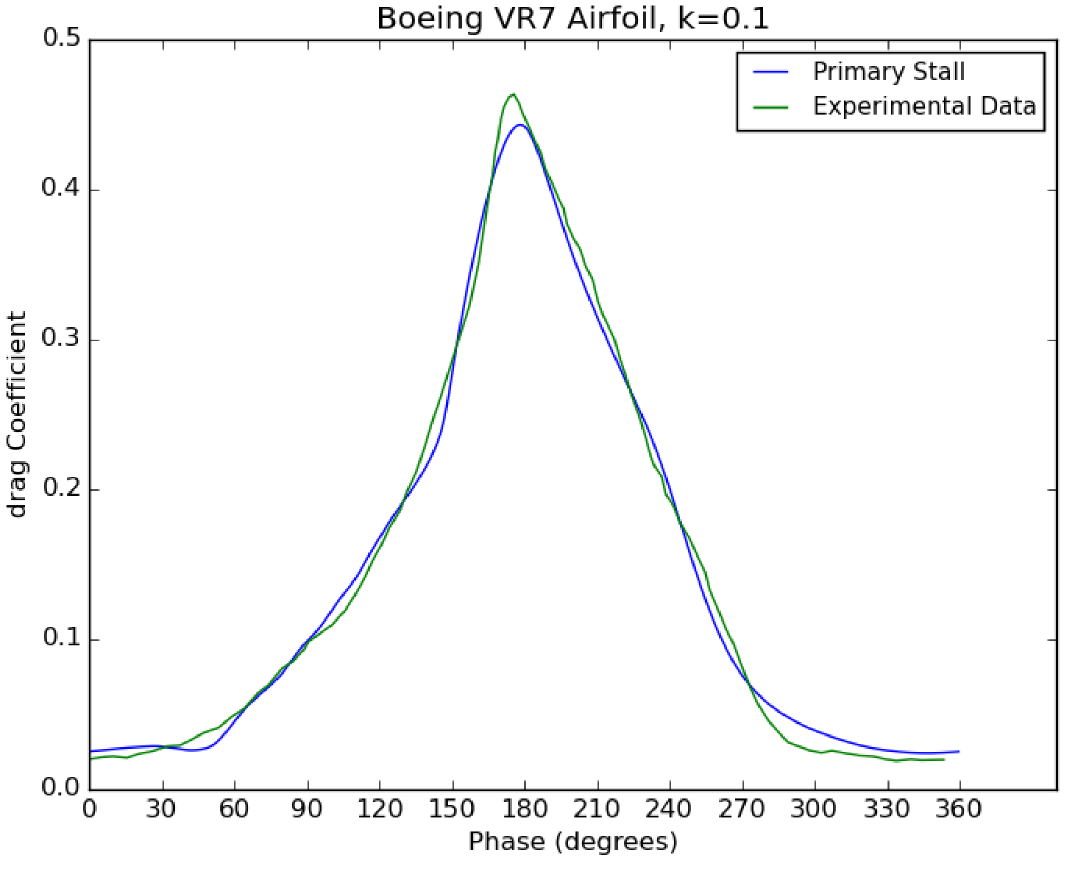

Figure 4.15 - Drag solutions for k=0.1, compared to Ref [17]

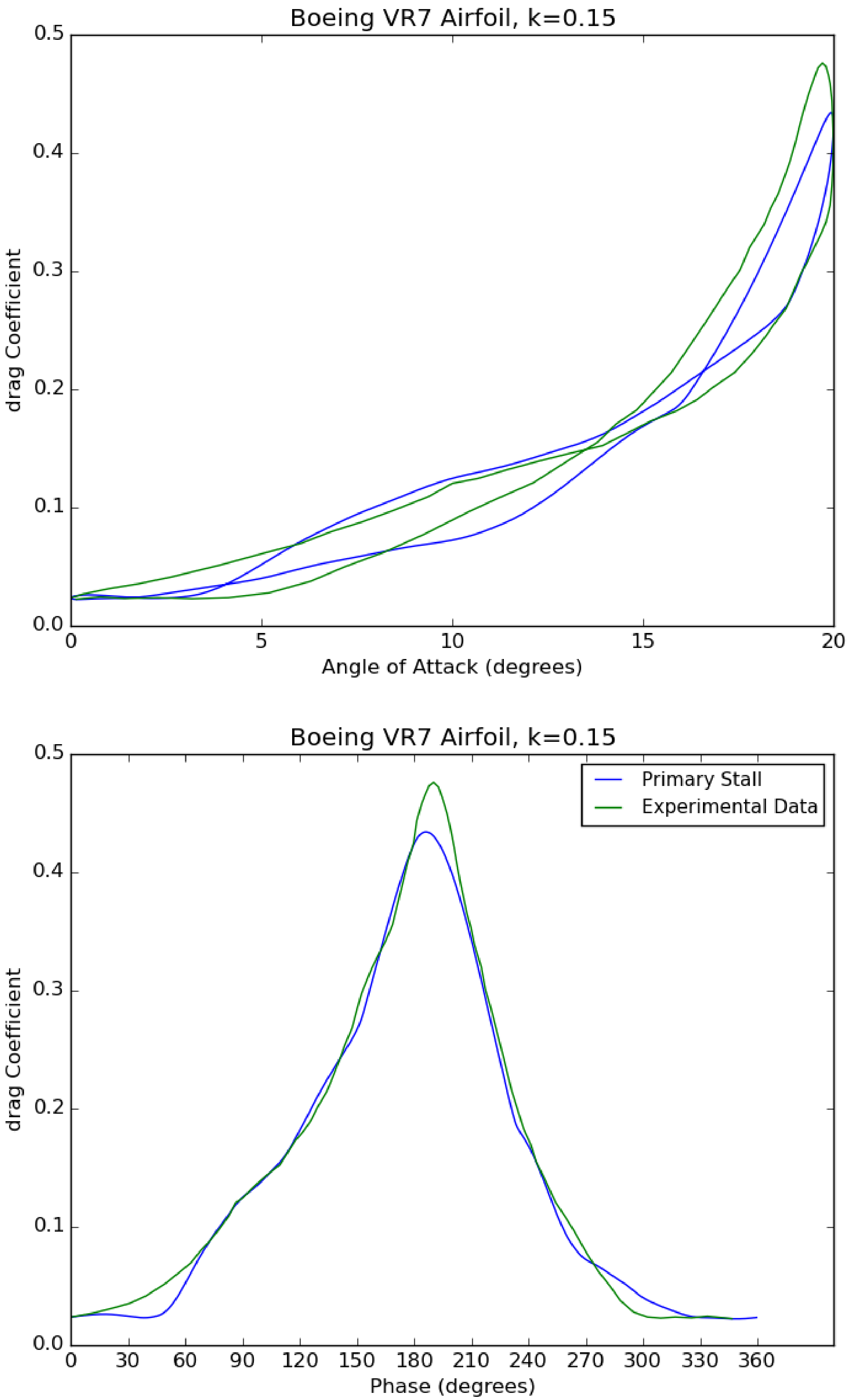

Figure 4.16 - Drag solutions for k=0.15, compared to Ref [17]

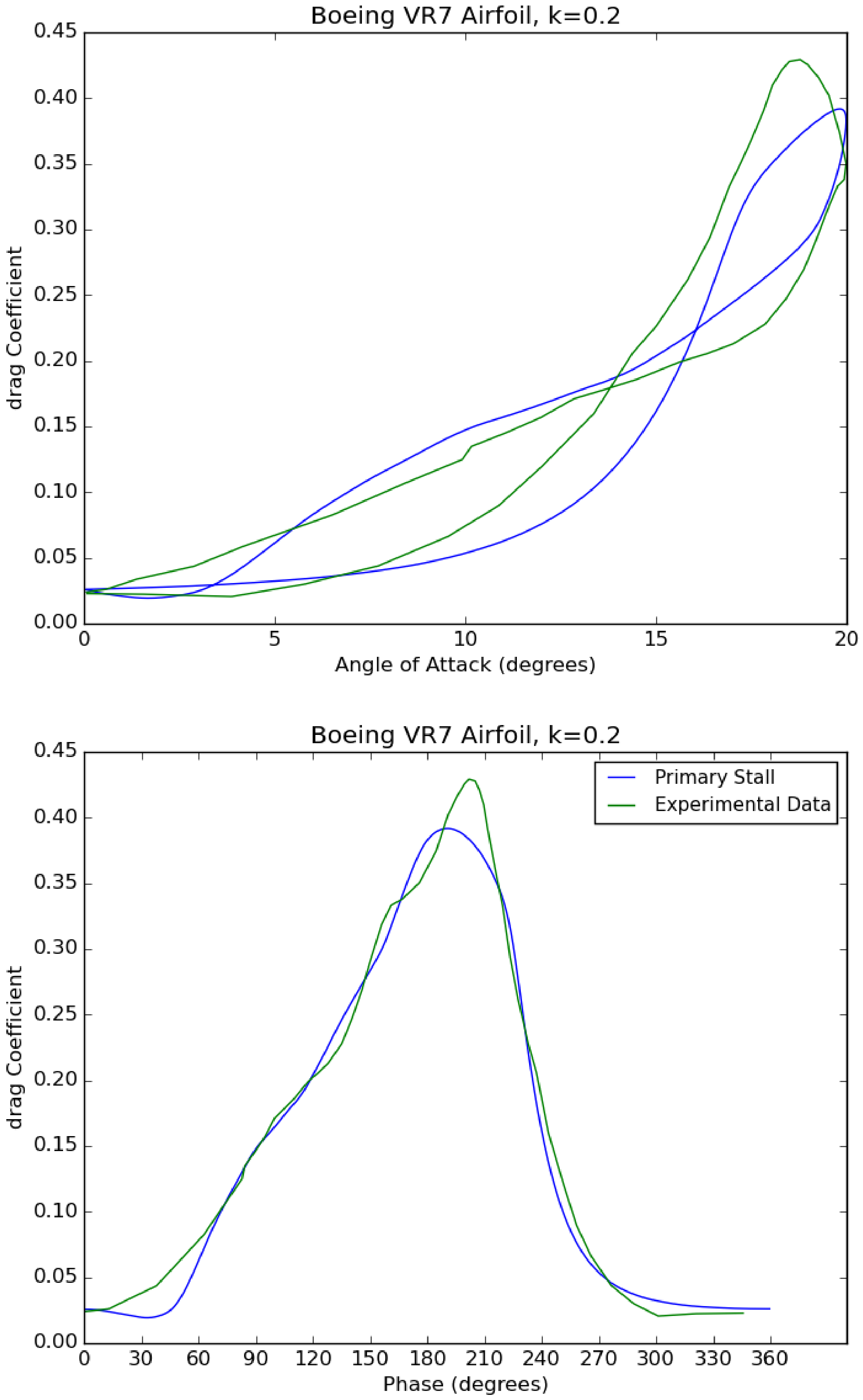

Figure 4.17 - Drag solutions for k=0.2, compared to Ref [17]

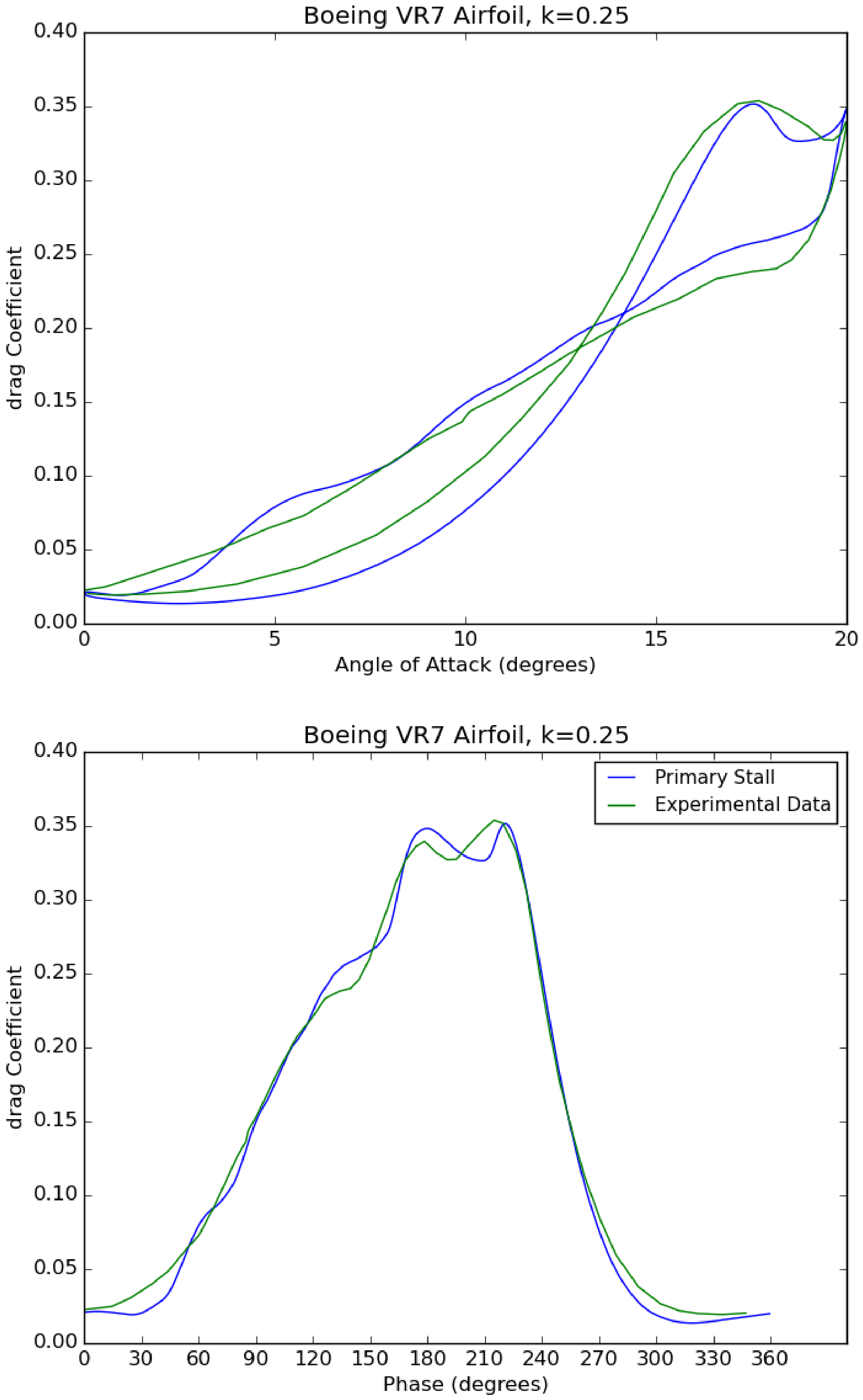

Figure 4.18 - Drag solutions for k=0.25, compared to Ref [17]

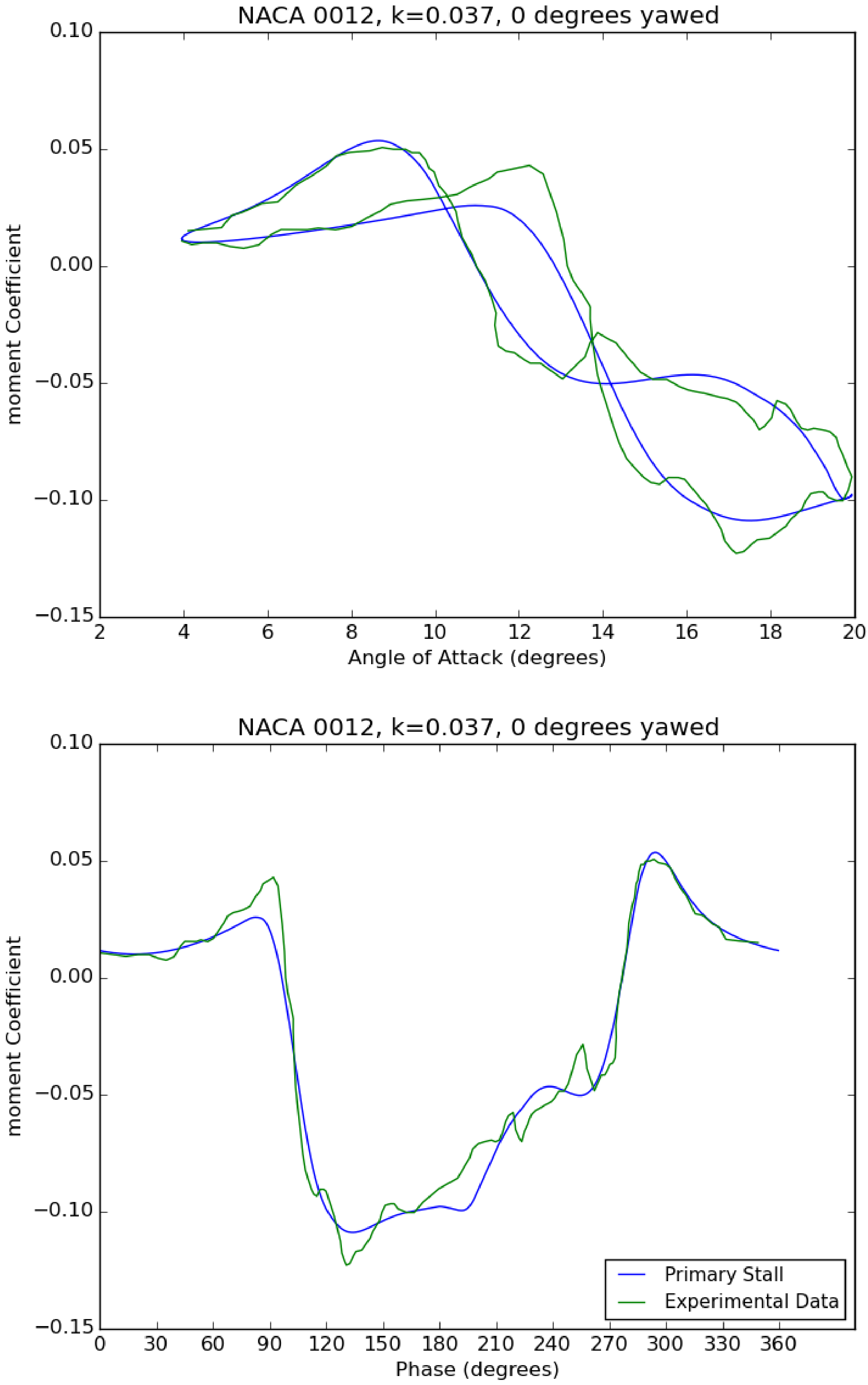

Figure 4.19 - Pitching moment solutions for k=0.037, M=0.4, compared to Ref [18]

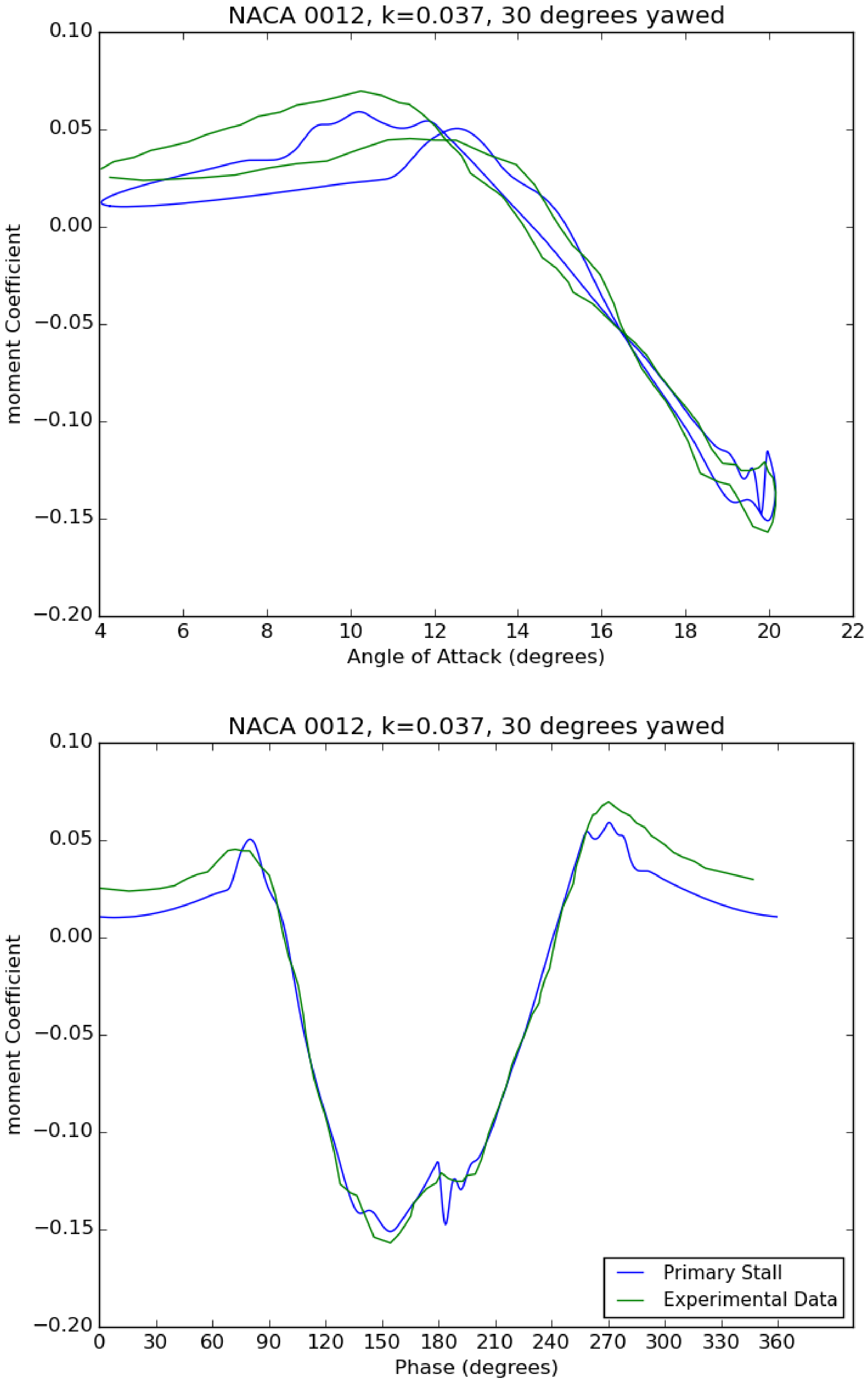

Figure 4.20 - Pitching moment solutions for k=0.037, M=0.4, compared to Ref [18]

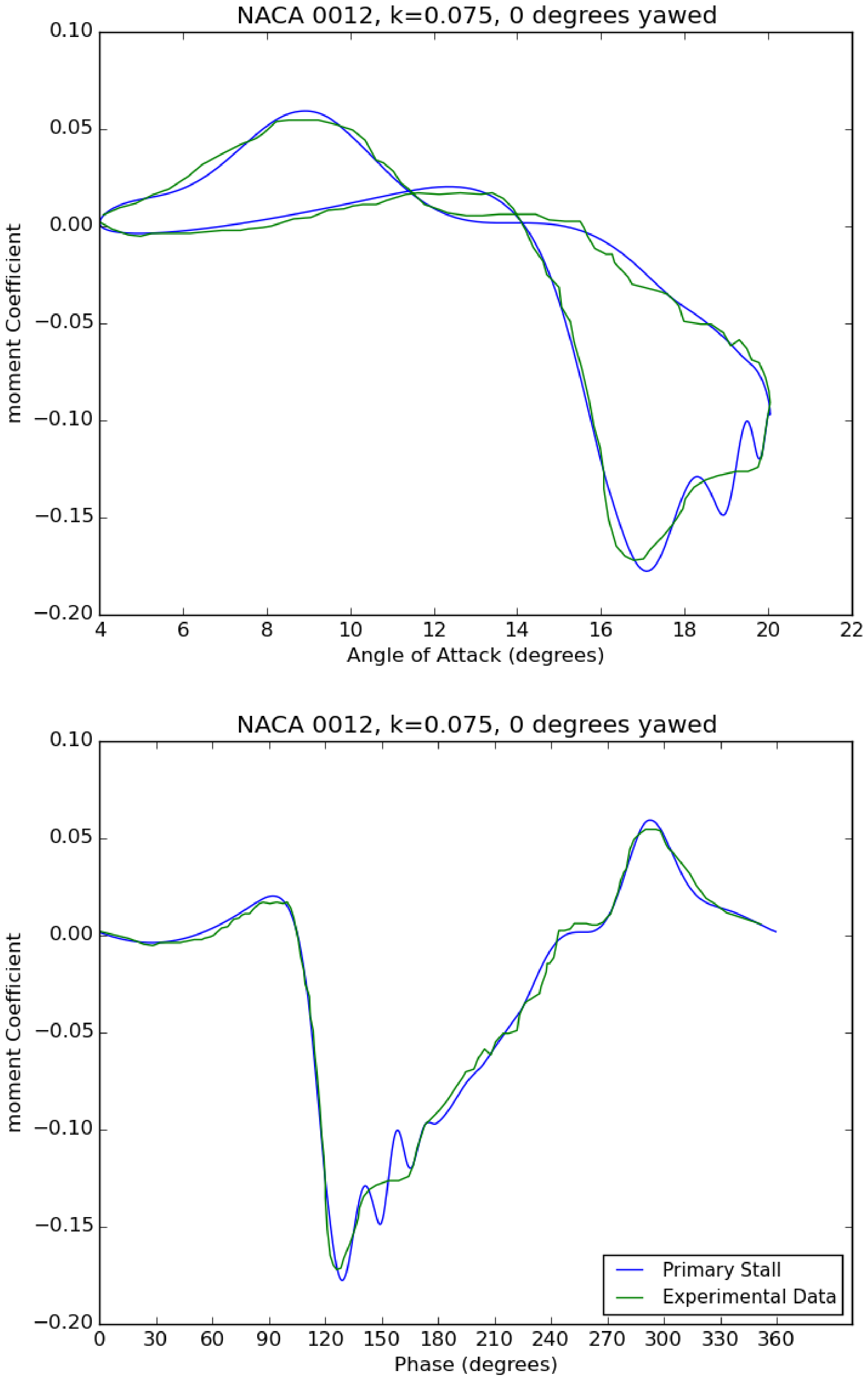

Figure 4.21 - Pitching moment solutions for k=0.075, M=0.4, compared to Ref [18]

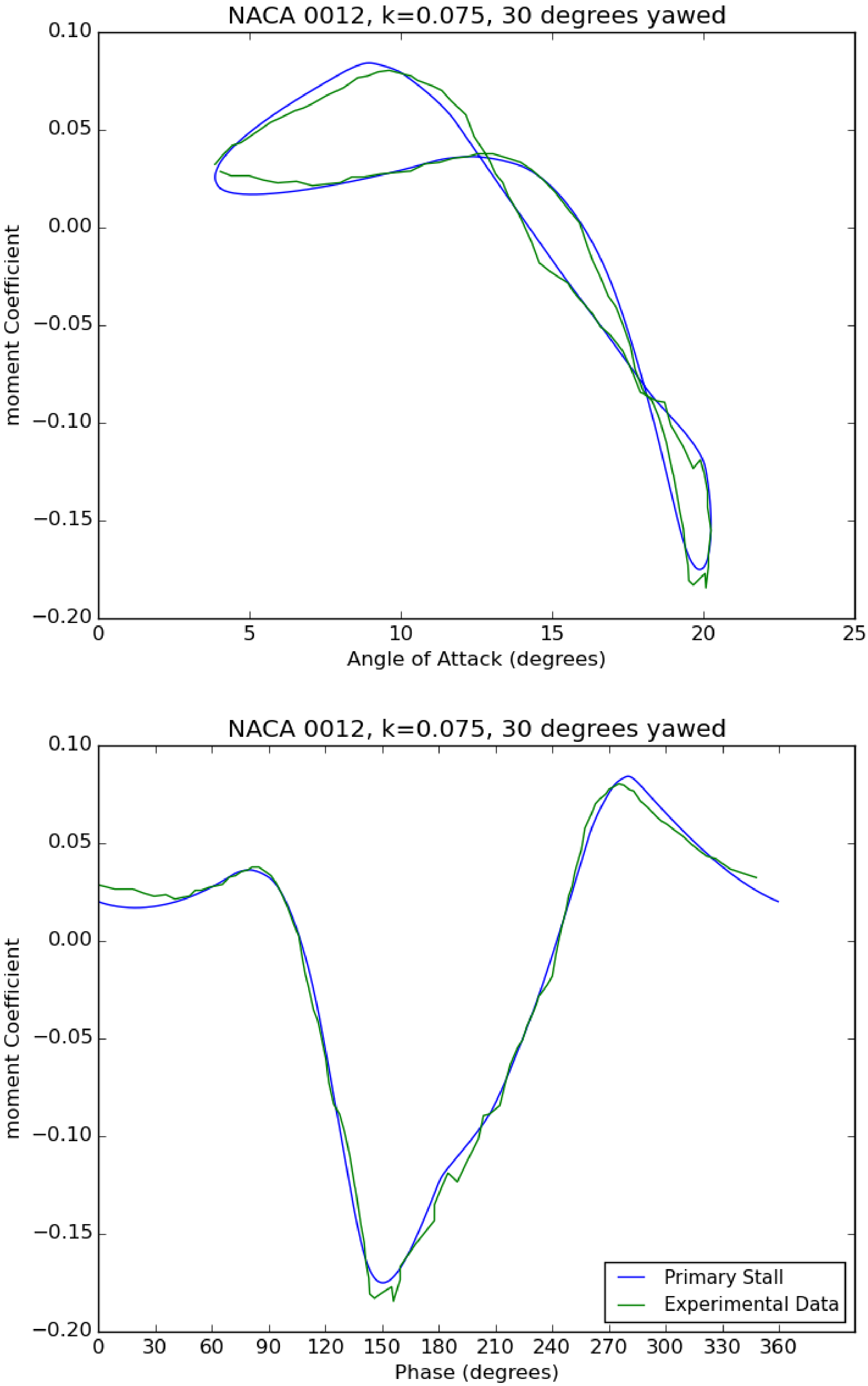

Figure 4.22 - Pitching moment solutions for k=0.075, M=0.4, compared to Ref [18]

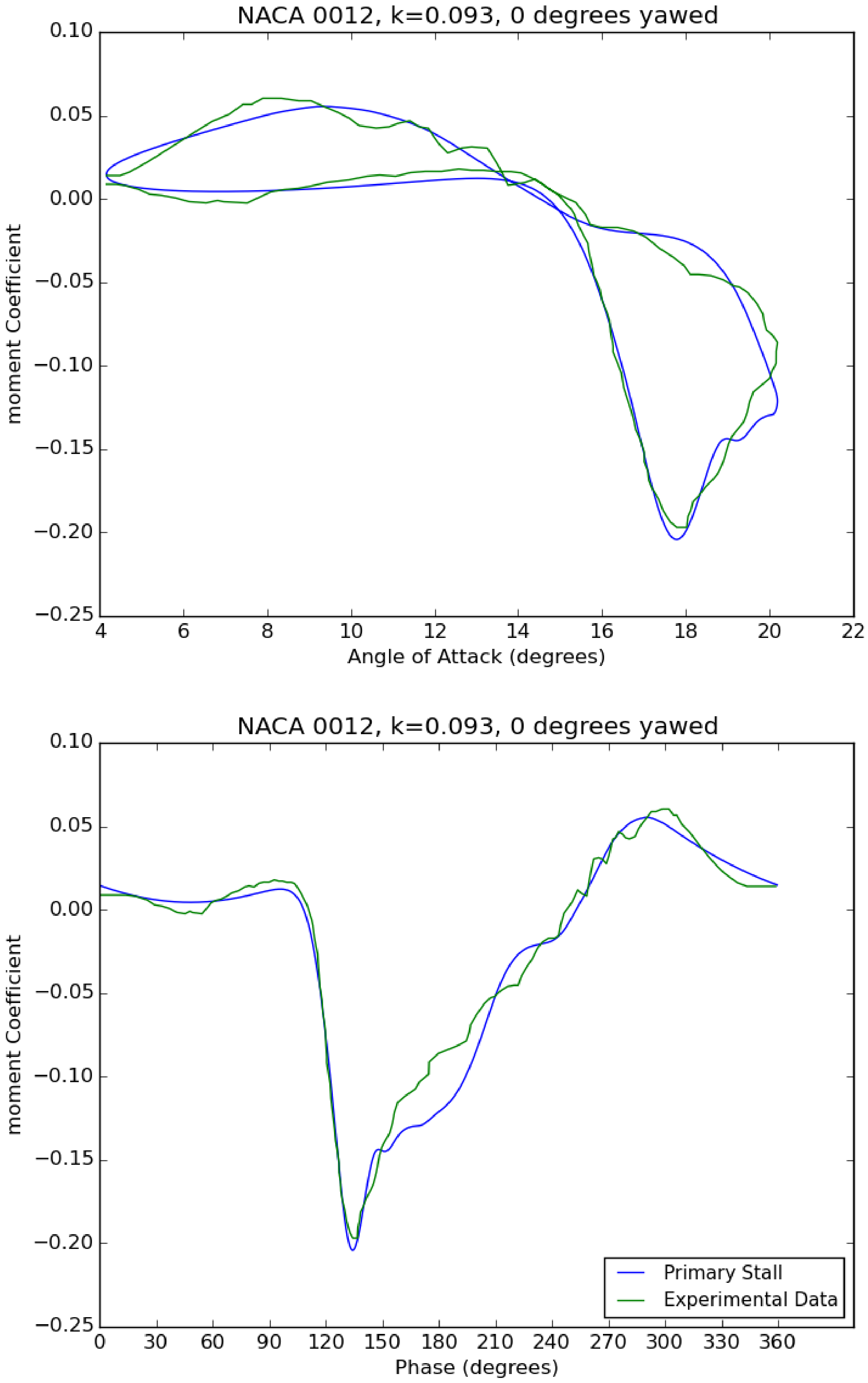

Figure 4.23 - Pitching moment solutions for k=0.093, M=0.4, compared to Ref [18]

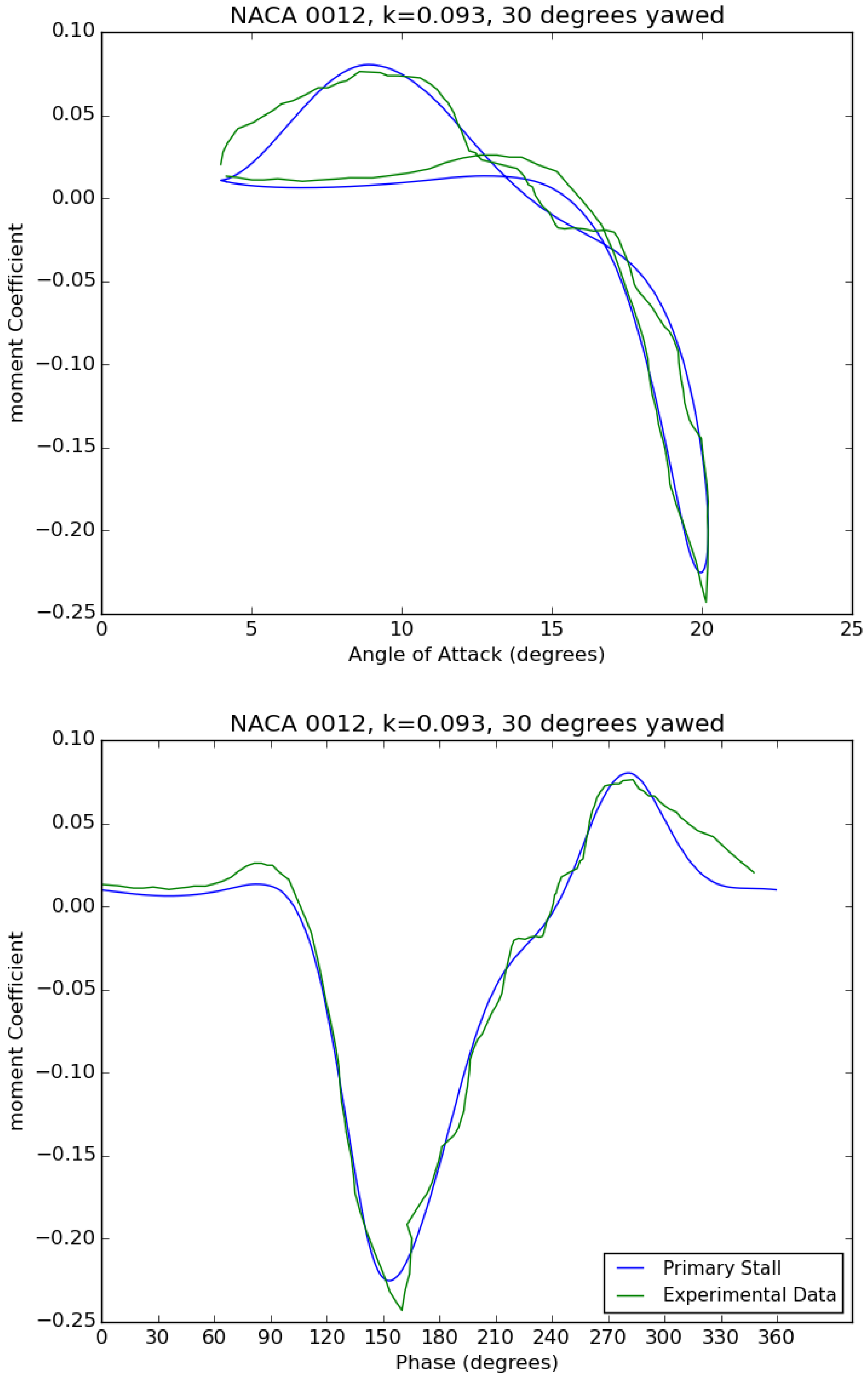

Figure 4.24 - Pitching moment solutions for k=0.093, M=0.4, compared to Ref [18]

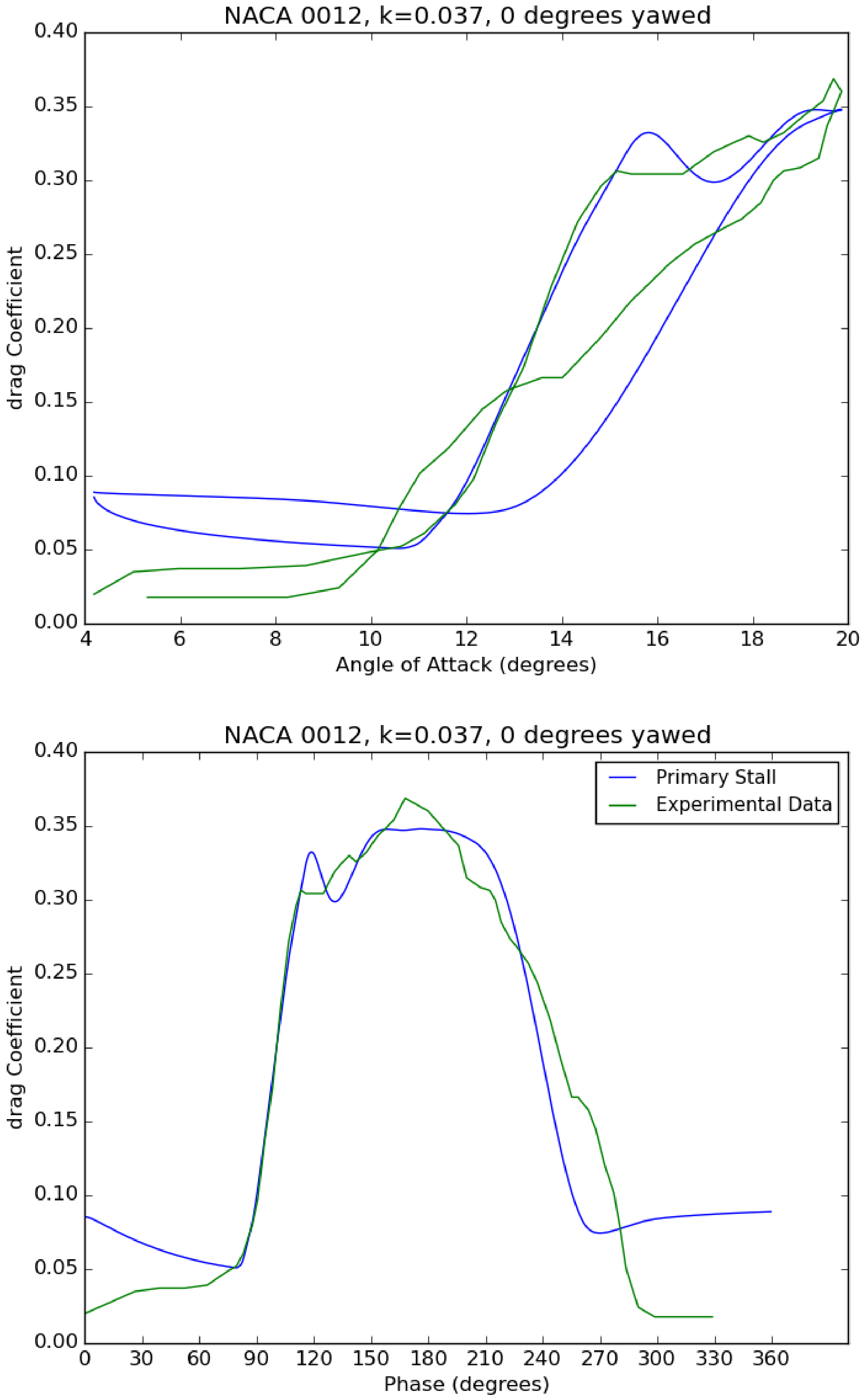

Figure 4.25 - Drag solutions for k=0.037, M=0.4, compared to Ref [18]

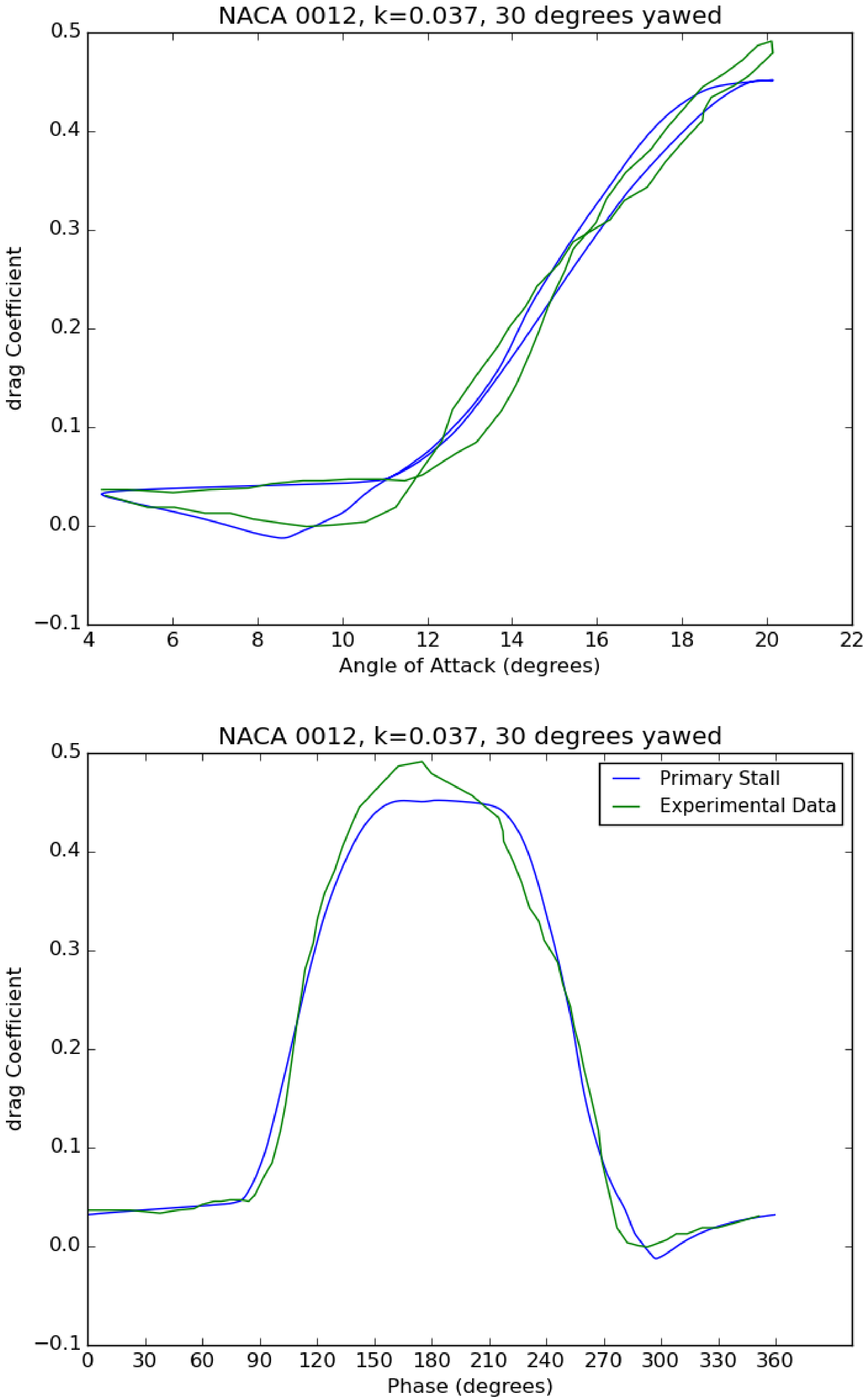

Figure 4.26 - Drag solutions for k=0.037, M=0.4, compared to Ref [18]

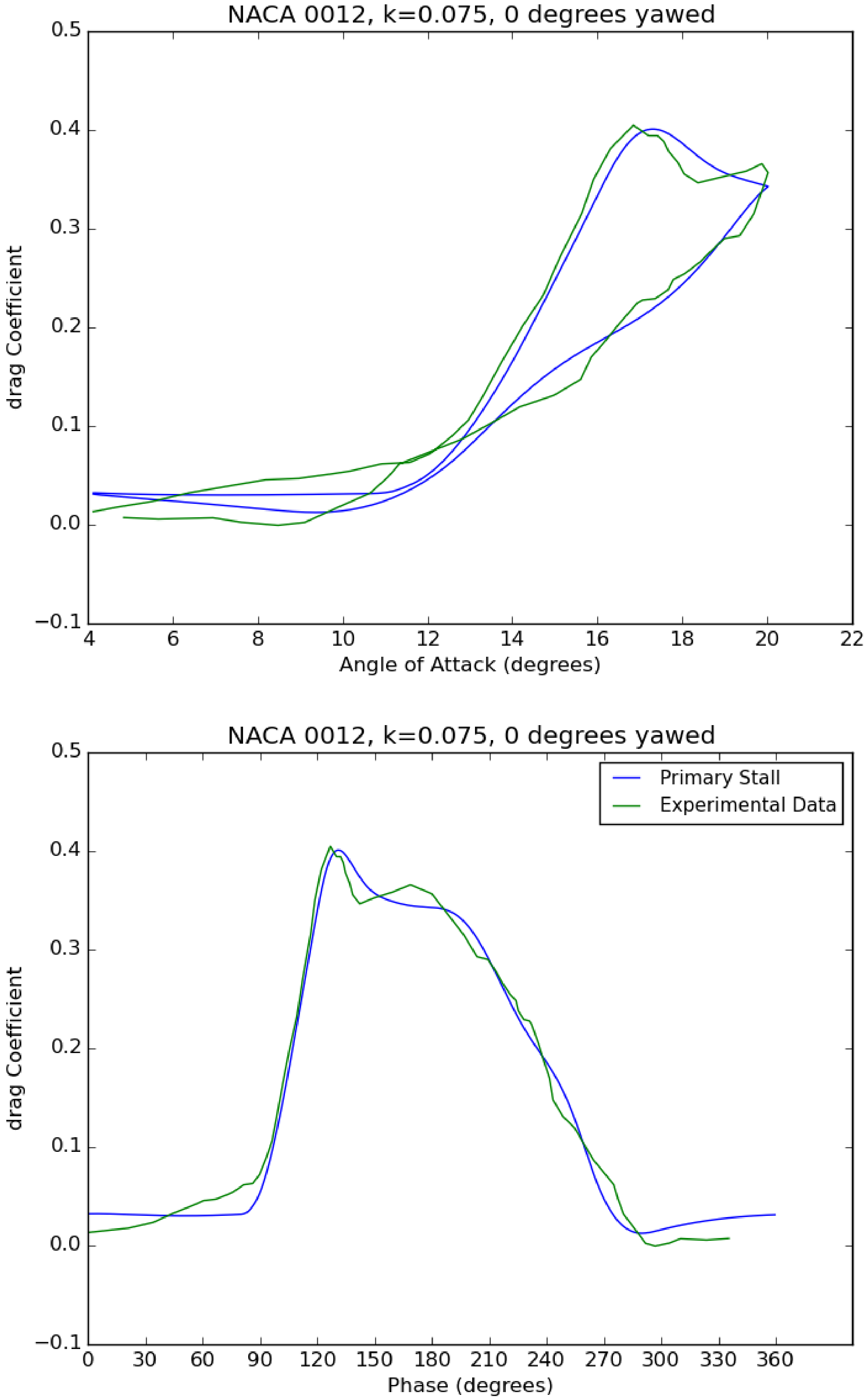

Figure 4.27 - Drag solutions for k=0.075, M=0.4, compared to Ref [18]

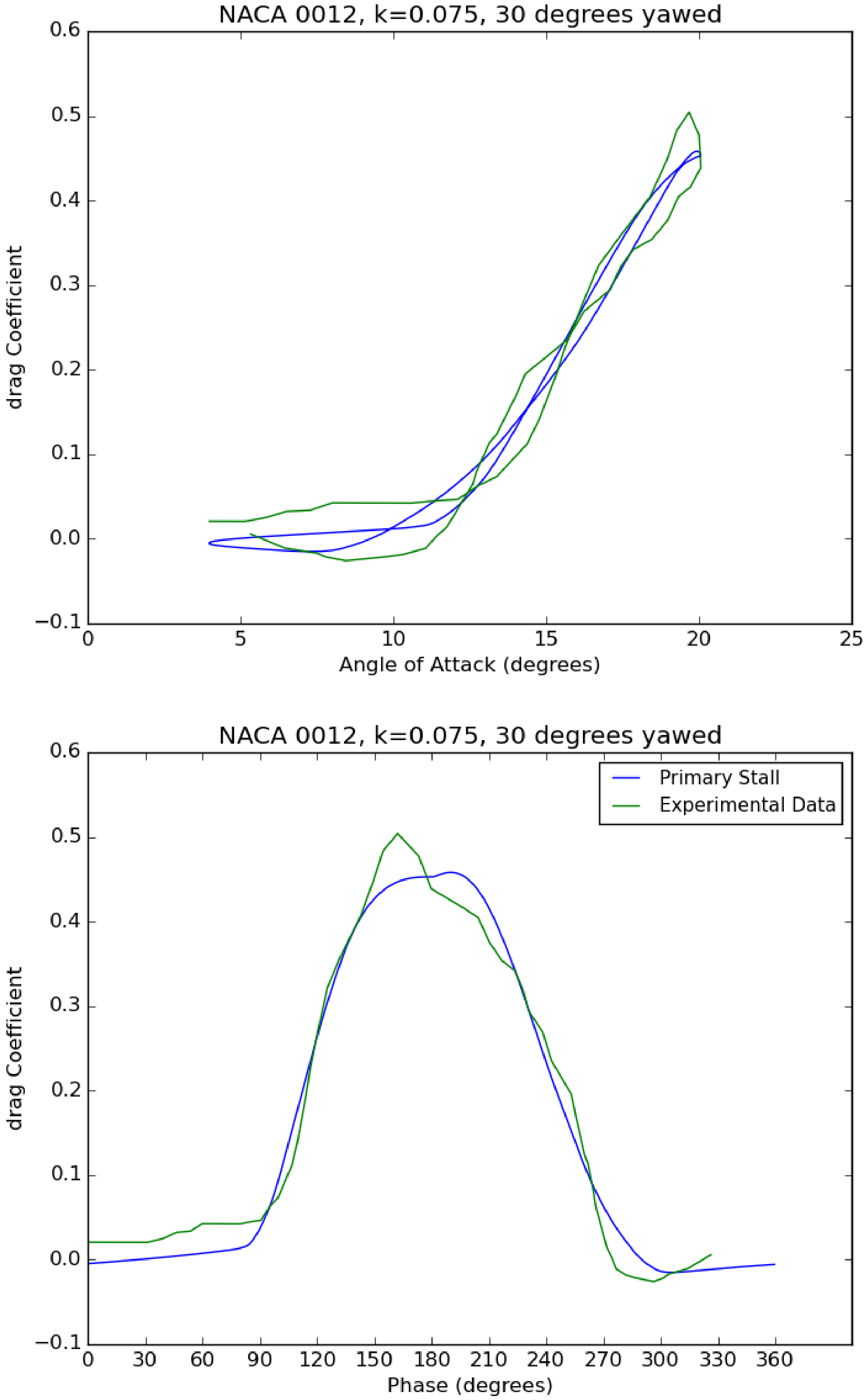

Figure 4.28 - Drag solutions for k=0.075, M=0.4, compared to Ref [18]

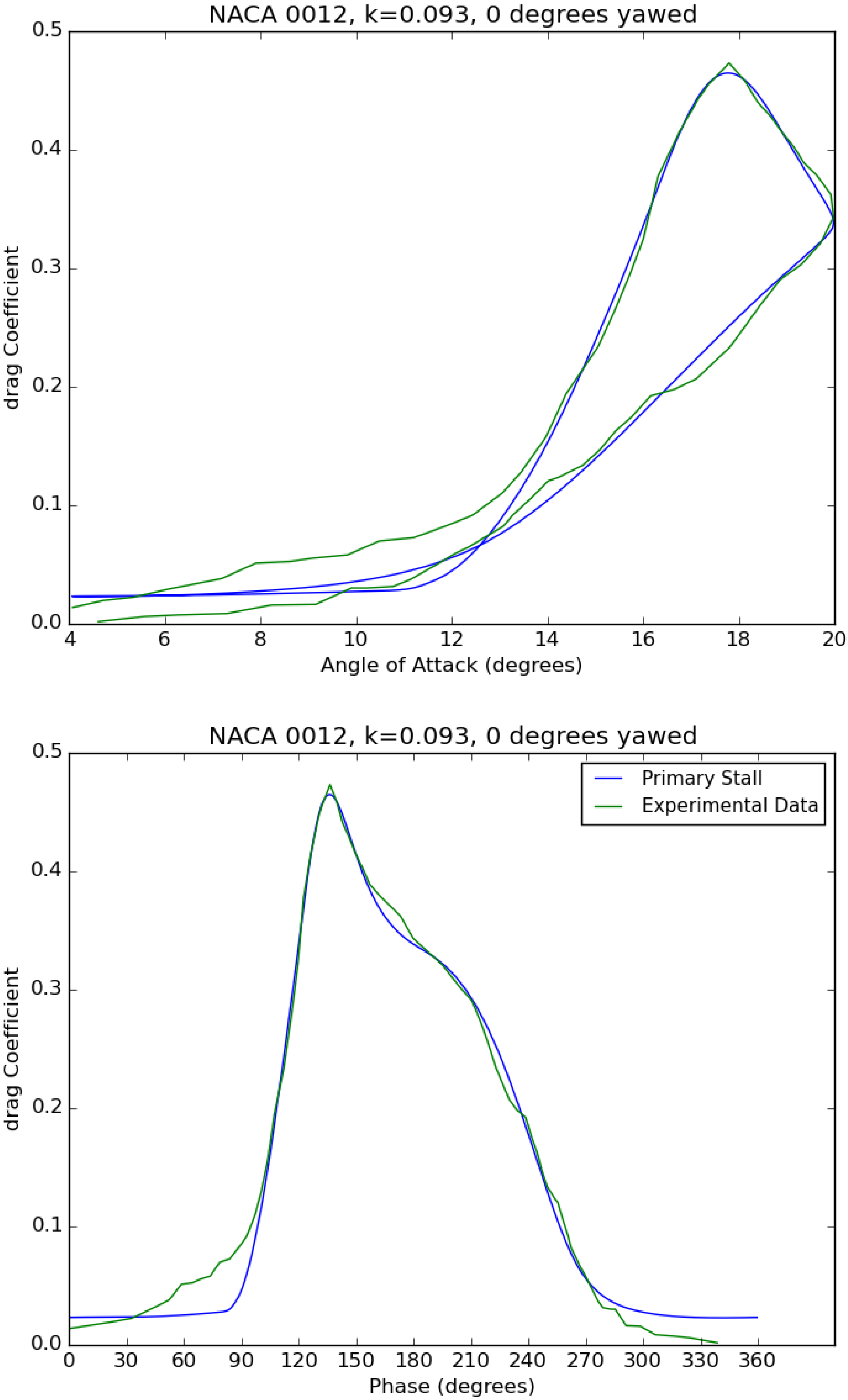

Figure 4.29 - Drag solutions for k=0.093, M=0.4, compared to Ref [18]

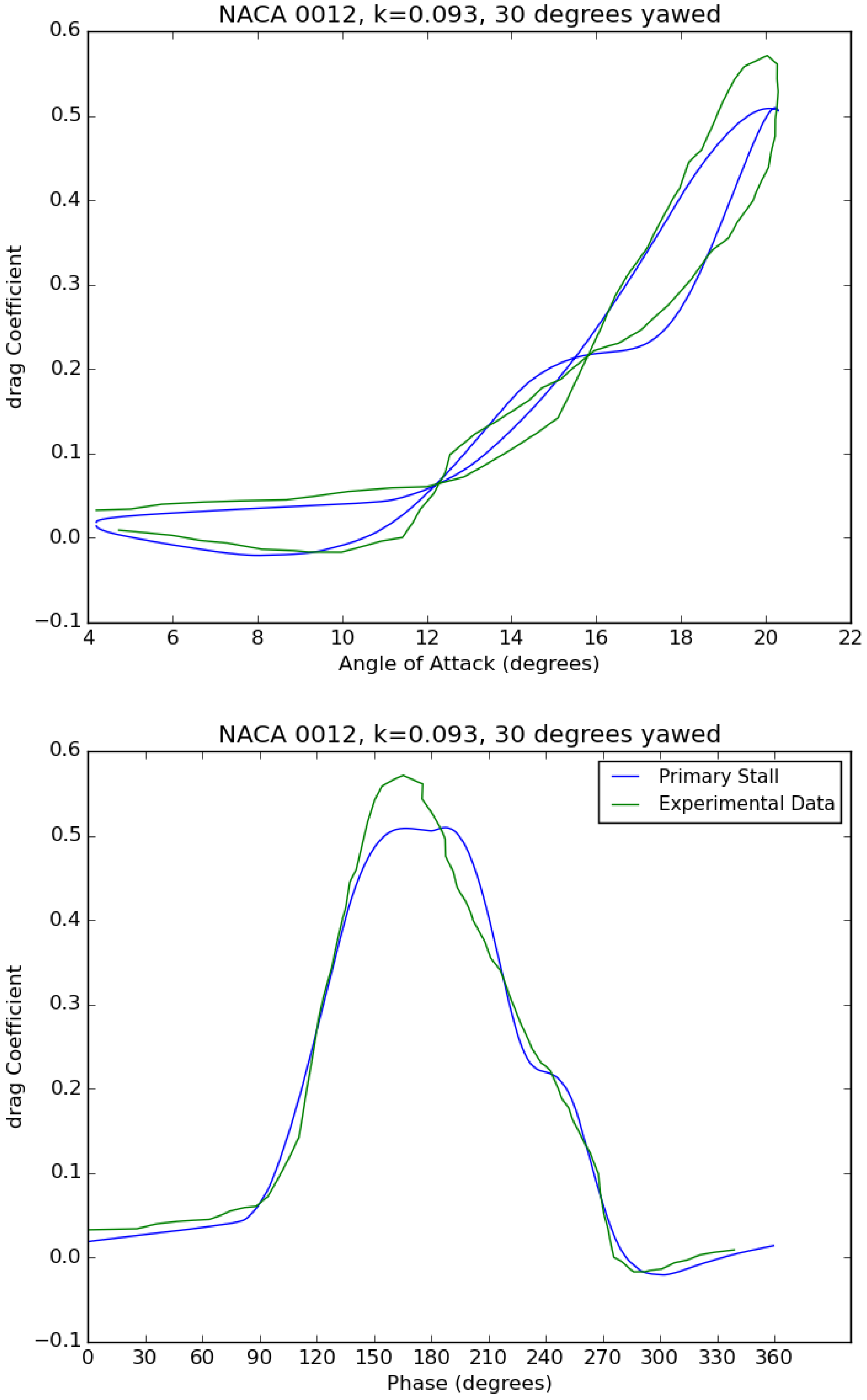

Figure 4.30 - Drag solutions for k=0.093, M=0.4, compared to Ref [18]

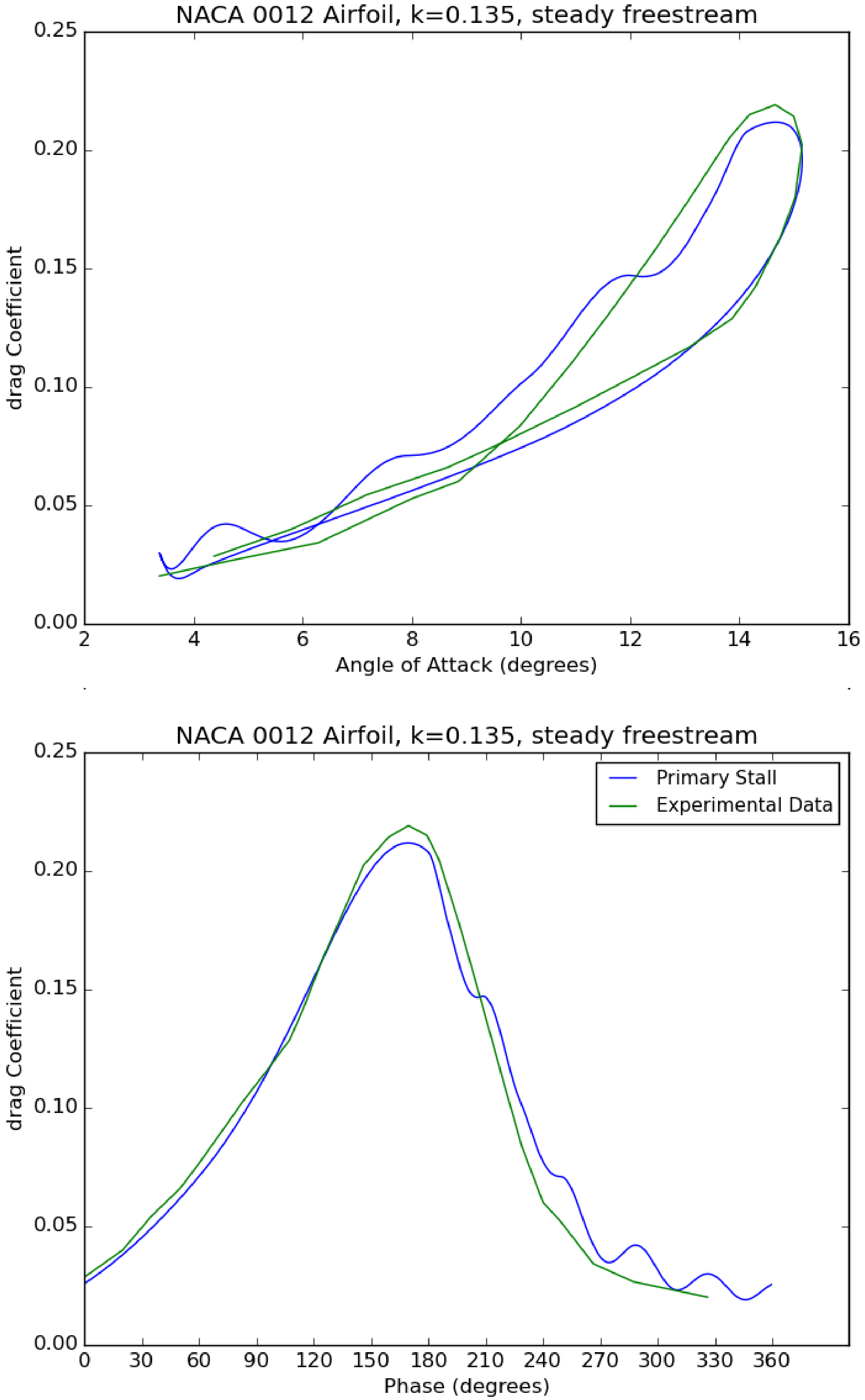

NACA 0012 Airfoil, k=0.135, steady freestream

NACA 0012 Airfoil, k=0.135, steady freestream

Figure 4.31 - Drag solutions for k=0.135, compared to Ref [21]

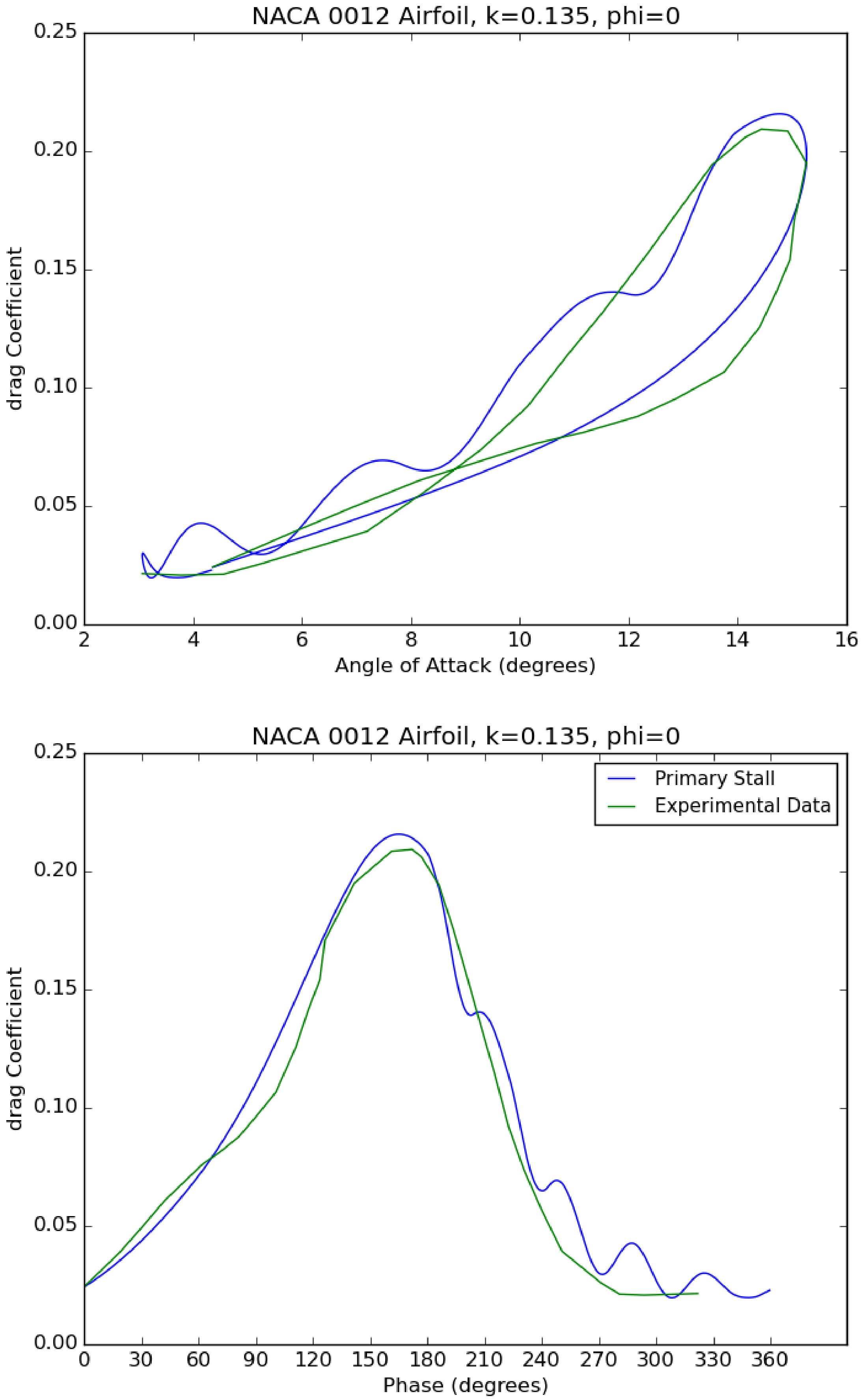

Figure 4.32 - Drag solutions for k=0.135, compared to Ref [21]

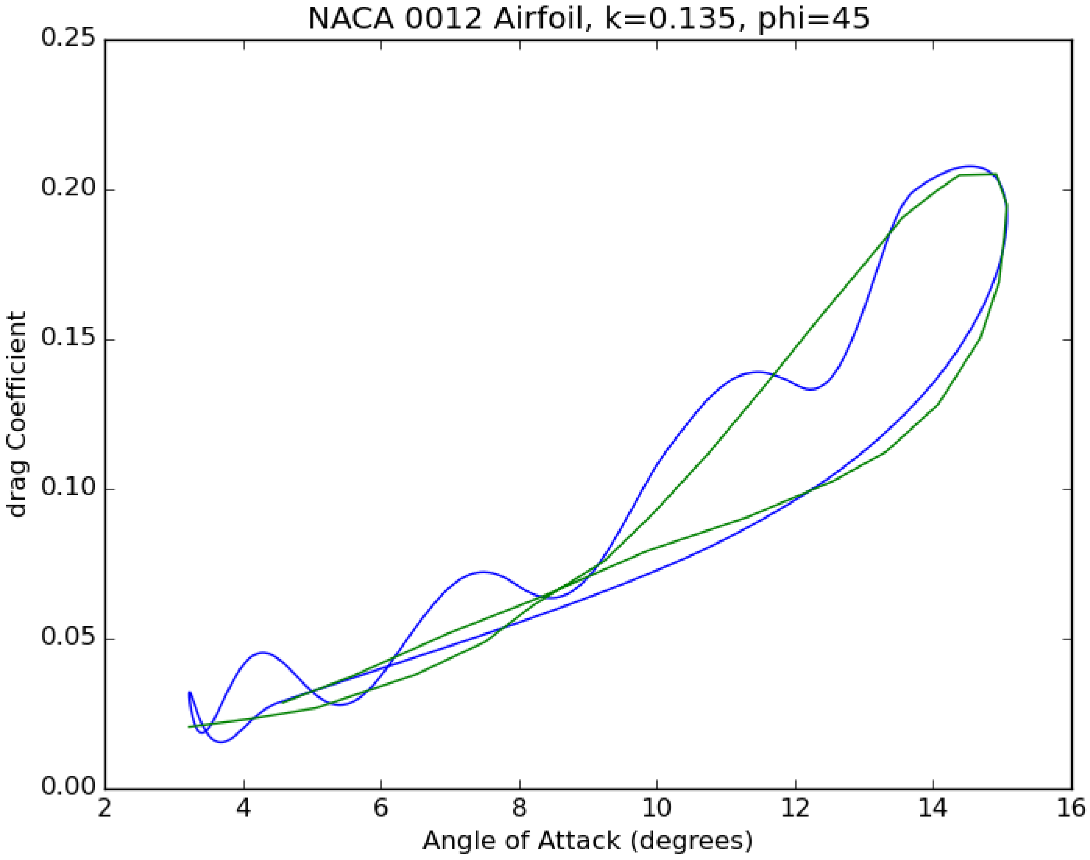

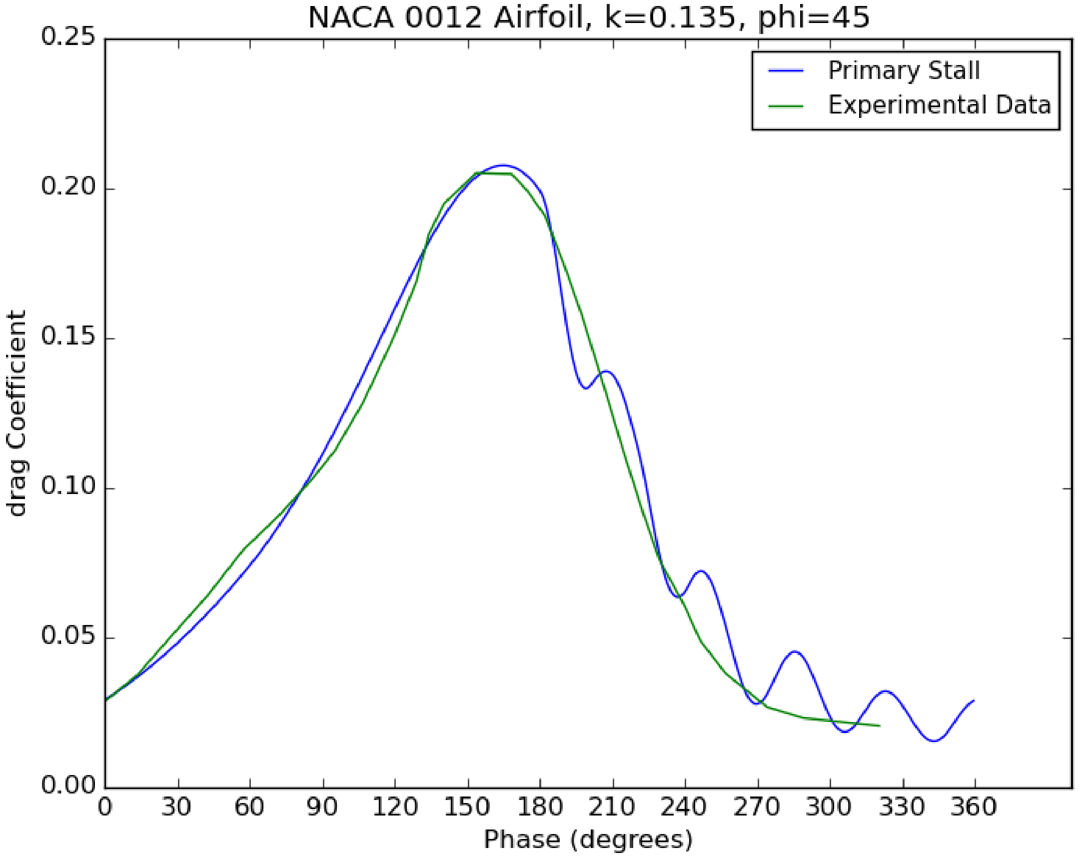

Figure 4.33 - Drag solutions for k=0.135, compared to Ref [21]

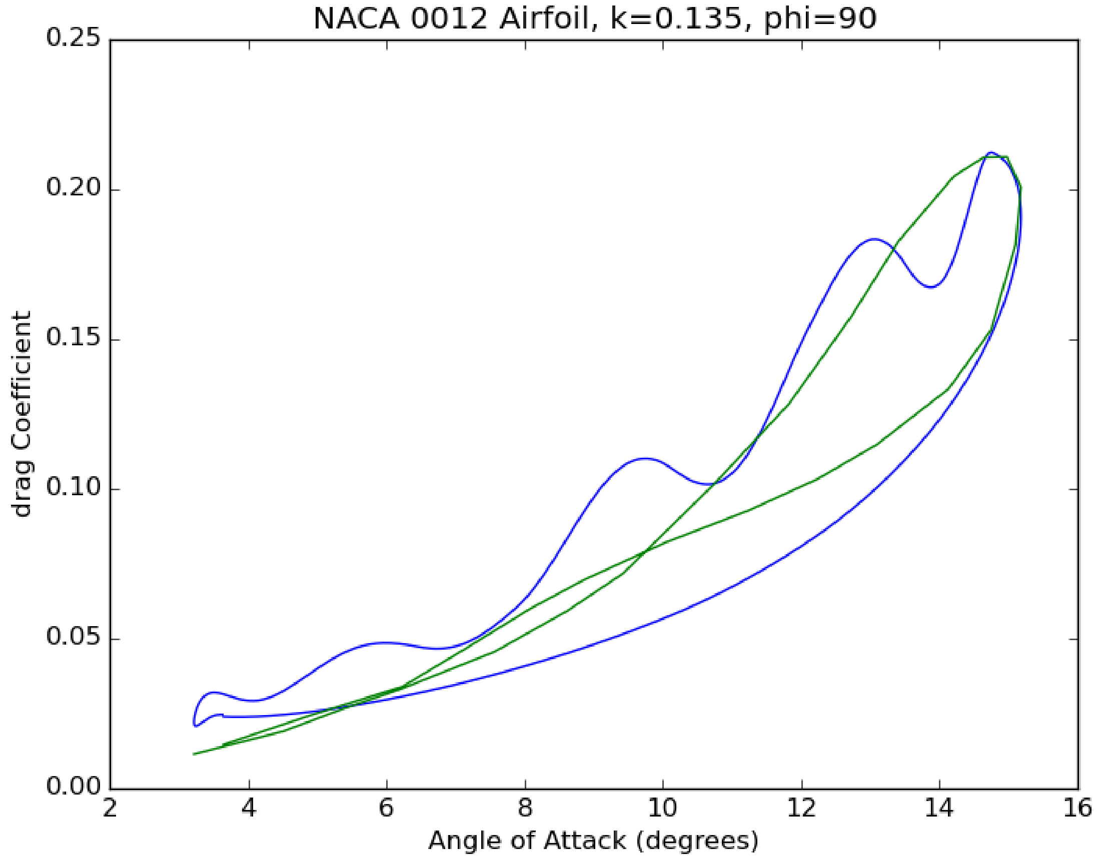

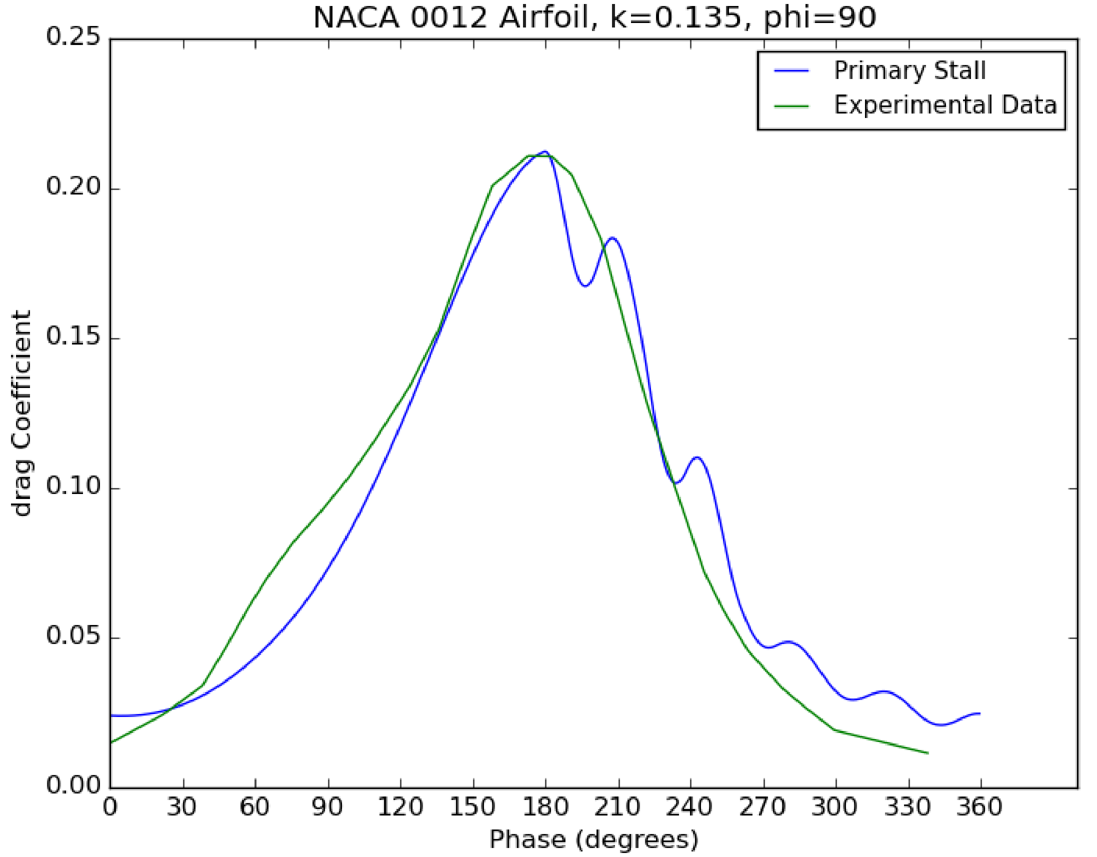

Figure 4.34 - Drag solutions for k=0.135, compared to Ref [21]

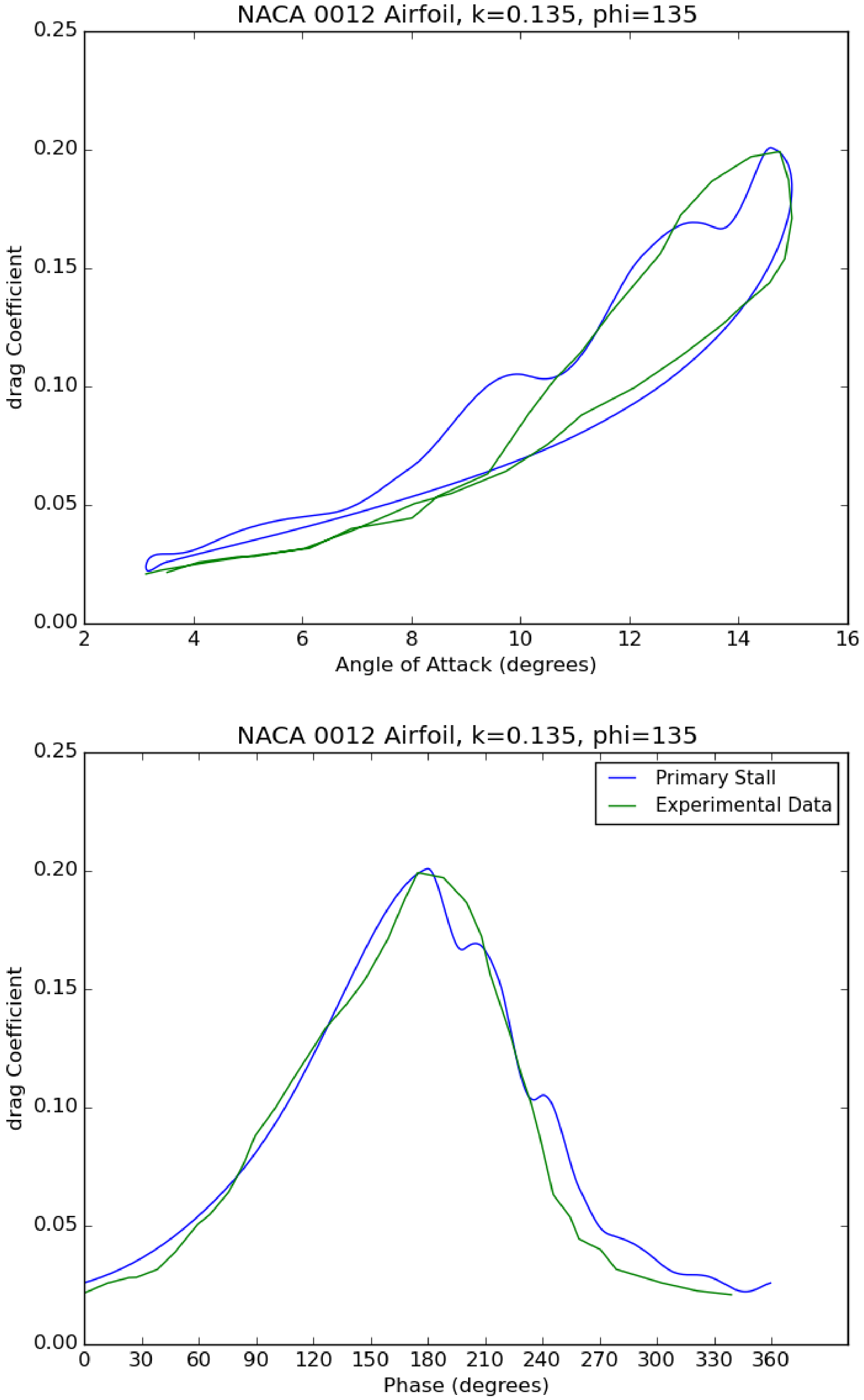

Figure 4.35 - Drag solutions for k=0.135, compared to Ref [21]

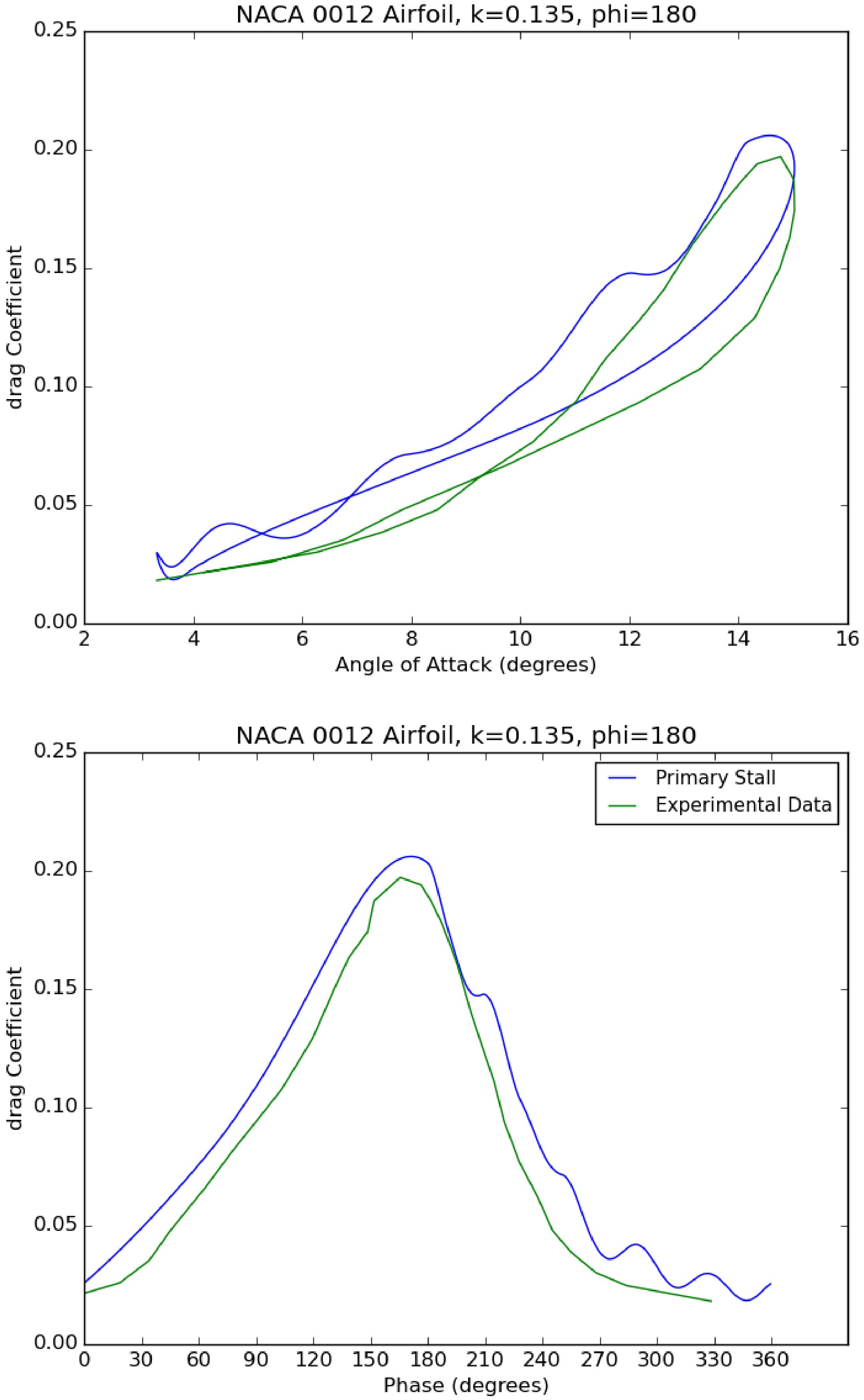

Figure 4.36 - Drag solutions for k=0.135, compared to Ref [21]

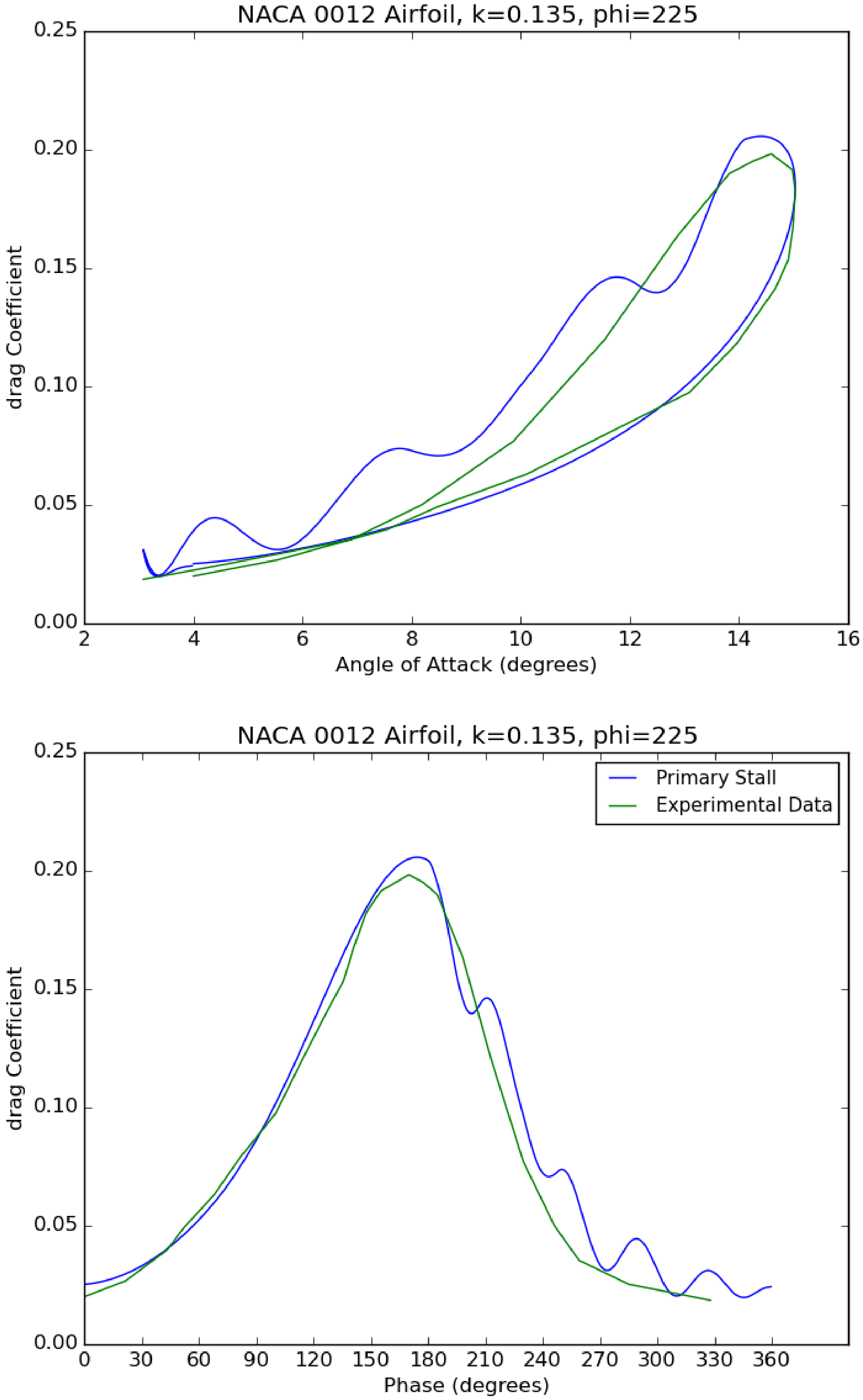

Figure 4.37 - Drag solutions for k=0.135, compared to Ref [21]

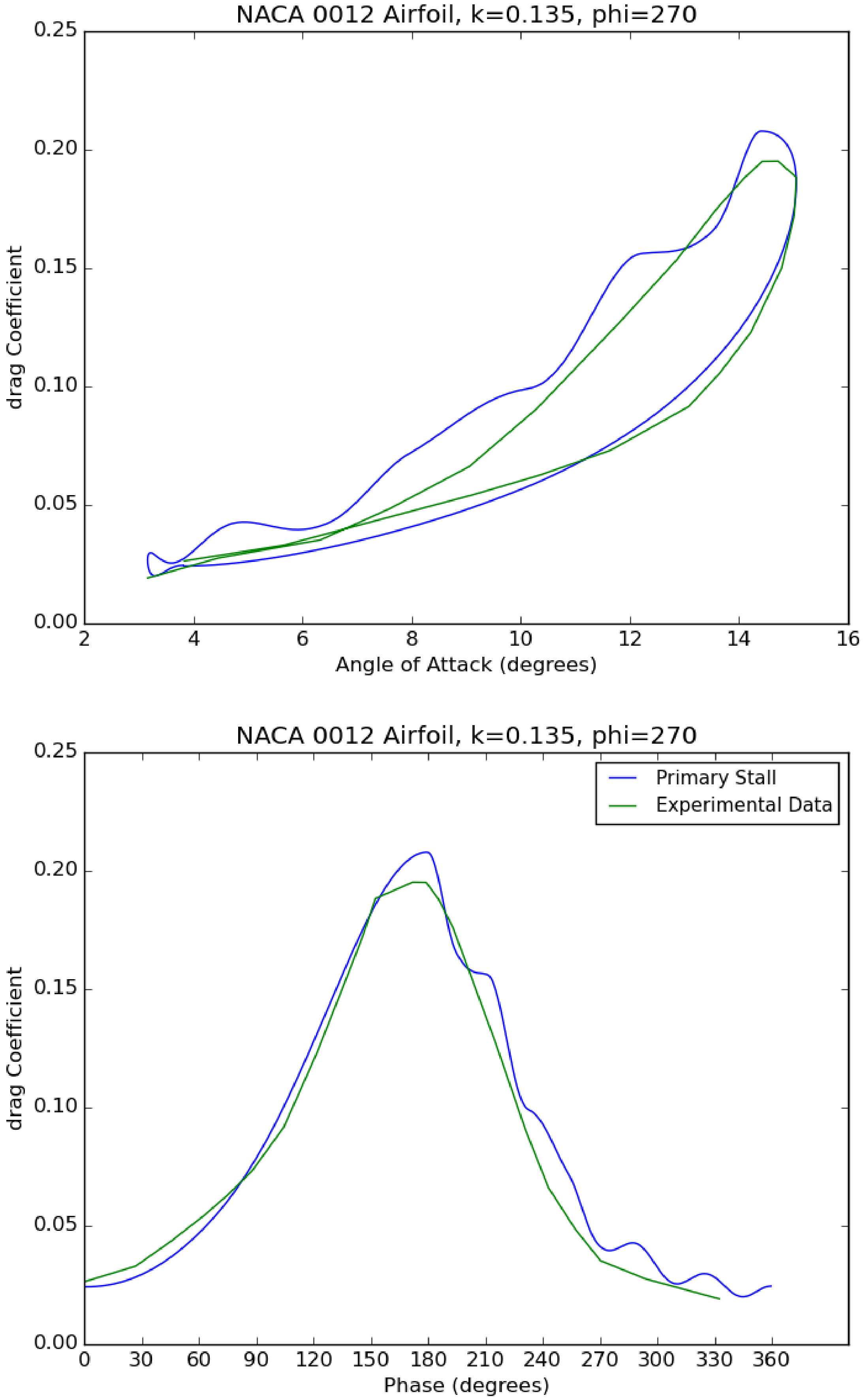

Figure 4.38 - Drag solutions for k=0.135, compared to Ref [21]

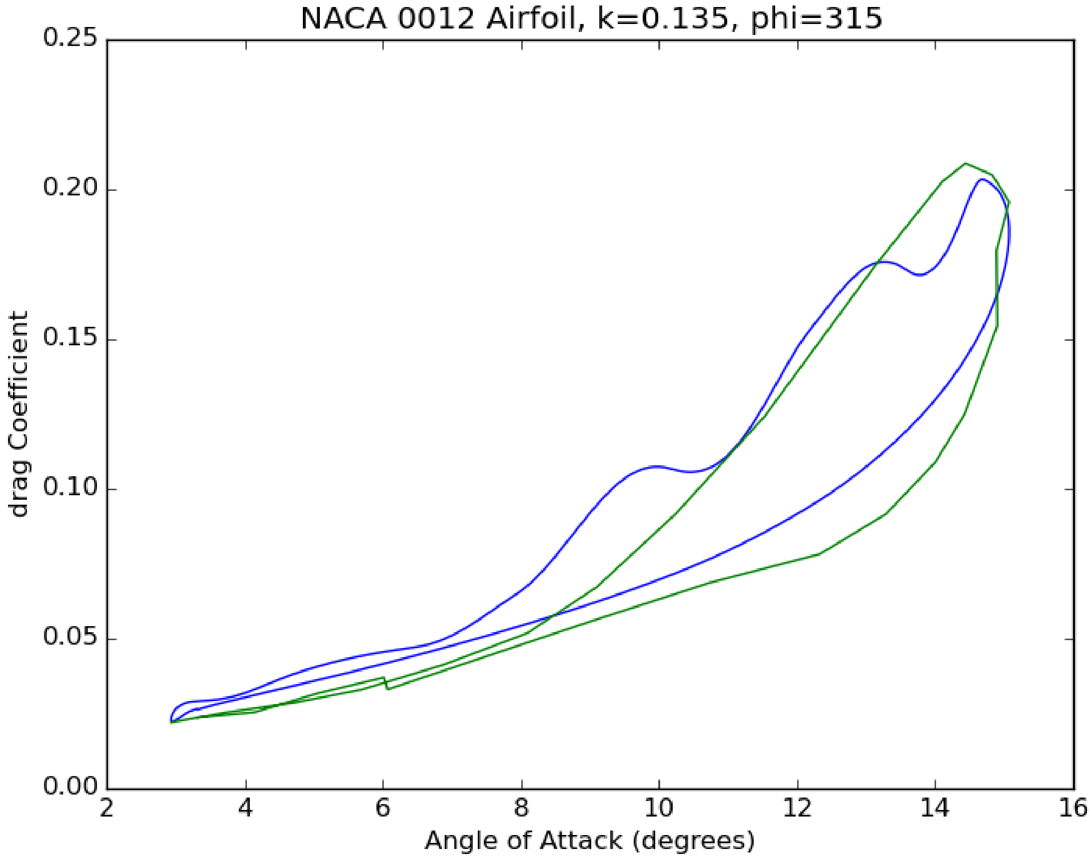

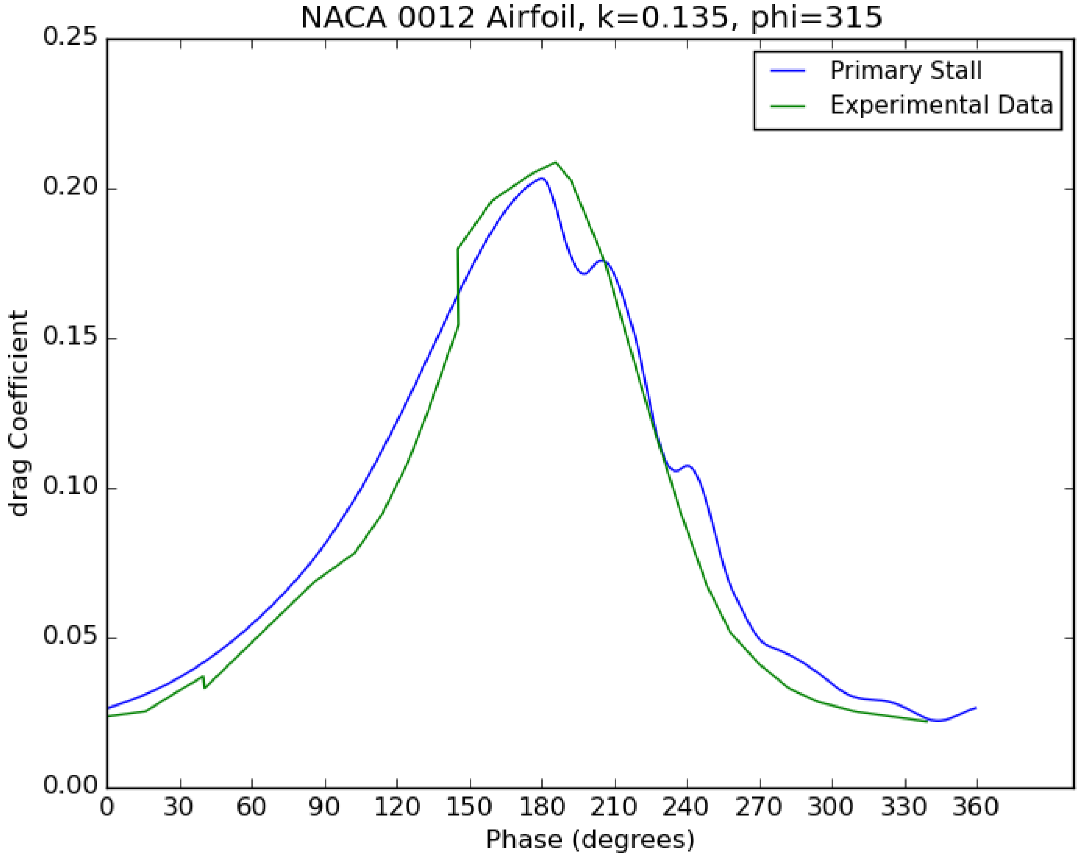

Figure 4.39 - Drag solutions for k=0.135, compared to Ref [21]

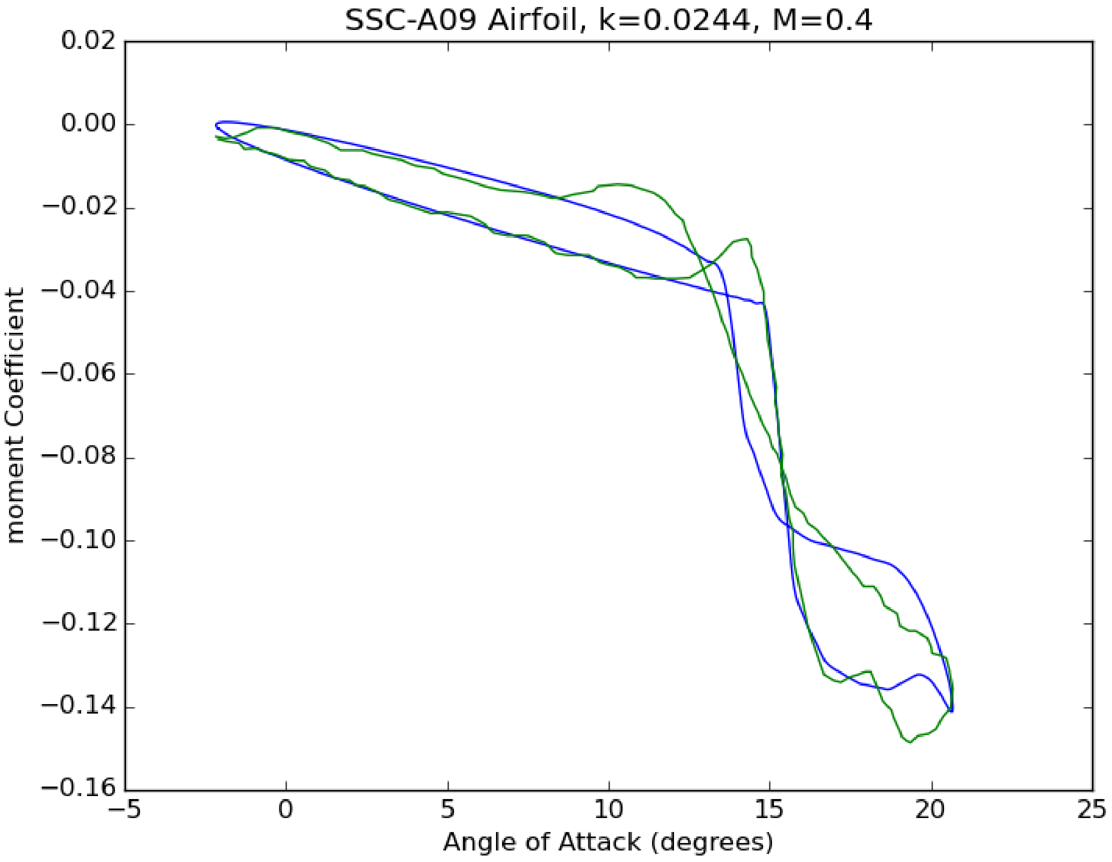

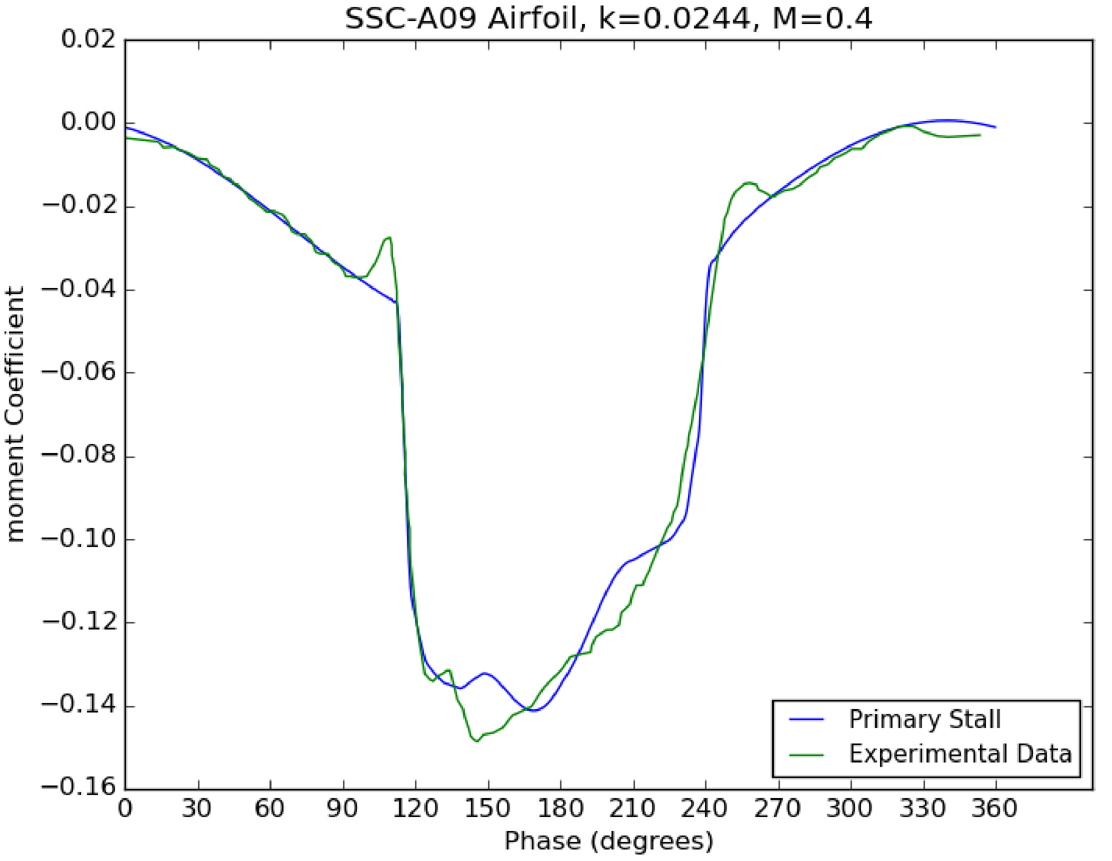

Figure 4.40 - Pitching moment solutions for k=0.0244, M=0.4, compared to Ref [22]

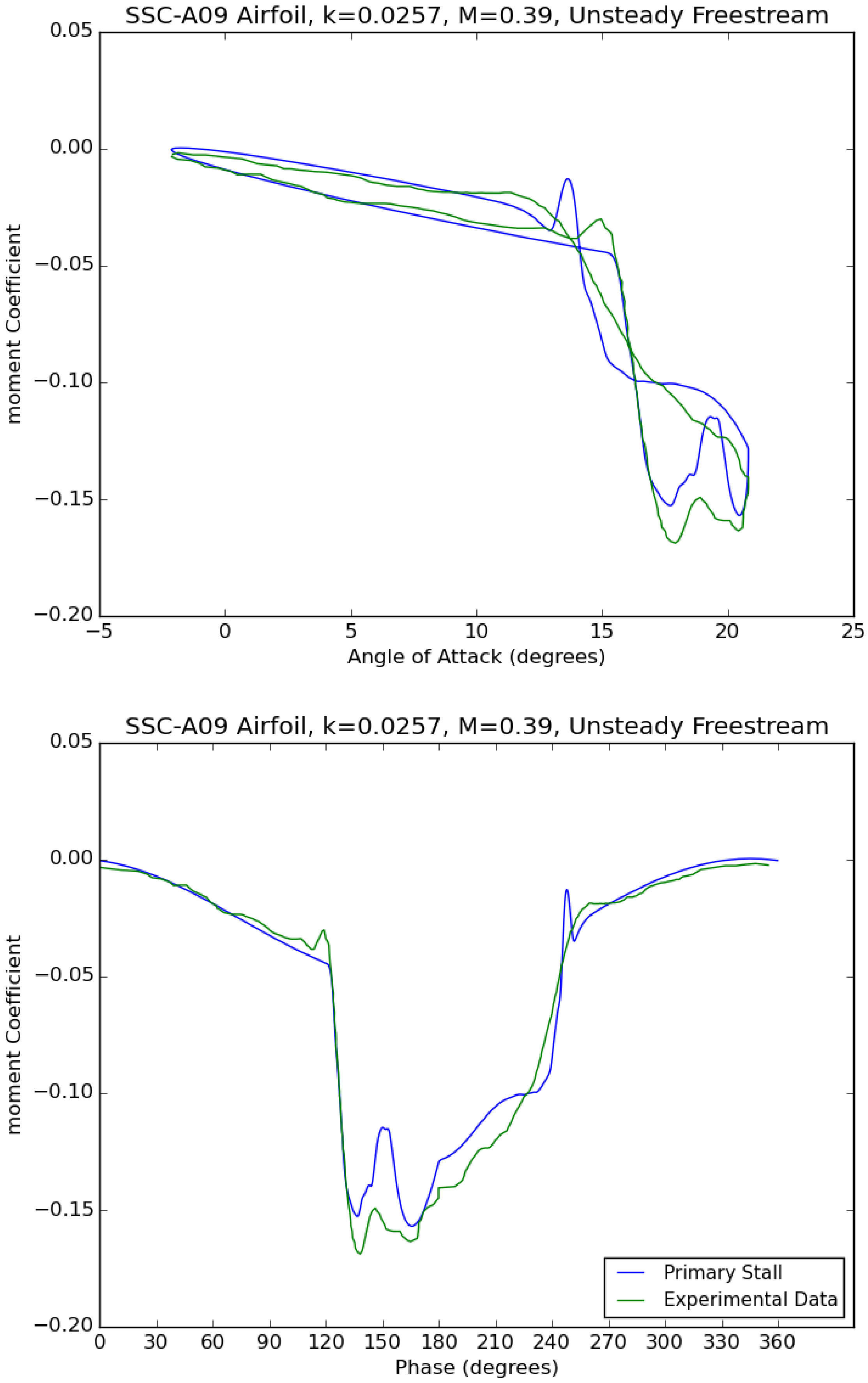

Figure 4.41 - Pitching moment solutions for k=0.0257, M=0.39, compared to Ref [22]

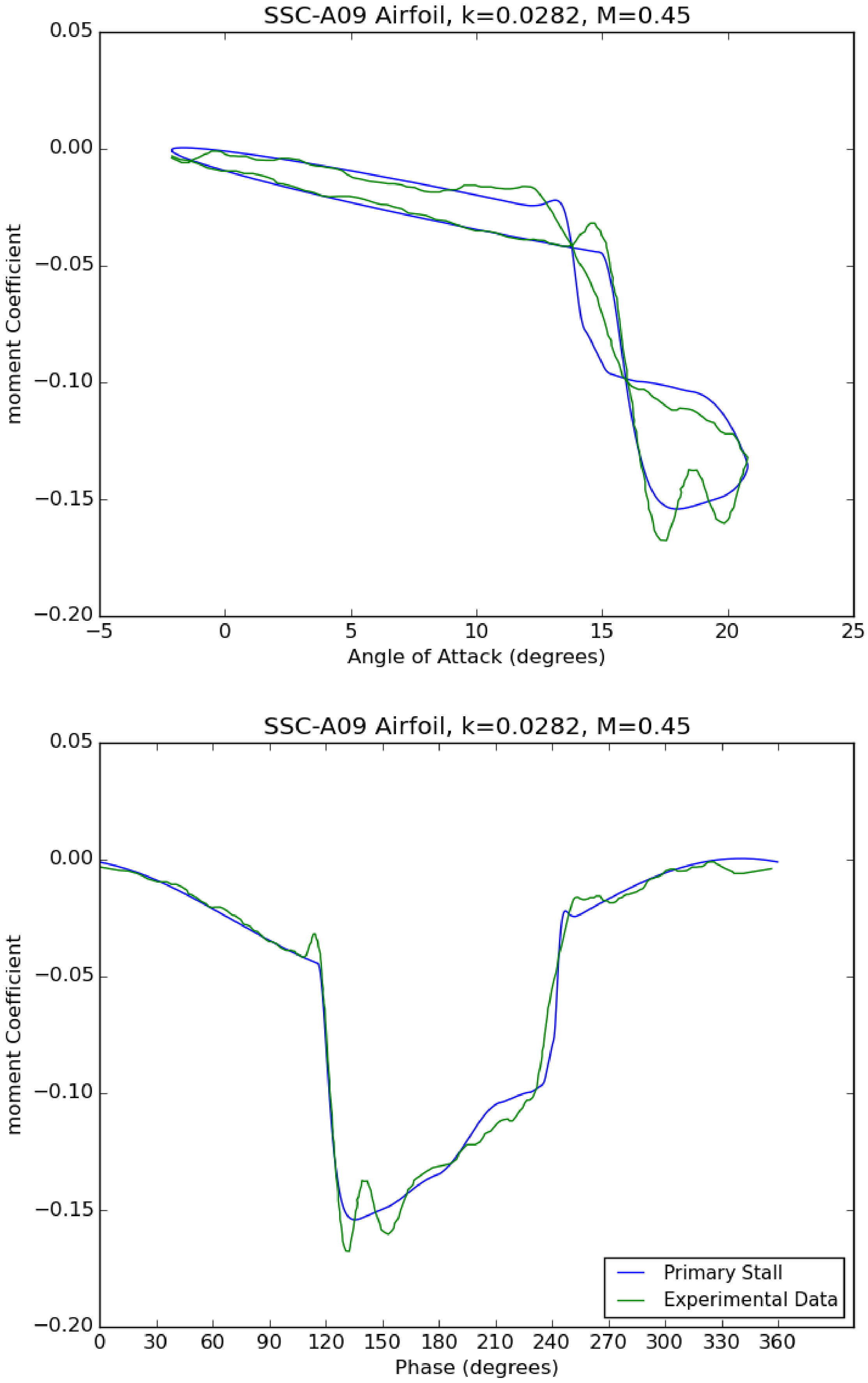

Figure 4.42 - Pitching moment solutions for k=0.0282, M=0.45, compared to Ref [22]

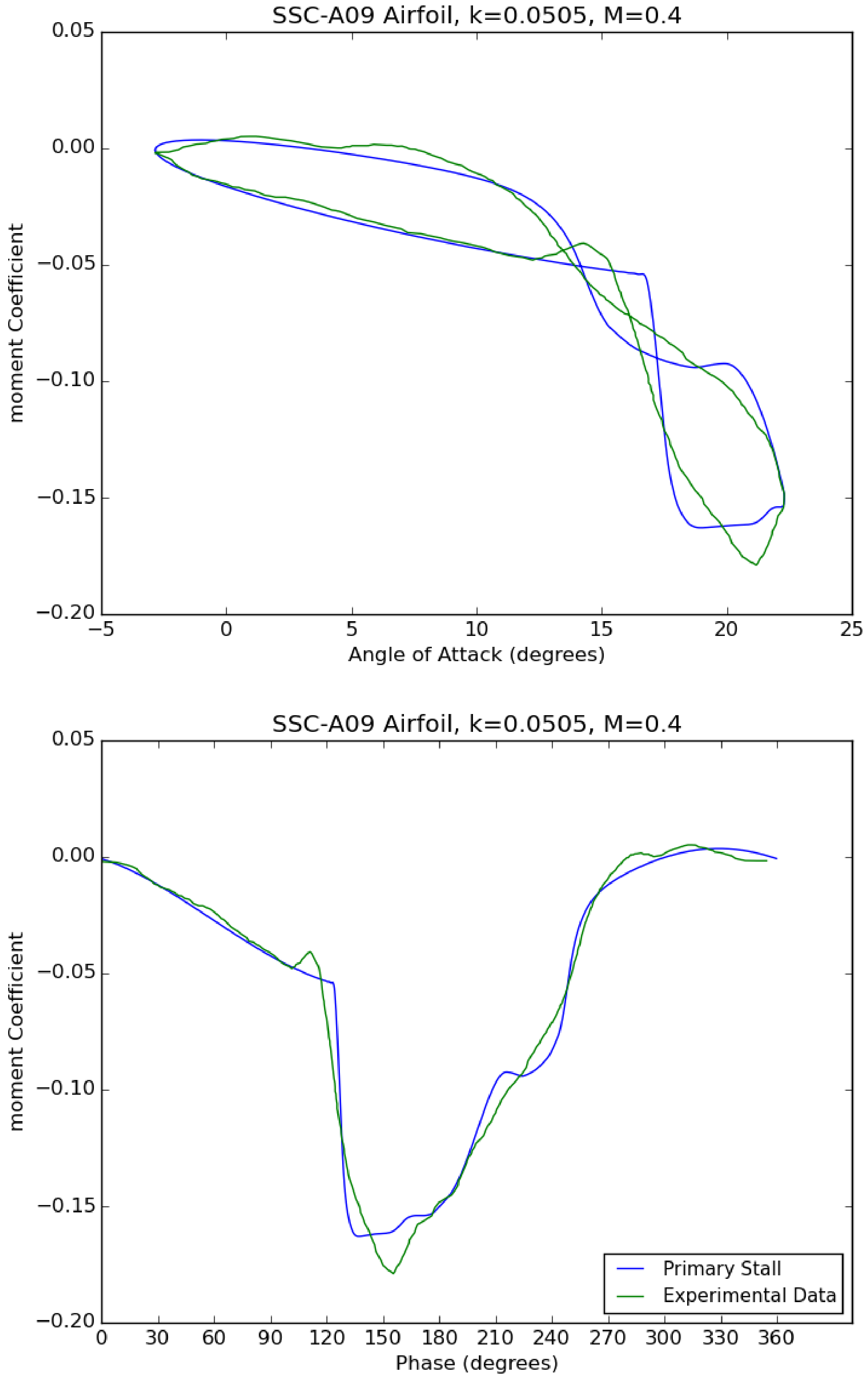

Figure 4.43 - Pitching moment solutions for k=0.0505, M=0.4, compared to Ref [22]

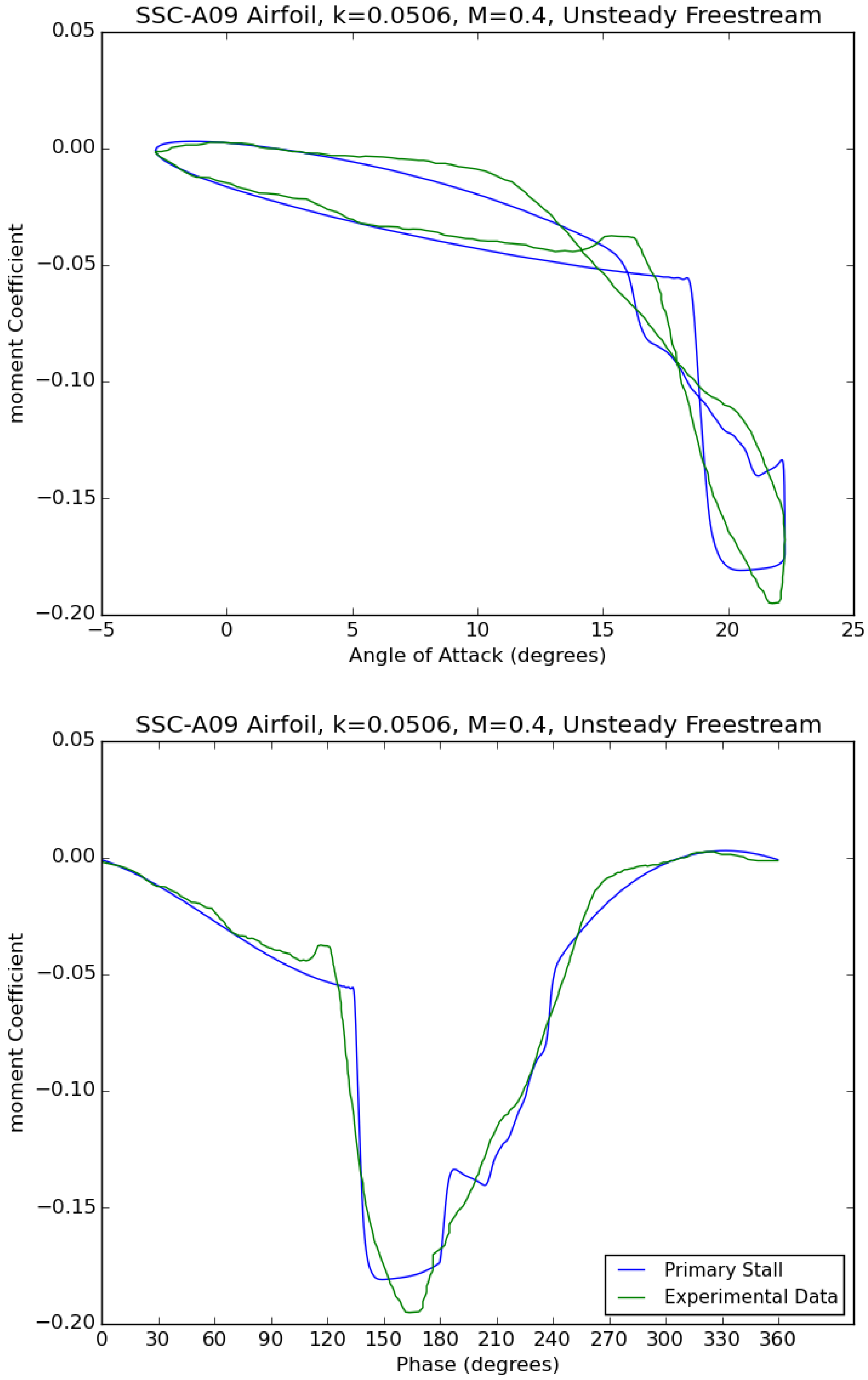
SSC-A09 Airfoil, k=0.0506, M=0.4, Unsteady Freestream

SSC-A09 Airfoil, k=0.0506, M=0.4, Unsteady Freestream

Figure 4.44 - Pitching moment solutions for k=0.0506, M=0.4, compared to Ref [22]

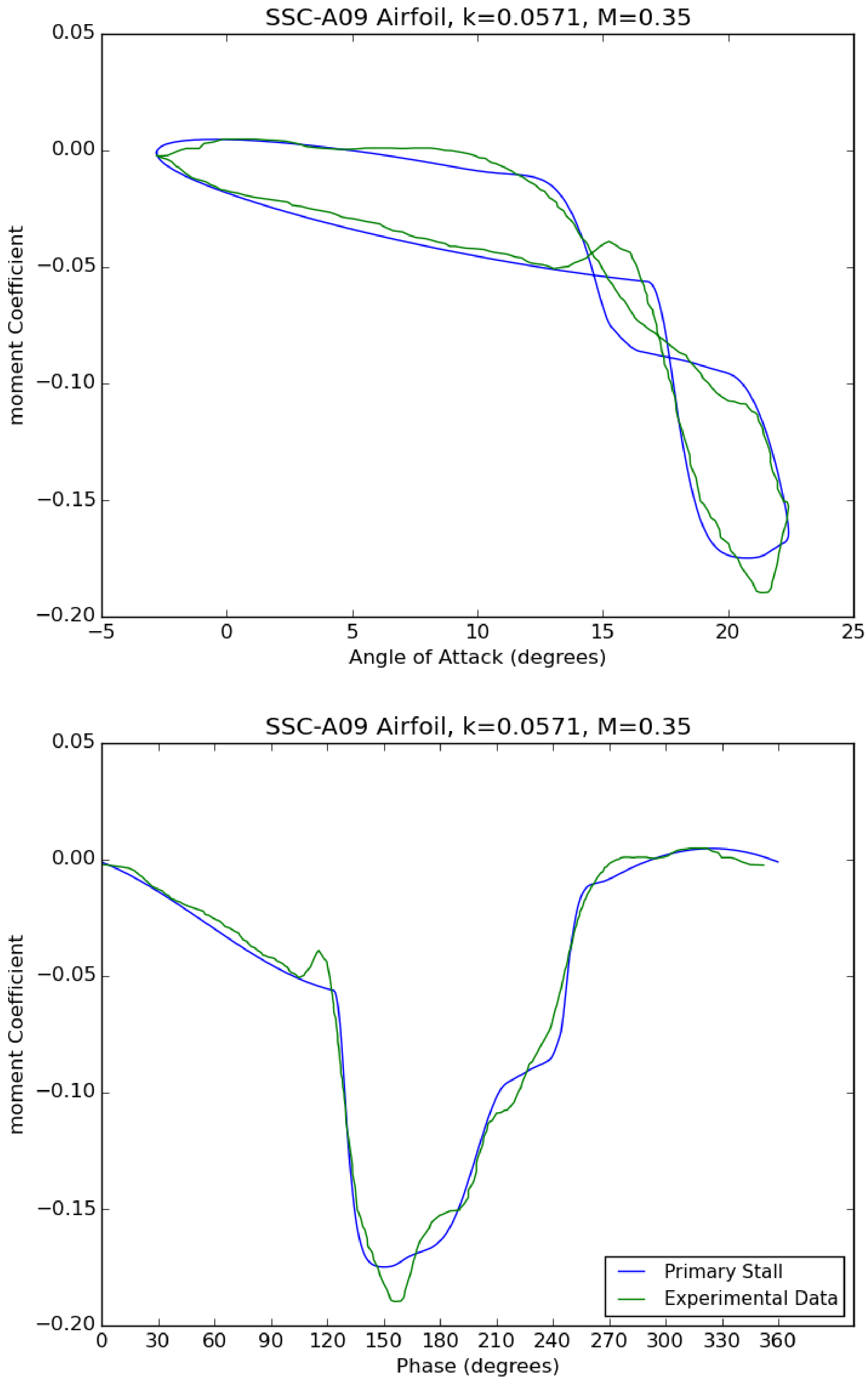

Figure 4.45 - Pitching moment solutions for k=0.0571, M=0.35, compared to Ref [22]

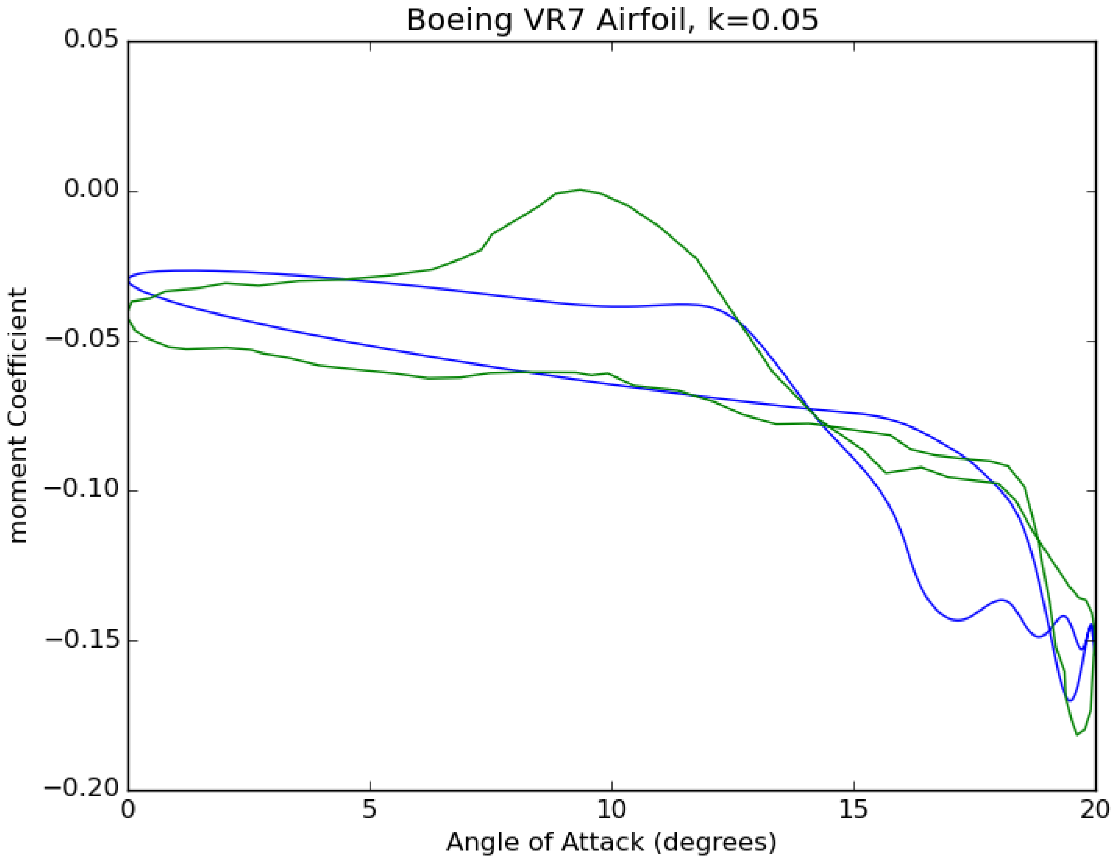

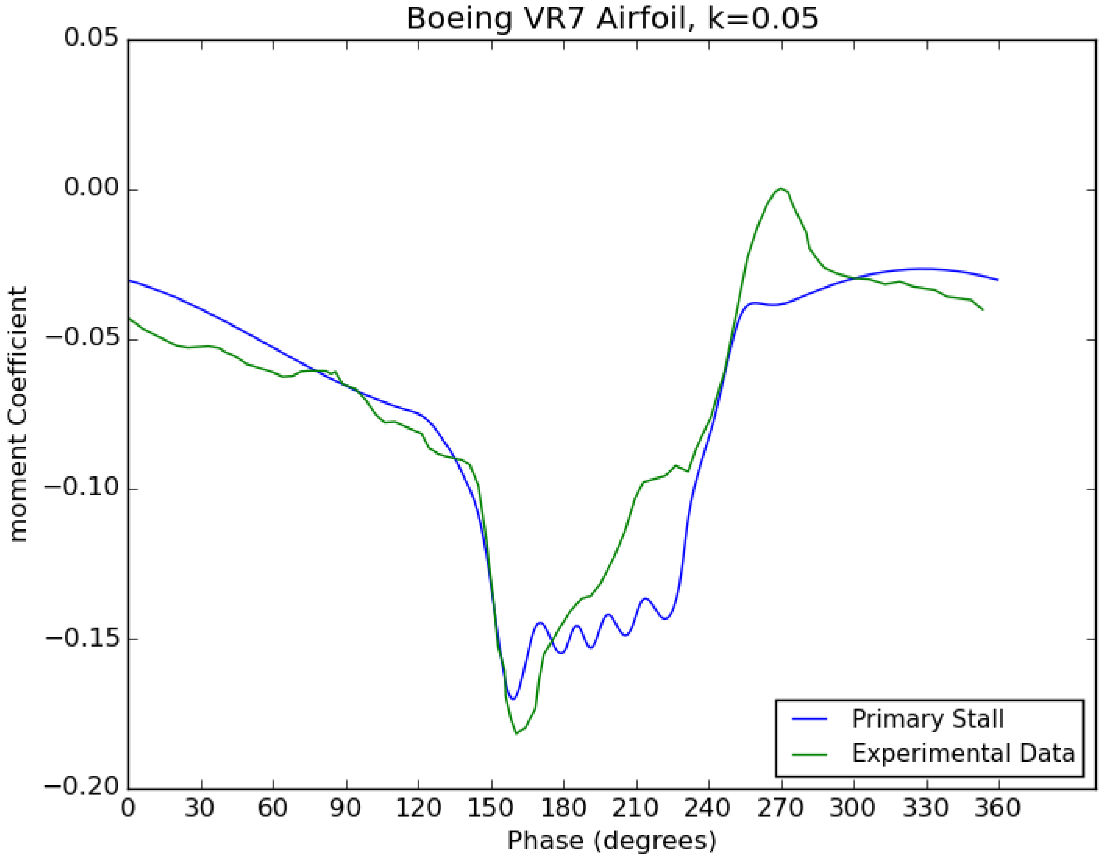

Figure 4.46 - Pitching moment solutions for k=0.05, compared to Ref [17]

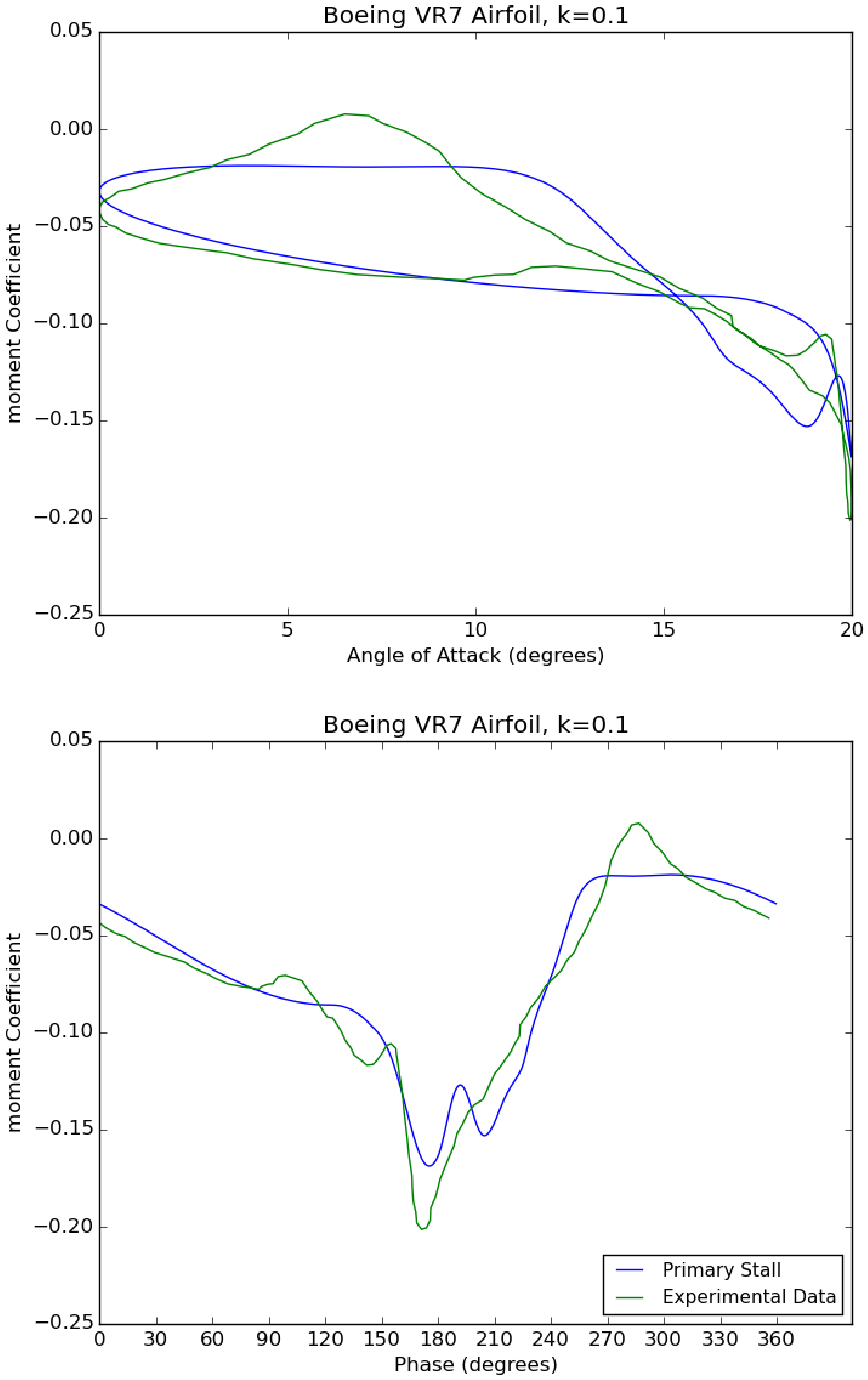

Figure 4.47 - Pitching moment solutions for k=0.1, compared to Ref [17]

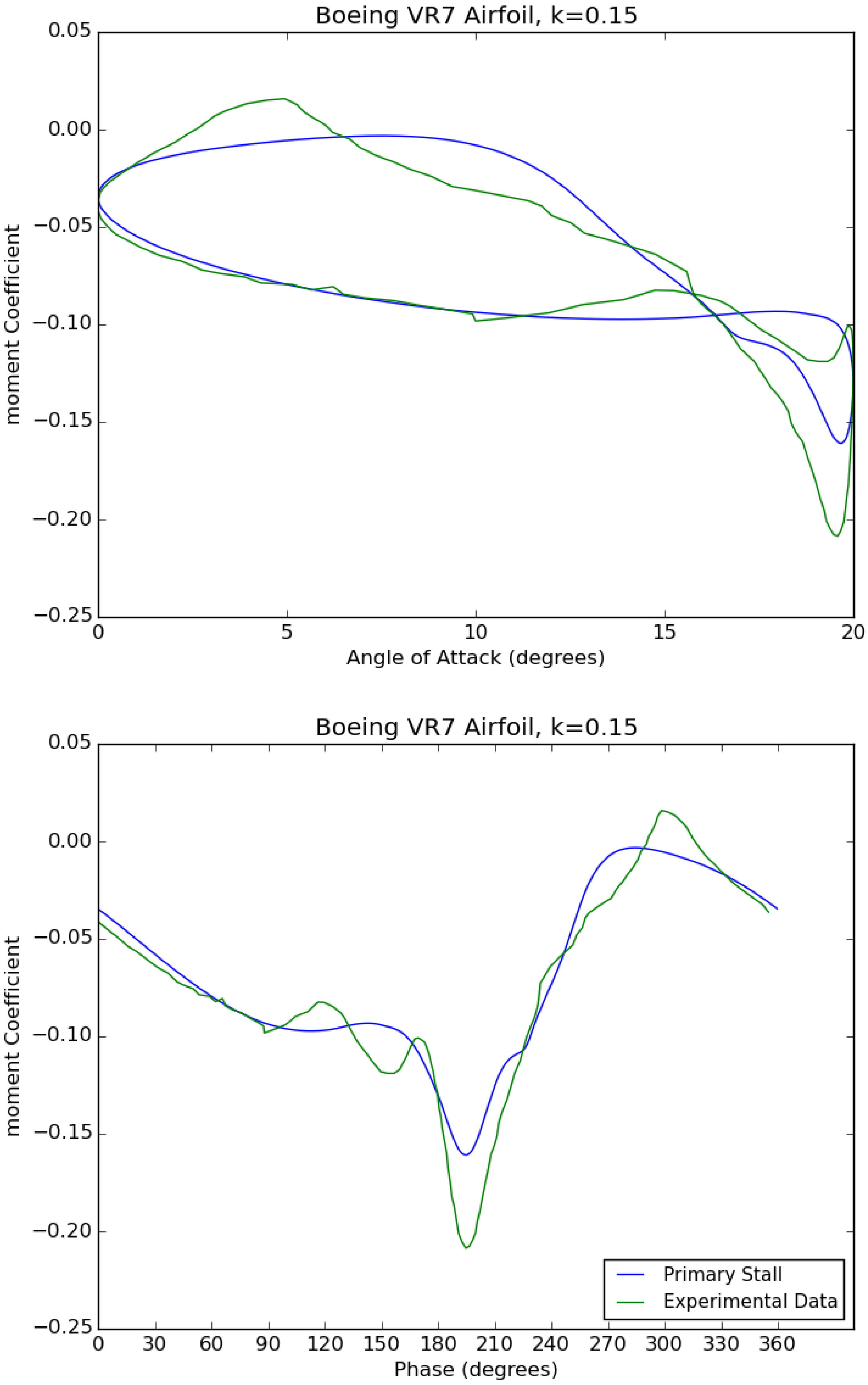

Figure 4.48 - Pitching moment solutions for k=0.15, compared to Ref [17]

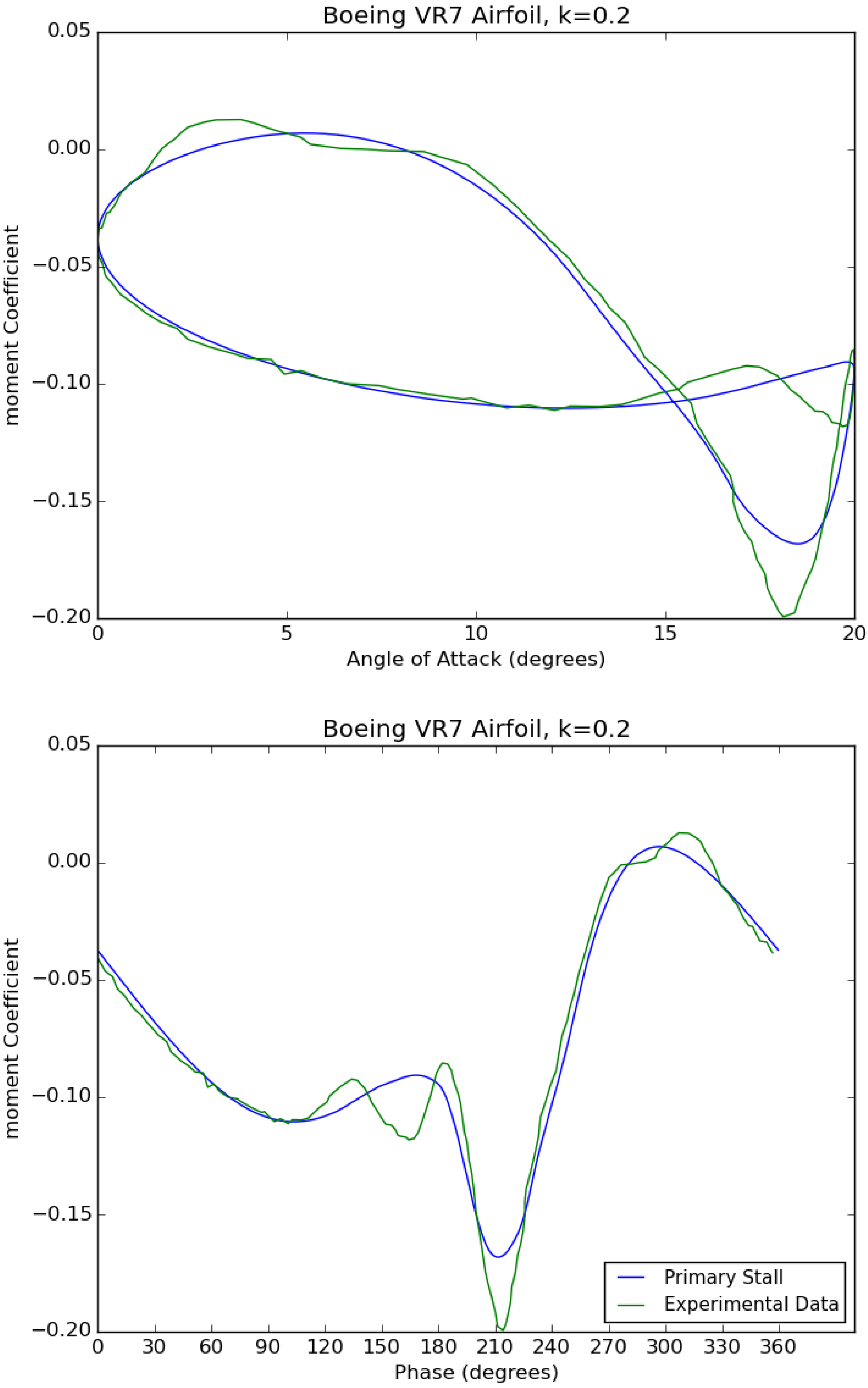

Figure 4.49 - Pitching moment solutions for k=0.2, compared to Ref [17]

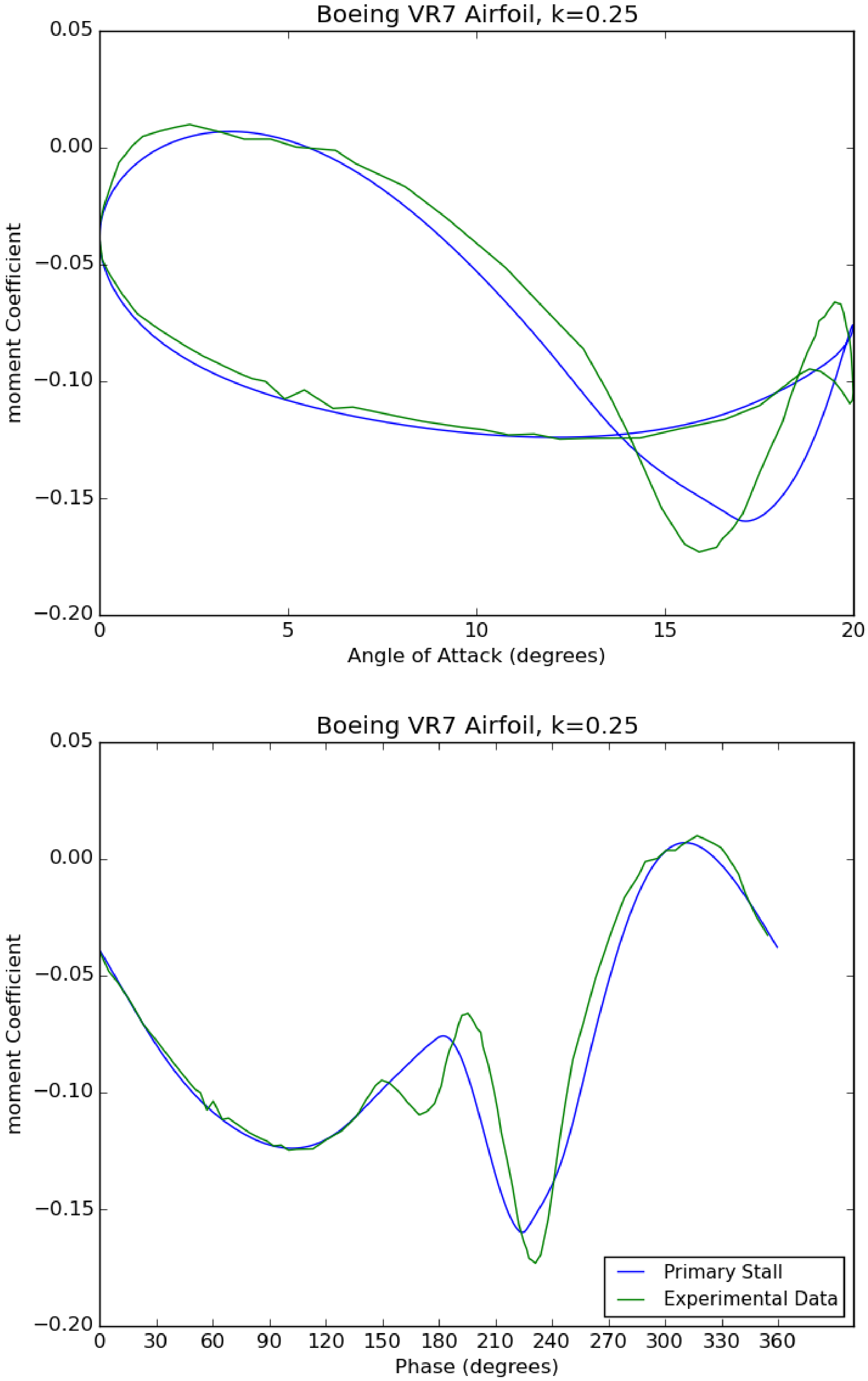

Figure 4.50 - Pitching moment solutions for k=0.25, compared to Ref [17]

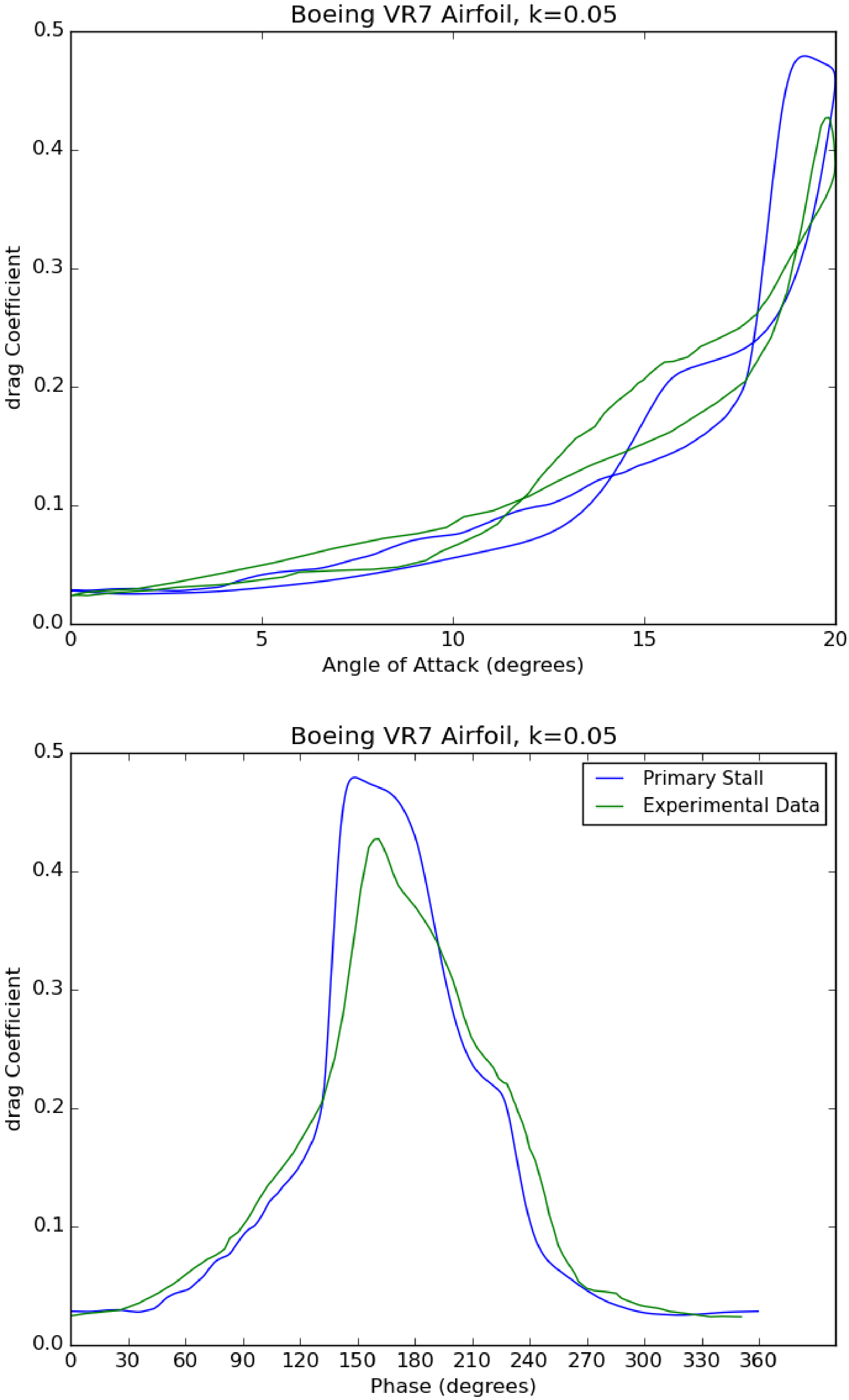

Figure 4.51 - Drag solutions for k=0.05, compared to Ref [17]

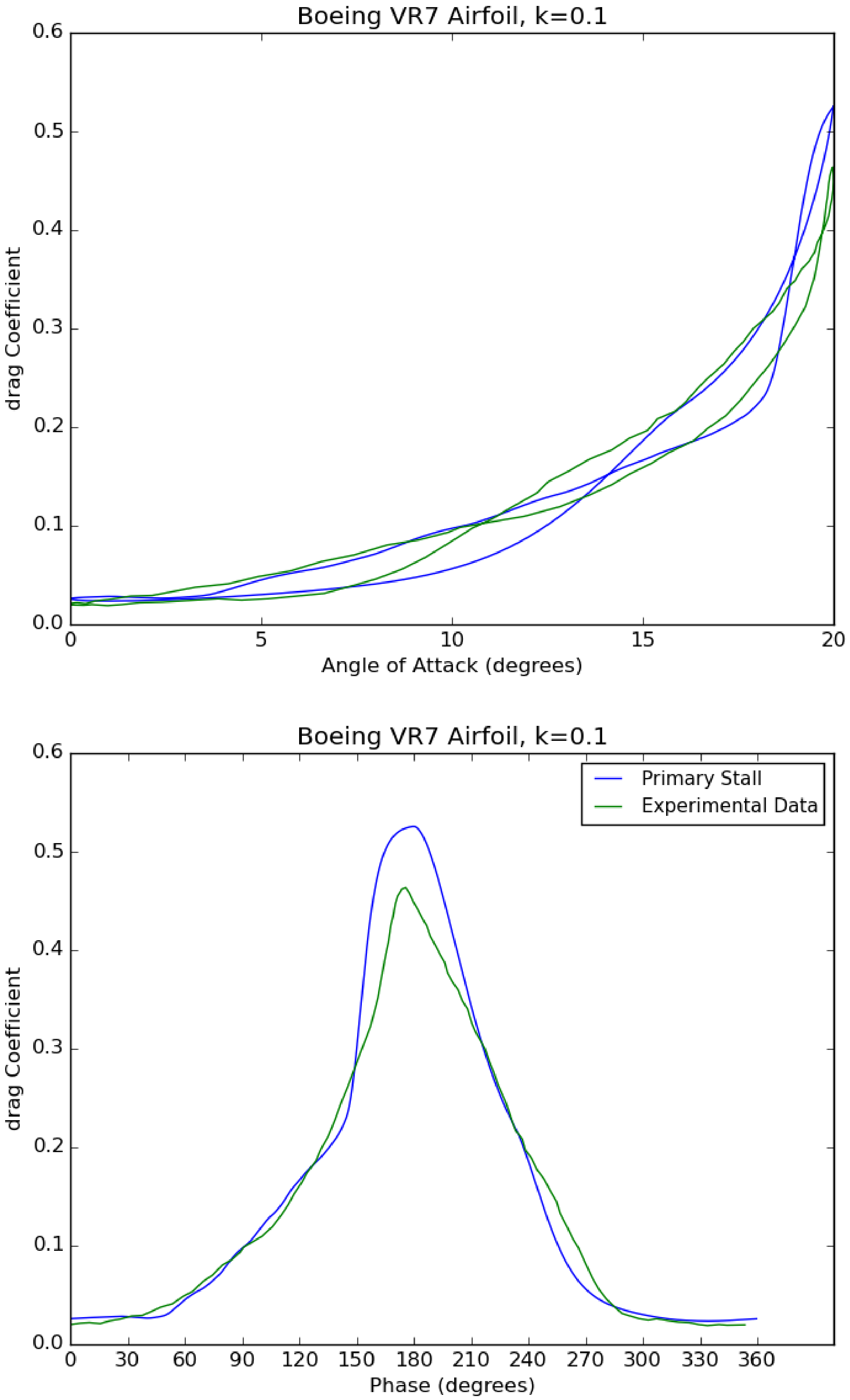

Figure 4.52 - Drag solutions for k=0.1, compared to Ref [17]

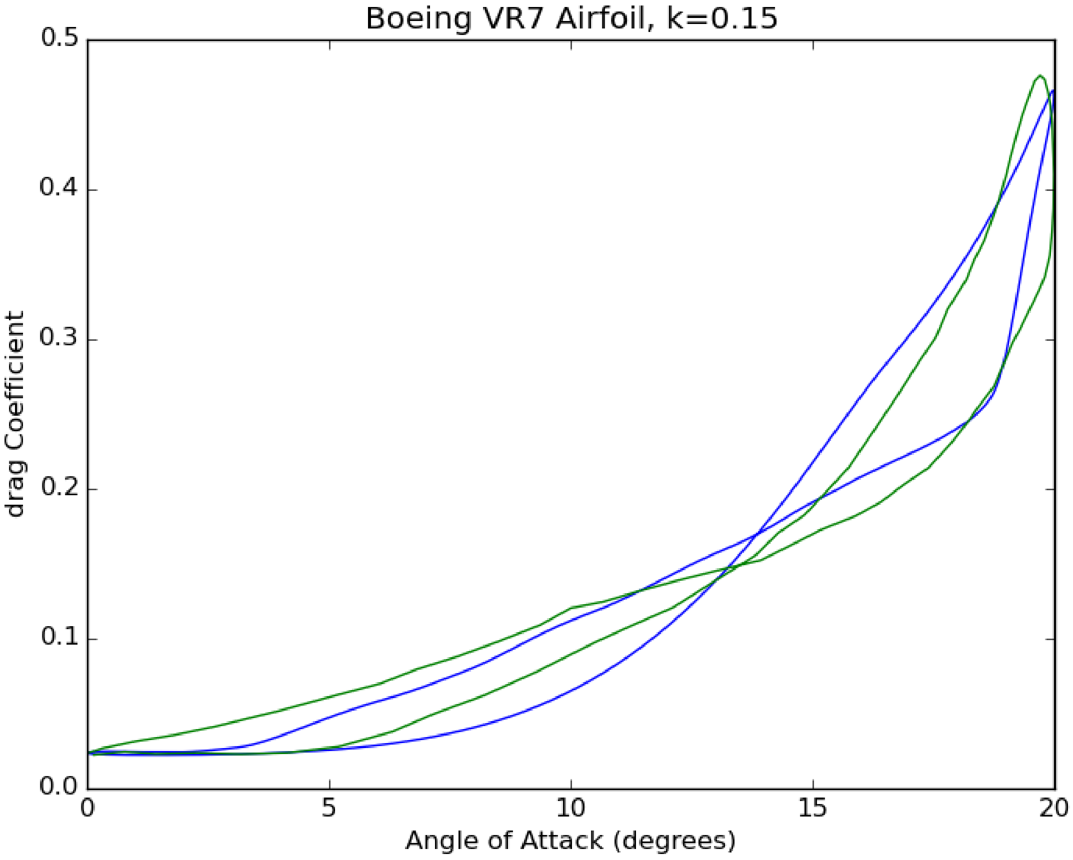

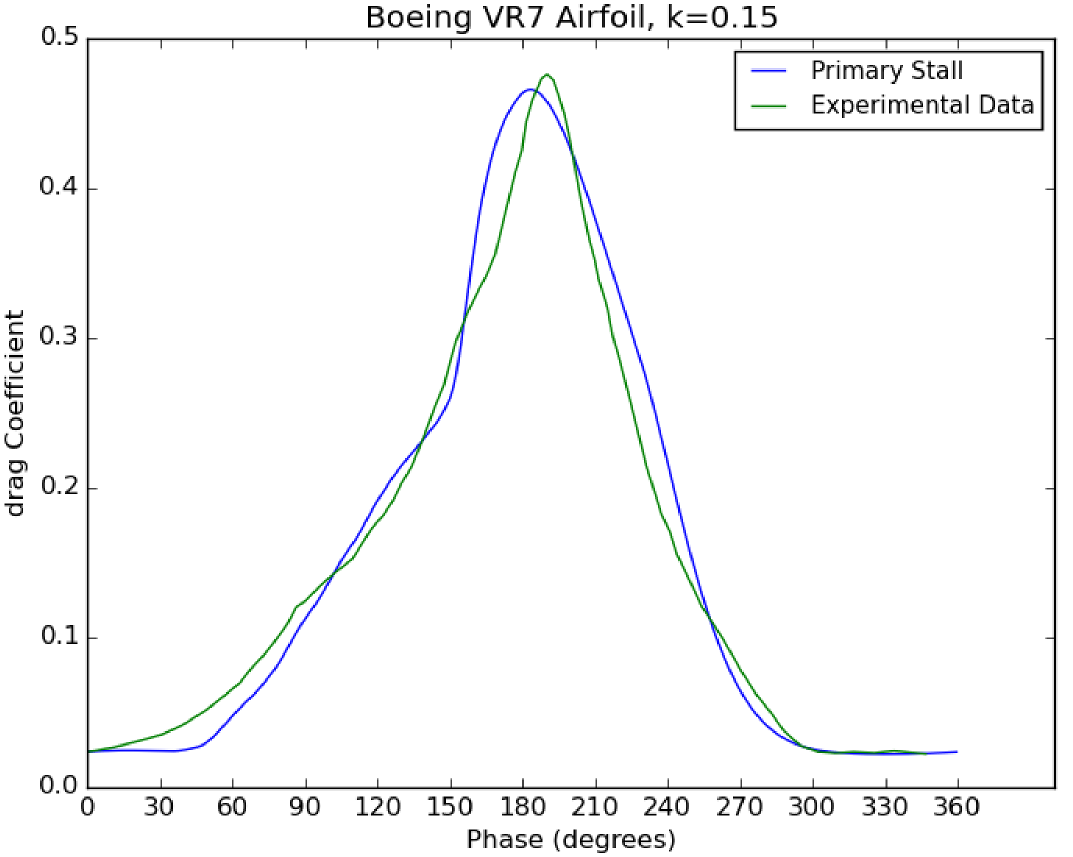

Figure 4.53 - Drag solutions for k=0.15, compared to Ref [17]

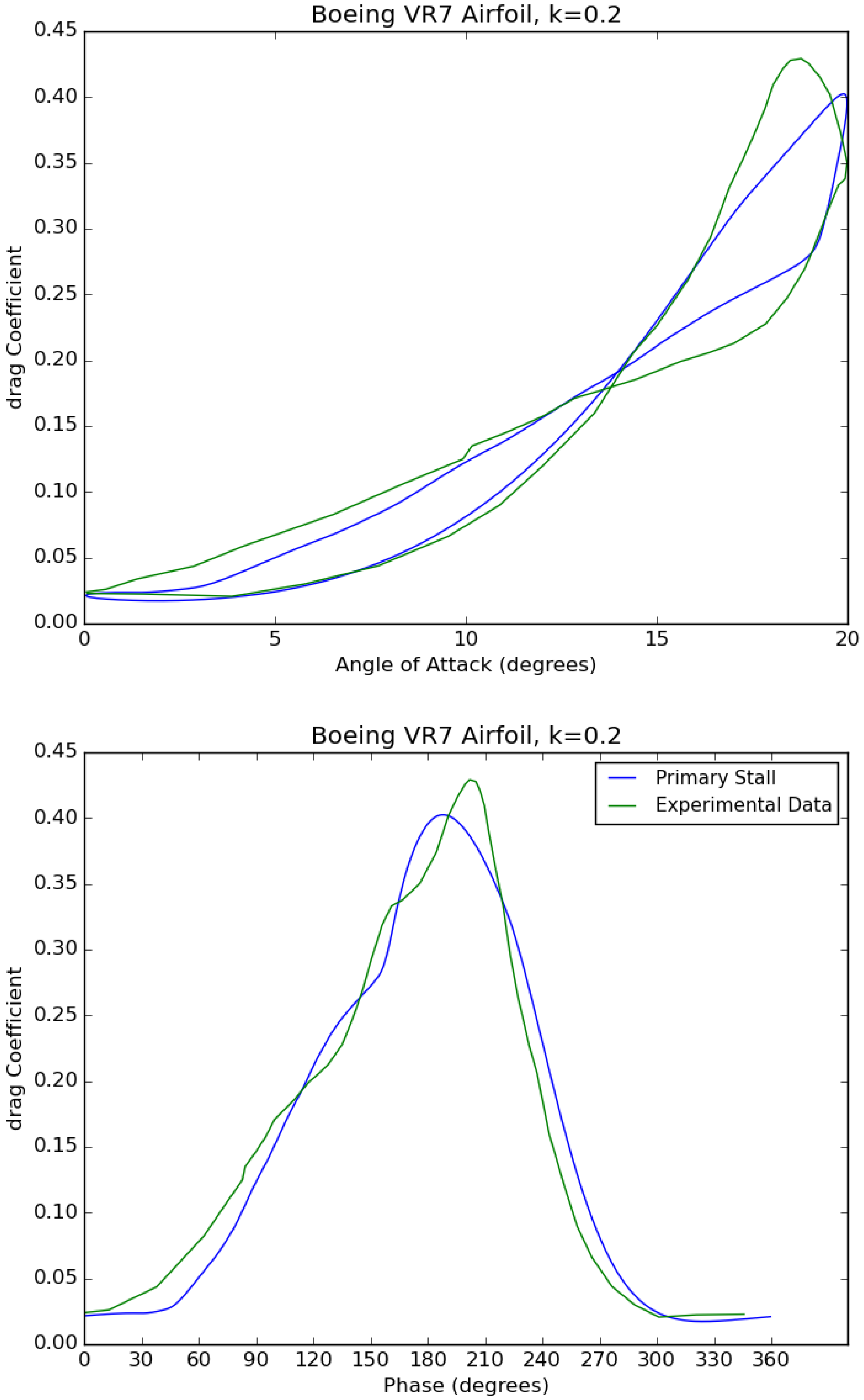

Figure 4.54 - Drag solutions for k=0.2, compared to Ref [17]

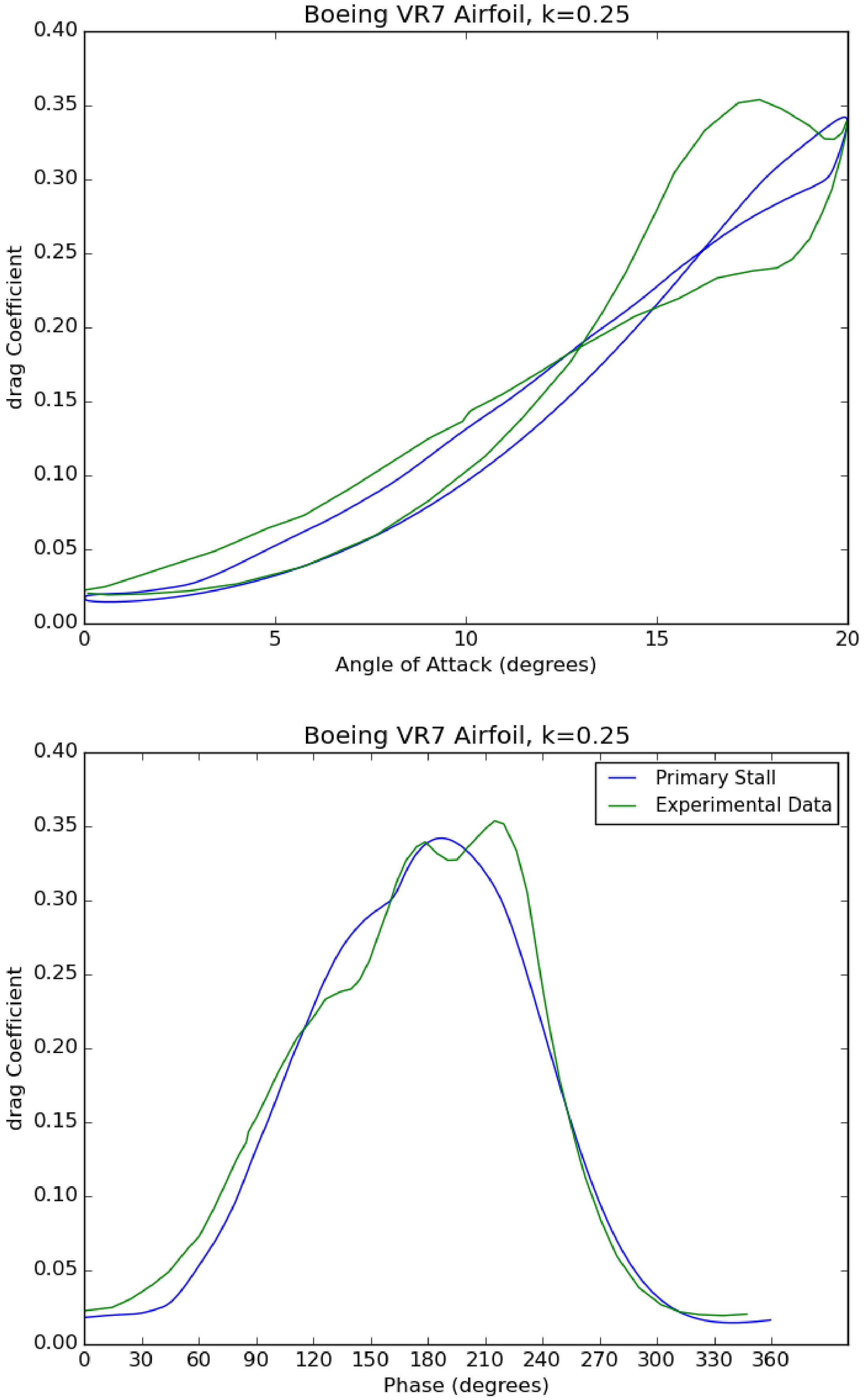

Figure 4.55 - Drag solutions for k=0.25, compared to Ref [17]

Chapter 5: Summary and Conclusions

This work developed and validated a state-space dynamic stall model for predicting pitching moment and drag of rotor blades. The Unified model developed in Chapter 2 is a hierarchical, reduced-order model suitable for real-time flight simulation. Eight inflow states and two stall circulation states are sufficient to model an airfoil in 2D flow for arbitrary freestream conditions. Stall parameters were determined via an optimization routine that minimized the 2-norm error of the difference between our modelled solution and experimental data. The "frozen inflow method" of Section 3.1 reduced the computing time during optimization by a factor of nine by making assumptions to decouple the inflow and stall equations. Data from several wind tunnel experiments were tested that contain unsteady freestream, yawed flow, and secondary stall effects.

The results of Chapter 4 showed how the stall model can simulate pitching moment and drag for five different datasets. The results for the Boeing VR-12 data of Ref [16] show close correlation of both pitching moment and drag for three Mach numbers and two reduced frequencies, including secondary stall. The yawed flow results of Section 4.3 show that yaw effects in 2D can be modelled using the yawed static data. The unsteady freestream results of Sections 4.4 and 4.5 show how the small corrections to the loads in Eqs. 2.36-2.40 can account for the unsteady freestream conditions in Refs [21] and [22]. For the VR-7 data of Ref [17], a single set of stall parameters was found to give reasonable correlation for a range of reduced frequencies.

Chapter 6: Future Work

The Peters-Modarres stall model has yet to be validated against any three-dimensional data. While Modarres considered 3D effects, he did not have wind tunnel tests or flight test data to compare with the model. Dynamic stall in an actual helicopter rotor is a 3D phenomenon, so these kinds of data are the next important data in the validation of the Unified model.

The best kind of test to validate this stall model in 3D would be a full-rotor wind tunnel test with effectively rigid blades. A flexible rotor blade undergoing dynamic stall would also have significant flapping, lead-lag, and torsional motion; this would require a structural model coupled to our stall model in order to validate. Creating and using a structural model is a project by itself, and could introduce errors that would hinder the validation of the stall model, so it is very preferable to use data that does not have these blade motions. With the entire rotor inside of the wind tunnel, a 3D wake would be generated as in a real helicopter, and the stall vortices would affect other sections of the same blade, or even other blades. In Section 6.2 of Modarres [14], he made modifications to the stall model to include the effect of radial coupling, and with a stiff full-rotor wind tunnel test, this radial coupling equation could be validated.

The problem with rigid-rotor tests is simple: there are none available. One the other hand, tests of flexible rotor blades undergoing dynamic stall in both wind tunnels and flight environments are much more available. Ref [37] is a flight test of a UH-60 helicopter during three dynamic stall-inducing conditions: a pull-up maneuver, a high-speed diving turn, and trim level flight. This test also shows generation of dangerously large pitch-link loads during the dynamic stall events. Ref [38] contains flight test and wind tunnel data of a bearingless rotor undergoing dynamic stall, with measured pitch-link loads. These non-rigid rotor tests are not as useful to us as rigid ones, but are still capable of being validated.

References

1. Johnson, Wayne. *Helicopter Theory,* Princeton University Press, Princeton, 1980, pp. 873-902

2. Hirschberg, Mike, "JMR Technology Demonstration Update" *Vertiflight,* Vol. 62, No. 1, January/February 2016, pp. 22-30

3. Norman D. Ham. "Stall Flutter of Helicopter Rotor Blades: A Special Case of the Dynamic Stall Phenomenon" *Journal of the American Helicopter Society,* Volume 12, Number 4, 1 October 1967, pp. 19-21(3)

4. Carta, Franklin O., "An Analysis of the Stall Flutter Instability of Helicopter Rotor Blades," *Journal of the American Helicopter Society*, Volume 12, Number 4, 1 October 1967, pp. 1-18(18)

5. Quackenbush, Todd R., *Journal of the American Helicopter Society,* Volume 29, Number 3, 1 July 1984, pp. 38-44(7)

6. Tarzanin, F. J., Jr., "Prediction of Control Loads due to Blade Stall," *Journal of the American Helicopter Society*, Volume 17, Number 2, 1 April 1972, pp. 33-46(14)

7. Tran, C. T.; and Pitot, D., "Semi-Empirical Model for the Dynamic Stall of Airfoils in View of the Application to the Calculation of the Responses of a Helicopter Blade in Forward Flight," *Vertica*, 5(1), 1981, pp. 35-53.

8. Petot, D., "Progress in the Semi-Empirical of the Aerodynamic Forces due to Large Amplitude Oscillations of an Airfoil in Attached or separated flow," ONERA TP 1983-111, 1983.

9. Leishman, J. G.; and Beddoes, T. S., "A Generalized Method for Unsteady Airfoil Behavior and Dynamic Stall Using the Indicial Method," 42nd Annual Forum of the American Helicopter Soc., Washington DC, June, 1986, pp. 243-265.

10. Carta, F. O. *et al.*, "Investigation of Airfoil Dynamic Stall and Its Influence on Helicopter Control Loads," U.S. Army AMRDL-Eustis Directorate Report TR-72-51, 1972.

11. Bielawa, Richard. L., "Synthesized Unsteady Airfoil Data with Application to Stall Flutter Calculations," Proceedings of the 31st Annual National Forum of the American Helicopter Society, Washington, D.C., May 13-15, 1975, Preprint No. 935.

12. Johnson, W., "The effect of Dynamic Stall on the Response and Airloading of Helicopter Rotor Blades," *Journal of the American Helicopter Society*, vol. 14, no. 2, April 1969, pp. 68-

79
13. Johnson, W., "Comparison of Three Methods for Calculation of Helicopter Rotor Blade Loading and Stresses Due to Stall," NASA TN D-7833, 1974.
14. Modarres, Ramin, "Semi-Empirical Modeling of Two-Dimensional and Three-Dimensional Dynamic Stall" (2016). Engineering and Applied Science Theses & Dissertations. Paper 161.
15. Ahaus, Loren A., *An Airloads Theory for Morphing Airfoils in Dynamic Stall with Experimental Correlation,* PhD thesis, Washington University in Saint Louis
16. Martin, P.B., McAlister, K.W., Chandrasekhara, M.S., and Geissler, W., "Dynamic Stall Measurements and Computations for a VR-12 Airfoil with a Variable Droop Leading Edge," Proceedings of the American Helicopter Society 59th Annual Forum, Phoenix, Arizona, May 2003, pp. 473-489
17. McAlister, K.W., Lambert, O., and Petot, D., "Application of the ONERA Model of Dynamic Stall." NASA TP 2399, AVSCOM TR 84-A-3, 1984
18. St. Hilaire, A. O., Carta, F. O., Fink, M. R.; and Jepson, W. D., "The Influence of Sweep on the Aerodynamic Loading of an Oscillating NACA 0012 Airfoil," Vol. 1-Technical Report, NACA CR 3092, 1979.
19. St. Hilaire, A. O.; and Carta, F. O., "The Influence of Sweep on the Aerodynamic Loading of an Oscillating NACA 0012 Airfoil," Vol. 2-Data Report, NASA CR 145350, 1979.
20. Maresca, C.A. Favier, Rebont. "Unsteady Aerodynamics of an Aerofoil at high angle of incidence performing various linear oscillations in a uniform stream" *Journal of the American Helicopter Society,* Volume 26, Number 2, 1 April 1981, pp. 40-45(6)
21. Favier, D., Belleudy, J.; and Maresca, C., "Influence of Coupling Incidence and Velocity Variations on the Airfoil Dynamic Stall," Proceedings of the American Helicopter Society 48th Annual Forum, Washington DC, 1992, pp. 1385-1407.
22. Naigle, et al, "Experimental Modeling of Compressible Dynamic Stall in Unsteady Flow through Interpolation of Phase-Marched Conditions in Steady Flow," Proceedings of the AHS Specialists' Conference on Aeromechanics Design for Vertical Lift, San Francisco, California, January 20-22, 2016.
23. Hird, K., Frankhouser, M. W., Gregory, J. W.; and Bons, J., "Compressible Dynamic Stall of an SSC-A09 Airfoil Subjected to Coupled Pitch and Freestream Mach Oscillations,"

Proceedings of the American Helicopter Society 70th Annual Forum, Montreal, Quebec, Canada, May 20-22, 2014.

24. Chen, Chi-Tsong. *Linear System Theory and Design.* 3rd edition. Oxford University Press, 1999, pp. 86-116.

25. Peters, David A. and He, Cheng Jian, “Finite-State Induced Flow Models, Part II: Three-Dimensional Rotor Disk,” Journal of Aircraft, Vol. 32, No. 2, March-April 1995, pp. 323-333.

26. Peters, David A., “How Dynamic Inflow Survives in the Competitive World of Rotorcraft Aerodynamics,” the 2008 Alexander Nikolsky Lecture, *Journal of the American Helicopter Society*, Vol. 54, No. 1, January 2009, pp. 1-15.

27. Peters, David A.; and Johnson, Mark J., "Finite-State Airloads for Deformable Airfoils on Fixed and Rotating Wings," Presented at the Symposium on Aeroelasticity and Fluid/Structure Interaction, American Society of Mechanical Engineers, Chicago, IL, November 6-11, 1994.

28. Peters, David A., Karunamoorthy, Swami, and Cao, Wen-Ming, “Finite-State Induced Flow Models, Part I: Two-Dimensional Thin Airfoil,” Journal of Aircraft, Vol. 32, No. 2, March-April 1995, pp. 313-322.

29. Abbott, Ira, and Von Doenhoff, Albert. *Theory of Wing Sections*. Dover Publications New York, Inc. 1959. pp. 64-79

30. Peters, David A. “Toward a Unified Lift Model for Use in Rotor Blade Stability Analyses,” *Journal of the American Helicopter Society,* Volume 30, Number 3, 1 July 1985, pp. 32-42(11)

31. He, Chengjian, *Development and Application of a Generalized Dynamic Wake Theory for Lifting Rotors*, Doctor of Philosophy Thesis, Georgia Institute of Technology, July, 1989.

32. https://bitbucket.org/mwmalick/stall/src/master. Accessed August 18, 2018.

33. Hamming, R. W., *Numerical Methods for Scientists and Engineers,* McGraw-Hill Book Company, Inc., 1962, pp. 211-212

34. S. Kirkpatrick, C. D. Gelatt Jr., M. P. Vecchi. Optimization by Simulated Annealing. Science 13 May 1983: Vol. 220, Issue 4598, pp. 671-680

35. St. Hilaire, A. O.; and Carta, F. O., "Analysis of Unswept and Swept Wing Chordwise Pressure Data from an Oscillating NACA 0012 Airfoil Experiment," Vol. 1-Technical Report, NACA CR 3567, 1983.

36. St. Hilaire, A. O.; and Carta, F. O., "Analysis of Unswept and Swept Wing Chordwise Pressure Data from an Oscillating NACA 0012 Airfoil Experiment," Vol. 2-Data Report, NACA CR 165927, 1983.

37. Bousman, William G. “A Qualitative Examination of Dynamic Stall from Flight Test Data.” *Journal of the American Helicopter Society,* Volume 43, Number 4, 1 October 1998, pp. 279-295(17)

38. Yen, Jing G., Yuce, Mithat. “Correlation of Pitch-Link Loads in Deep Stall on Bearingless Rotors.” *Journal of the American Helicopter Society,* Volume 37, Number 4, 1 October 1992, pp. 4-15(12)

Appendix: Summary of the Unified model

This section will state the matrix form of the Unified model, and define each matrix and vector used. All of the equations necessary to implement the model in code are in this section, and the definitions here should look identical to Appendix A in [15], Appendix A in [14], and Appendix B of [27].

Generalized loads equation:

$$\frac{1}{2\pi\rho}\{L_n\} = -b^2[M]\left\{\ddot{h}_n + \dot{v}_n\right\} - bu_0[C]\left\{\dot{h}_n + v_n - \lambda_0\right\} - {u_0}^2[K]\{h_n\} \\ - b[G]\{\dot{u}_0 h_n - u_0 v_n + u_0\lambda_0\}$$

$-\square_0$ is the thin-airfoil theory lift.

$(\square_1 - \square_0\square)\square$ is the pitching moment about the quarter-chord.

D is the pressure drag (this does not include profile drag):

$$\frac{1}{2\pi\rho}D = -b\left\{\dot{h}_n + v_n - \lambda_0\right\}^T[S]\left\{\dot{h}_n + v_n - \lambda_0\right\} + b\left\{\ddot{h}_n + \dot{v}_n\right\}^T[G]\{h_n\} \\ - u_0\left\{\dot{h}_n + v_n - \lambda_0\right\}^T[K-H]\{h_n\} + \{\dot{u}_0 h_n - u_0 v_n + u_0\lambda_0\}^T[H]\{h_n\}$$

Γ is the total circulation from the linear theory, so it does not include $\Gamma_\square$, the circulation due to stall.

$$\frac{1}{2\pi}\Gamma = b\{1\}^T[C-G]\left\{\dot{h}_n + v_n - \lambda_1\right\} + u_0\{1\}^T[K]\{h_n\}$$

The “n” and “m” subscripts respectively refer to which inflow state and Glauert expansion state is being considered. There are a total of N inflow states and M Glauert states.

From the 2D Karunamoorthy inflow theory, this is the equation for the inflow states:

$$\{\dot{\lambda}\} = [A]^{-1}\left[\{c\}\left(\{e\}^T\{\dot{v}_n + \ddot{h}_n\} + \frac{u_0}{b}\{f\}^T\{\dot{h}_n\} + \frac{\dot{\Gamma}_0}{2b\pi}\right) - \frac{u_0}{b}\{\lambda\}\right]$$

All states except $\lambda_0$can be determined this way. To get λ_0:

$$\lambda_0 \approx \frac{1}{2}\sum_{n=1}^{N} b_n\,\lambda_n$$

where

$$b_n = (-1)^{n-1}\frac{(N+n-1)!}{(N-n-1)!}\frac{1}{(n!)^2}, \quad 1 < n < N-1$$

$$b_N = (-1)^{(N+1)}$$

Note that these two equations are misprinted in Ahaus [15].

Stall equation:

$$\frac{b^2}{U^2}\ddot{\Gamma}_n + \eta\frac{b}{U}\dot{\Gamma}_n + \omega^2\Gamma_n = -bU\omega^2\left[\Delta C_n + e\frac{b}{U}\frac{d\Delta C_n}{dt}\right]$$

Total lift:

$$\square = -\square_0 + \square\square_0\square_\square$$

Total drag:

$$Drag = D + \rho u_0\Gamma_d + (profile\ drag)$$

Total pitching moment about quarter-chord:

$$M = (L_1 - L_0 a)b + 2bu_0\Gamma_m$$

Stall parameter equations:

$$\omega = \omega_0 + \omega_2(\Delta C_L)^2$$

$$\eta = \eta_0 + \eta_2(\Delta C_L)^2$$

$$e = e_0 + e_2(\Delta C_L)^2$$

$$\{1\} = \{1 \;\; 0 \;\; 0 \;\; 0 \;\; \cdots\}^T$$

$\{b\} = \{b_1 \;\; b_2 \;\; b_3 \;\; \cdots \;\; b_N\}^T$ **from b_n above**

$$\{c\} = \{2 \;\; 1 \;\; \tfrac{2}{3} \;\; \tfrac{1}{2} \;\; \cdots \;\; \tfrac{2}{N}\}^T$$

$$\{d\} = \{\tfrac{1}{2} \;\; 0 \;\; 0 \;\; 0 \;\; \cdots\}^T$$

$$\{e\} = \{1 \;\; \tfrac{1}{2} \;\; 0 \;\; 0 \;\; \cdots\}^T$$

$$\{f\} = \{0 \;\; 1 \;\; 2 \;\; \cdots \;\; M\}^T$$

$$\{h_n\} = \{h_0 \;\; h_1 \;\; h_2 \;\; \cdots \;\; h_M\}^T$$

$$\{v_n\} = \{v_0 \;\; v_1 \;\; 0 \;\; 0 \;\; \cdots\}^T$$

$$\{\dot{v}_n + \ddot{h}_n\} = \left\{\dot{v}_0 + \ddot{h}_0 \;\; \dot{v}_1 + \ddot{h}_1 \;\; 0 \;\; 0 \;\; \cdots\right\}^T$$

$$\{\lambda_0\} = \{\lambda_0 \;\; 0 \;\; 0 \;\; 0 \;\; \cdots\}^T$$

$$\{\lambda_1\} = \{\lambda_0 \;\; \lambda_1 \;\; 0 \;\; 0 \;\; \cdots\}^T$$

$$[A] = [D + db^T + cd^T + \tfrac{1}{2}cb^T]$$

$$[T] = \begin{bmatrix} -ba & (b/\pi)[\sin\varphi_m - \varphi_m\cos\varphi_m] \\ b & (b/\pi)[\varphi_m - \sin\varphi_m\cos\varphi_m] \\ 0 & (b/\pi)\left[\frac{1}{n+1}\sin[(n+1)\varphi_m] + \frac{1}{n-1}\sin[(n-1)\varphi_m] - \frac{2}{n}\cos\varphi_m\sin(n\varphi_m)\right] \\ \vdots & \vdots \end{bmatrix}$$

$$[C] = \begin{bmatrix} f & 1 & 0 & 0 & 0 & \cdots \\ -\frac{1}{2} & 0 & \frac{1}{2} & 0 & 0 & \cdots \\ 0 & -\frac{1}{2} & 0 & \frac{1}{2} & 0 & \cdots \\ 0 & 0 & -\frac{1}{2} & 0 & \frac{1}{2} & \ddots \\ 0 & 0 & 0 & -\frac{1}{2} & 0 & \ddots \\ \vdots & \vdots & \vdots & \ddots & \ddots & \ddots \end{bmatrix} \quad [D] = \begin{bmatrix} 0 & -\frac{1}{2} & 0 & 0 & \cdots & 0 \\ \frac{1}{4} & 0 & -\frac{1}{4} & 0 & \cdots & 0 \\ 0 & \frac{1}{6} & 0 & -\frac{1}{6} & \ddots & 0 \\ 0 & 0 & \frac{1}{8} & \ddots & \ddots & 0 \\ \vdots & \vdots & \ddots & \ddots & 0 & \ddots \\ 0 & 0 & 0 & 0 & \frac{1}{2N} & 0 \end{bmatrix}$$

$$[G] = \begin{bmatrix} 0 & \frac{1}{2} & 0 & 0 & 0 & \cdots \\ 0 & 0 & \frac{1}{4} & 0 & 0 & \cdots \\ 0 & -\frac{1}{4} & 0 & \frac{1}{4} & 0 & \ddots \\ 0 & 0 & -\frac{1}{4} & 0 & \frac{1}{4} & \ddots \\ 0 & 0 & 0 & -\frac{1}{4} & 0 & \ddots \\ \vdots & \vdots & \vdots & \ddots & \ddots & \ddots \end{bmatrix} \quad [H] = \begin{bmatrix} 0 & 0 & 0 & 0 & 0 & \cdots \\ 0 & 1/2 & 0 & 0 & 0 & \cdots \\ 0 & 0 & 2/2 & 0 & 0 & \cdots \\ 0 & 0 & 0 & 3/2 & 0 & \cdots \\ 0 & 0 & 0 & 0 & 4/2 & \cdots \\ \vdots & \vdots & \vdots & \vdots & \vdots & \ddots \end{bmatrix}$$

$$[K] = \begin{bmatrix} 0 & f & 2 & 3f & 4 & \cdots \\ 0 & -\frac{1}{2} & 0 & 0 & 0 & \cdots \\ 0 & 0 & -\frac{2}{2} & 0 & 0 & \cdots \\ 0 & 0 & 0 & -\frac{3}{2} & 0 & \ddots \\ 0 & 0 & 0 & 0 & \ddots & \ddots \\ \vdots & \vdots & \vdots & \vdots & \ddots & -\frac{M}{2} \end{bmatrix} \quad [K'] = \begin{bmatrix} f & \frac{1}{2} & 0 & 0 & 0 & \cdots \\ -\frac{1}{2} & 0 & \frac{1}{4} & 0 & 0 & \cdots \\ 0 & -\frac{1}{4} & 0 & \frac{1}{4} & 0 & \cdots \\ 0 & 0 & -\frac{1}{4} & 0 & \frac{1}{4} & \ddots \\ 0 & 0 & 0 & -\frac{1}{4} & 0 & \ddots \\ \vdots & \vdots & \vdots & \ddots & \ddots & \ddots \end{bmatrix}$$

$$[M] = \begin{bmatrix} \frac{1}{2} & 0 & -\frac{1}{4} & 0 & 0 & \cdots \\ 0 & \frac{1}{16} & 0 & -\frac{1}{16} & 0 & \cdots \\ -\frac{1}{4} & 0 & \frac{1}{6} & 0 & \ddots & \ddots \\ 0 & -\frac{1}{16} & 0 & \ddots & 0 & \ddots \\ 0 & 0 & \ddots & 0 & \ddots & \ddots \\ \vdots & \vdots & \ddots & -\frac{1}{8M} & \ddots & \frac{M}{4(M^2-1)} \end{bmatrix} \quad [S] = \begin{bmatrix} f & 0 & 0 & 0 & 0 & \cdots \\ 0 & 0 & 0 & 0 & 0 & \cdots \\ 0 & 0 & 0 & 0 & 0 & \cdots \\ 0 & 0 & 0 & 0 & 0 & \cdots \\ 0 & 0 & 0 & 0 & 0 & \cdots \\ \vdots & \vdots & \vdots & \vdots & \vdots & \ddots \end{bmatrix}$$